OPEN ACCESS
IOP Publishing
Journal of Physics D: Applied Physics
J. Phys. D: Appl. Phys. **49** (2016) 363001 (45pp)
doi:10.1088/0022-3727/49/36/363001

Topical Review

Magnetism in curved geometries

Robert Streubel[1,2], Peter Fischer[2,3], Florian Kronast[4], Volodymyr P Kravchuk[5], Denis D Sheka[6], Yuri Gaididei[5], Oliver G Schmidt[1,7] and Denys Makarov[1,8]

[1] Institute for Integrative Nanosciences, IFW Dresden, 01069 Dresden, Germany
[2] Materials Sciences Division, Lawrence Berkeley National Laboratory, Berkeley CA 94720, USA
[3] Physics Department, UC Santa Cruz, Santa Cruz CA 95064, USA
[4] Helmholtz-Zentrum Berlin für Materialien und Energie GmbH, 12489 Berlin, Germany
[5] Bogolyubov Institute for Theoretical Physics of National Academy of Sciences of Ukraine, 03680 Kyiv, Ukraine
[6] Taras Shevchenko National University of Kyiv, 01601 Kyiv, Ukraine
[7] Material Systems for Nanoelectronics, Chemnitz University of Technology, 09107 Chemnitz, Germany
[8] Helmholtz-Zentrum Dresden-Rossendorf e.V., Institute of Ion Beam Physics and Materials Research, 01328 Dresden, Germany

E-mail: streubel@lbl.gov and d.makarov@hzdr.de

Received 31 March 2016, revised 20 June 2016
Accepted for publication 28 June 2016
Published 17 August 2016

Abstract

Extending planar two-dimensional structures into the three-dimensional space has become a general trend in multiple disciplines, including electronics, photonics, plasmonics and magnetics. This approach provides means to modify conventional or to launch novel functionalities by tailoring the geometry of an object, e.g. its local curvature. In a generic electronic system, curvature results in the appearance of scalar and vector geometric potentials inducing anisotropic and chiral effects. In the specific case of magnetism, even in the simplest case of a curved anisotropic Heisenberg magnet, the curvilinear geometry manifests two exchange-driven interactions, namely effective anisotropy and antisymmetric exchange, i.e. Dzyaloshinskii–Moriya-like interaction. As a consequence, a family of novel curvature-driven effects emerges, which includes magnetochiral effects and topologically induced magnetization patterning, resulting in theoretically predicted unlimited domain wall velocities, chirality symmetry breaking and Cherenkov-like effects for magnons. The broad range of altered physical properties makes these curved architectures appealing in view of fundamental research on e.g. skyrmionic systems, magnonic crystals or exotic spin configurations. In addition to these rich physics, the application potential of three-dimensionally shaped objects is currently being explored as magnetic field sensorics for magnetofluidic applications, spin-wave filters, advanced magneto-encephalography devices for diagnosis of epilepsy or for energy-efficient racetrack memory devices. These recent developments ranging from theoretical predictions over fabrication of three-dimensionally curved magnetic thin films, hollow cylinders or wires, to their characterization using integral means as well as the development of advanced tomography approaches are in the focus of this review.

Keywords: magnetic helix, magnetic shell, Dzyaloshinskii–Moriya interaction, curvilinear magnetism, shapeable magnetoelectronics, curved magnetic thin films, magnetic tubes

(Some figures may appear in colour only in the online journal)

1. Introduction

The interplay between geometry and topology is of fundamental importance throughout many disciplines. Examples include thin layers of superfluids [1] and superconductors [2, 3], nematic liquid crystal shells [4, 5], viral shells [6], cell membranes [7] and macromolecular structures [8]. Considerable effort has been devoted to understanding the role of the coupling between in-surface order and curvature of the underlying surface [9, 10]. Until recently, the impact of a curvature on electromagnetic properties of solids was mainly studied theoretically. The remarkable development in nanotechnology, e.g. preparation of high-quality extended thin films and nanowires as well as the potential to arbitrarily reshape those architectures after their fabrication, has enabled first experimental insights into the fundamental properties of three-dimensional (3D) shaped objects with photonic, plasmonic and magnetic properties.

This review focuses on the peculiarities emerging from geometrically curved magnetic objects, including two-dimensional (2D) bent wires [11–14], 3D helices [15–19], 3D curved shells, e.g. spherical [20–25] or tubular [26–28] and Möbius bands [29]. The objects are neither bulk systems nor nanoparticles, and are obtained by a conformal transformation of quasi-one-dimensional (1D) wires or extended thin films. We consider effects that are driven by the interplay between object geometry and topology of the magnetic sub-system.

Owing to intense theoretical and experimental efforts, the topic of magnetism in curved geometries has evolved in an independent research field of modern magnetism with many exciting theoretical predictions and strong application potential. The emergence of a curvature-induced anisotropy and an effective Dzyaloshinskii–Moriya interaction (DMI) are characteristic for bent and curved wires and surfaces [29–31], leading to curvature-driven magnetochiral effects [22, 26, 32–36] and topologically induced magnetization patterning [22, 29], including increased domain wall velocities in hollow tubes [37], chirality symmetry breaking [29, 34, 35] and Cherenkov-like effects for magnons [38]. In addition to these rich physics, the application potential of 3D-shaped objects is currently being explored as magnetic field sensorics for magnetofluidic applications [39, 40], spin-wave filters [41, 42], advanced magneto-encephalography devices for diagnosis of epilepsy at early stages [43–45] or for energy-efficient racetrack memory devices [37, 46].

The realization of those curved magnetic thin films requires advanced approaches for fabrication and characterization. There are numerous chemical and physical methods available to realize 3D magnetic objects of different sizes and geometries. Chemical approaches relying on electrochemical deposition in nanoporous templates combined with atomic layer deposition allow to produce magnetic rods [47–51], core-shell magnetic tubular heterostructures [52, 53] or even magnetic hollow tubes with diameters in the tens to hundreds of nanometer range [28, 54–56]. Due to their small dimensions, these objects possess rather simple axially symmetric domain patterns, such as longitudinal and azimuthal magnetization [28, 55]. Physical deposition provides high-quality layers with minimal surface roughness. Magnetic thin films and multilayers deposited onto curvature templates, e.g. cylinders [57], spheres [20, 21, 25, 58–60] or regular patterns of nanostructures of ripples, nanocones or nanodots prepared by low energy ion beam sputtering of semiconductor and oxide surfaces [61–64], resemble cap-like structures with well-determined structural and magnetic properties. Depending on the dimensions of the features in the template, e.g. diameter of spherical particles, curvature radii from 5 nm [65, 66] to some micrometers [60, 67, 68] are feasible to obtain.

Magnetic properties of those curved thin films are typically investigated employing magnetometry [28, 56, 69–71], magnetic force microscopy [20, 49, 58, 65, 72–75], scanning magnetoresistive microscope [23], transmission electron microscopy [76, 77], or soft x-ray imaging techniques including x-ray photoemission electron microscopy [52, 59, 74, 78, 79], transmission soft x-ray microscopy [23, 73, 79, 80] or x-ray holography [81].

Facilitating the glancing angle deposition (GLAD) approach [17, 82, 83], it is possible to realize magnetic helices [77, 84] as well as springs [85] with small dimensions down to 50 nm [86]. Combining physical deposition with strain engineering techniques [87–90] allows to realize wrinkled magnetic thin films [91–95] as well as rolled-up magnetic tubular architectures, such as Swiss rolls [40–42, 96, 97] and helices [15, 98, 99]. Typically, these objects possess diameters ranging from 1 μm [40, 42, 97, 100–102] up to 100 μm [39, 45]. These architectures possess complex domain patterns [96, 101, 103, 104], which determine their magnetoelectric responses [45, 101, 104].

In contrast to planar architectures or magnetic caps where each sample area can be observed using 'top-view' microscopy, 3D curved surfaces like helices, Möbius bands or Swiss rolls hide substantial parts of their structure. Structural and magnetic properties may only be revealed with tomographic imaging using the information drawn from precharacterization investigations as input. In this respect, integral measurements exploiting electric current flowing through the object (magnetoresistance) or stray fields of the structure (magnetometry) are well suited to determine characteristics of the entire sample, e.g. preferential magnetization orientation and switching fields. State-of-the-art magnetic tomographic imaging techniques, such as magnetic neutron tomography [105, 106], electron holography [76, 77, 107, 108] and vector

field electron tomography (VFET) [109, 110], rely on the detection of the phase shift originating from interaction with magnetic fields. While magnetic neutron tomography is applied to determine the spatial distribution of magnetic domain walls in macroscopic bulk materials, electron holography and VFET allow for reconstructing magnetization vector fields in nanoscopic samples with nanometer spatial resolution. On the other hand, utilizing x-ray magnetic circular dichroism (XMCD) [111–115] as element-specific contrast mechanism with full-field x-ray microscopies [116–118] provides nanometer spatial resolution to image the peculiarities of the magnetic domain patterns in 3D curved geometries extended over tens of micrometer. X-ray tomography is an established technique to reconstruct the 3D distributions of atomic densities in a vast of different 3D objects [105, 119–124]. Very recently, magnetic soft x-ray tomography (MXT) [96] offering the possibility to reconstruct magnetization spin textures in 3D-shaped mesoscopic objects has been reported.

The scope of this review is to present recent advances in the emergent topic of 3D curved magnetic thin films including both theoretical predictions and experimental studies. It is organized as follows: the second section provides the relevant theoretical background to assess curvature-driven effects. The generic theory is briefly discussed with more emphasis given to the specific shapes, e.g. hemispherical caps, tubes, or helices, which can be experimentally realized and investigated. Basics of x-ray microscopy extensively used to study 3D magnetic objects are briefly reviewed in section 3. Section 4 deals with the experimental realization of magnetic cap structures and their characterization. Experiments with tubular objects including rods, hollow tubes and rolled-up thin films are presented in section 5. Section 6 introduces an approach to fabricate and characterize magnetic micro- and nano-helices. Section 7 summarizes recent activities on the investigation of truly 3D magnetic textures using tomographic techniques. In this respect, magnetic neutron tomography, electron holography, vector field electron tomography and magnetic soft x-ray MXT will be addressed.

2. Theoretical background: curvature-induced effects in nanowires and nanoshells

The influence of a curvilinear geometry on transport and electromagnetic properties of matter is a hot topic in condensed matter and field theories. There has been long-standing discussions in quantum mechanics regarding the thin-layer quantization formalism of a particle constrained to a curved space [125–129]. The curvature of the system can induce an additional effective energy contribution, the so-called geometrical potential. The corresponding quantum mechanical approach was introduced by Jensen and Koppe [126] and generalized by da Costa [127] to study the tangential motion of a particle rigidly bound to a surface. The constraint of electron motion along the curve or surface results in transverse thin-wall quantization of the electronic states leading to specific quantum motion. The geometrical potential is determined by the local curvature of the system, which causes a vast of intriguing phenomena in charge and energy transport as well as in localization [129–143]. For instance, 1D wires possess, in addition to the geometrical potential induced by the wire curvature, a vector potential originating from the wire torsion [144–147] that manifests chiral effects.

The theoretical description of the evolution of the magnetization distribution in curved systems is based on the dynamics of the 3D vector order parameter, e.g. the magnetization unit vector in low-dimensional physical systems (quasi 2D nanoshell, quasi 1D nanowire). Studying curvature-induced effects on the evolution of vector fields has a long history [9, 10, 148, 149]. One of the well-known examples of nonlinear vector field models is the general Ginzburg–Landau vector model with the energy functional [150]:

$$E = \int \mathrm{d}\boldsymbol{x}\,[\boldsymbol{\nabla u} : \boldsymbol{\nabla u} + V(\boldsymbol{u})] \tag{1}$$

for the vector order parameter $\boldsymbol{u} = (u^1, u^2, \ldots, u^n)$ in the multidimensional real space $\boldsymbol{x} \in \mathbb{R}^d$. Here, $\boldsymbol{\nabla}$ is the nabla operator and V the geometrical potential. The colon operator denotes a scalar product in both real and order parameter spaces. If transformations of the order parameter and of the real space are independent of each other, the scalar product can be rewritten as: $\boldsymbol{\nabla u} : \boldsymbol{\nabla u} = G_{ij}\ \boldsymbol{\nabla} u^i\ \boldsymbol{\nabla} u^j$ with the metric tensor G_{ij} of the order parameter space. The behavior of vector fields $\boldsymbol{u}$ in a curved space [9, 10] becomes more sophisticated due to the intimate relation between the geometry of the substrate space ($\boldsymbol{x}$-variable) and of the field ($\boldsymbol{u}$-variable). In spite of numerous results on the behavior of a vector field in curved systems [9, 10, 148, 149], the problem is far from being solved. In the majority of studies, the 3D vector field was rigidly bound to the surface (shells) or to the curve (wires). In other words, the vector field was simplified to be *strictly tangential* to the curved substrate. In particular, the general expression for the surface energy of static tangential distribution of the director in a curvilinear shell of a liquid crystal was recently obtained [151–154] with possible applications using different geometries and orientation ordering [155–157]. Such strictly tangential field distributions were further used to study the role of curvature in the interaction between defects in 2D *XY*-like models to describe ultrathin layers of superfluids, superconductors, and liquid crystals confined to curved surfaces [158].

The phenomenological description of magnetization statics and dynamics in the continuum limit relies on the total energy of the magnet consisting of exchange, anisotropy, dipolar and Zeeman energy. To simplify the description, we focus on a ferromagnet with uniaxial anisotropy, i.e. an anisotropic Heisenberg model. In this case, the total energy functional reads:

$$E = \int \mathrm{d}\boldsymbol{x}\,[A\mathscr{E}_{\mathrm{ex}} + K(\boldsymbol{m}\cdot\boldsymbol{e}_{\mathrm{a}})^2]\,. \tag{2}$$

Here, the first term describes the isotropic exchange interaction

$$\mathscr{E}_{\mathrm{ex}} = (\boldsymbol{\nabla} m_x)^2 + (\boldsymbol{\nabla} m_y)^2 + (\boldsymbol{\nabla} m_z)^2, \tag{3}$$

with the exchange stiffness A. The second term in (2) is the anisotropy energy. The unit vector $\boldsymbol{e}_{\mathrm{A}}$ gives the direction of

the anisotropy axis; K is the anisotropy constant. We emphasize that $\boldsymbol{e}_{\mathrm{A}} = \boldsymbol{e}_{\mathrm{A}}(\boldsymbol{x})$ is a function of the spatial coordinates $\boldsymbol{x}$ in accordance to the geometry of a curvilinear sample. For example, $\boldsymbol{e}_{\mathrm{A}}$ pointing normal to a curvilinear shell and $K>0$ leads to an easy-surface anisotropy; $\boldsymbol{e}_{\mathrm{A}}$ being tangential to a curvilinear wire and $K<0$ manifests an easy-tangential anisotropy. The geometry-dependent direction of the local anisotropy requires the development of a fully curvilinear framework of the static and dynamic magnetization behavior.

The representation of the magnetic energy functional in an arbitrary curvilinear frame of reference is a challenge. A proper description of the curvilinear system has been given for specific geometries, such as cylinders [27, 159], tori [160, 161], cones [162, 163] and spheres [22]. Most theoretical studies are limited to the isotropic Heisenberg model with possible skyrmion-like solutions [159, 164–166]. For example, 2π-skyrmions can appear in an isotropic Heisenberg magnet due to the coupling between magnetic field and curvature of the surface [167]. In easy-surface Heisenberg magnets, the curvature of the underlying surface leads to the coupling between the localized out-of-surface component of magnetic vortex with its delocalized in-surface structure [22].

Very recently, a full 3D theory for thin magnetic shells and wires of arbitrary shape was put forth [30, 31]. This approach allows to derive the energy for arbitrary curves and surfaces, and arbitrary magnetization vector fields in the assumption that magnetostatic effects can be reduced to an effective anisotropy. In the curvilinear reference frame, the exchange energy (3) consists of three different contributions [31]:

$$\mathscr{E}_{\mathrm{ex}} = \mathscr{E}^{0}_{\mathrm{ex}} + \mathscr{E}_{\mathrm{A}} + \mathscr{E}_{\mathrm{D}}. \tag{4}$$

The first term describes the isotropic part of the exchange expression:

$$\mathscr{E}^{0}_{\mathrm{ex}} = \boldsymbol{\nabla} m_{\alpha} \cdot \boldsymbol{\nabla} m_{\alpha}. \tag{5}$$

Greek indices $\alpha, \beta, \gamma = 1, 2, 3$ numerate curvilinear components of vector fields and curvilinear coordinates and $\boldsymbol{\nabla}$ is the nabla operator in its curvilinear form [31]. The Einstein summation convention is used from here on.

In addition to this common exchange expression, curvature and torsion in magnetic shells [30] and wires [31] induce two effective magnetic interactions: (i) curvilinear geometry-induced effective anisotropy and (ii) curvilinear geometry-induced effective DMI.

2.1. Curvilinear geometry-induced effective anisotropy and shape-induced patterning

The effective anisotropy interaction stems from the curvilinear form of the exchange energy (4):

$$\mathscr{E}_{\mathrm{A}} = \mathscr{K}_{\alpha\beta} m_{\alpha} m_{\beta}. \tag{6}$$

For curved wires, the components $\mathscr{K}_{\alpha\beta}$ have a bilinear form with respect to curvature and torsion [31]; For shells, the components $\mathscr{K}_{\alpha\beta}$ have a bilinear form with respect to the components of the second fundamental form and spin connection of the surface [30]. In this respect, it is instructive to mention that the effective anisotropy emulates a scalar geometrical potential closely related to the potential which arises in the quantum mechanical problem of the particle rigidly bound to a surface [126–129].

An impressive manifestation of the geometry-induced anisotropy can be seen in the equilibrium magnetization configurations: the ground state essentially depends on the curvature preventing strictly tangential distributions even for strong easy-tangential anisotropy. For example, the ground state of a helix nanowire with strong anisotropy directed along the wire reveals a magnetization distribution that is tilted in the local rectifying surface. The tilt angle depends on the product of curvature and torsion [19, 168]. Analogously, the equilibrium magnetization distribution of a cone shell [30] is neither strictly tangential nor strictly normal to the cone surface. The angle between magnetization and easy (hard) anisotropy direction is proportional to the square of the local mean curvature [30].

Effects of the curvature-induced anisotropy are obvious in a tubular geometry. Systematic studies of magnetic nanotubes have proven an exchange energy of the form similar to (4) with an effective easy-axis anisotropy along the tube [27, 169–173]. The longitudinal anisotropy term $\mathscr{E}_{\mathrm{A}}$ gives rise to a gap formation in the dispersion relation of magnons in nanotubes [172]. Another striking consequence of the nontrivial geometry is *shape-induced patterning*. One of the simplest systems with such a phenomenon is a ring-shaped wire (circumference). This object is characterized by a finite constant curvature and zero torsion. The magnetization in rings with sufficiently large anisotropy forms a flux-closure vortex-like distribution [174, 175], and an onion distribution otherwise [31].

The interplay between curvilinear geometry and nontrivial topology of the magnetization structure in such systems can be crucial. For example, it is very well-known that the ground state of small flat magnets is spatially uniform (monodomain). In contrast, a quasiuniform magnetization distribution in small spherical shells is forbidden by the hairy-ball theorem [176]. Instead, two oppositely disposed vortices form as ground state (figure 1(a)) [22]. Another nontrivial topology is the Möbius ring that forces a discontinuity of any normal vector field due to its nonorientable surface. This discontinuity is the origin of the magnetization patterning in Möbius rings: topologically induced domain walls (figures 1(b) and (c)) [29, 177].

2.2. Curvilinear geometry-induced effective Dzyaloshinskii–Moriya interaction and chiral effects

The last term in the curvilinear exchange expression (4) is the curvature-induced effective Dzyaloshinskii–Moriya interaction:

$$\mathscr{E}_{\mathrm{D}} = \mathscr{D}_{\alpha\beta\gamma}(m_{\beta}\nabla_{\gamma} m_{\alpha} - m_{\alpha}\nabla_{\gamma} m_{\beta}), \tag{7}$$

where effective DMI constants $\mathscr{D}_{\alpha\beta\gamma}$ are antisymmetric with respect to α and β. Furthermore, they are linear in curvatures and torsion for curves, and linear in the components of the second fundamental form and spin connection for shells [31]. In some respect, this interaction resembles the vector geometrical potential generated by the torsion of the space curve.

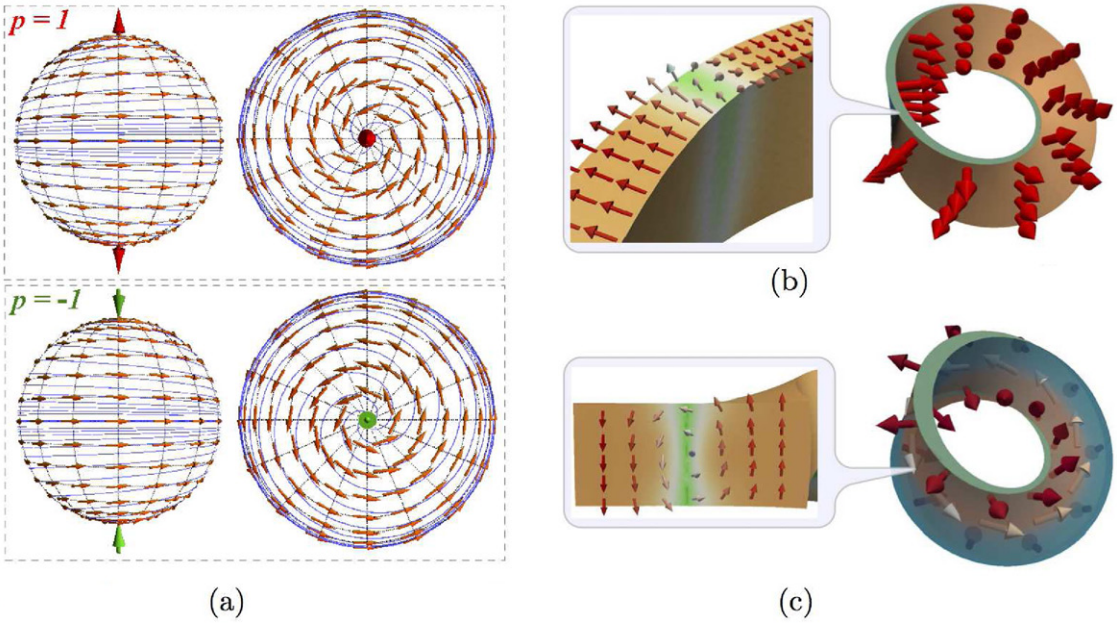

Figure 1. Shape-induced patterning: (a) Topologically induced double vortex ground state of soft magnetic spherical shell. Reprinted with permission from [22]. Copyright (2012) by the American Physical Society. (b), (c) Topologically induced domain walls appear as a ground state in magnetic Möbius ring with strong easy-normal anisotropy. Panels (b) and (c) are reprinted with permission from [29].

This problem was recently studied in the framework of a constrained quantum mechanics augmented with a spin-orbit coupling [144–147].

The curvature-induced effective Dzyaloshinskii–Moriya interaction is the source of a possible chiral symmetry breaking. As a rule chiral effects appear in systems with broken local inversion symmetry and are generally related to the geometrical Berry phase [178]. In magnetism, these phenomena are referred to as *magnetochiral effects* [26].

The simplest magnetic object with magnetochiral properties is a *magnetic vortex*, which forms as a ground state in soft-magnetic thin films with lateral dimensions of ≈ 1 μm due to the interplay between exchange and magnetostatic energy contributions. For circular shapes, the circulation of the in-plane magnetization tangential to the edge surface is divergence-free [179]. An out-of-plane magnetization exists only in a very small region around the center (vortex core) that has a lateral extension similar to the exchange length (typically 10 nm for soft-magnetic materials [180, 181]). The vortex state in planar systems is energetically degenerated with respect to the upward or downward magnetization of the vortex core (the vortex polarity $p = \pm 1$), and to the clockwise or counter-clockwise sense of magnetization rotation (vortex chirality/circulation). This degeneracy is lifted in curved systems and triggers new physical phenomena. Figure 2 depicts an example of spiral-like twisting of Landau domain patterns in Permalloy microsquares upon application of a perpendicular magnetic field. Micromagnetic simulations demonstrated the impact of a slight spherical curvature on the magnetic state arising from surface tensions in the underlying membrane [32]. A nucleation asymmetry between vortices with different core polarities was experimentally observed for square-shaped platelets [32, 182, 183]. In particular, different switching thresholds for vortex cores with opposite polarity were reported [182]. Sample roughness breaking the mirror symmetry at the local scale was given as an explanation for polarity and chirality symmetry breaking [183, 184].

Magnetic vortex distribution can form as a ground state in magnetic cap structures [59, 185]. In such a system, the interplay between magnetic vortex polarity, chirality, and the curvature of the underlying surface lifts the degeneracy of the switching efficiency of the vortex polarity with respect to the vortex chirality. In particular, a clockwise (CW) chirality requires smaller magnetic field pulses to switch the vortex polarity than a counter-clockwise (CCW) configuration (figure 3(a)) [36]. On the other hand, vortex states with opposite chirality reveal distinct switching fields (figure 3(b)) [186].

Let us now consider how the curvature effects the vortex state in a spherical magnetic shell. Unlike a planar disk where the magnetization follows concentric circles, the magnetization lines become spirals in spherical shells (figure 1(a)) [22]. Thus, the magnetization acquires an additional meridional component, which depends on the chirality, i.e. the product of the vortex circulation c and polarity p. For $c = +1$, the meridional component is oriented inwards ($p = -1$) and outwards ($p = +1$) at the poles. This effect originates from the curvature-induced DMI. The vortex core plays the role of a charge source for the vortex phase structure, which causes the polarity-circulation coupling, i.e. the coupling between the localized out-of-surface and the delocalized in-plane structures [22]. Note that the very same coupling effects the vortex-magnon interaction. It is well-known that in flat magnets the vortex core is a source of an effective magnetic field which leads to a splitting of different magnon modes [187–189]. This leaves the question: How magnon modes are affected by the curvature and the coupling between vortex polarity and circulation?

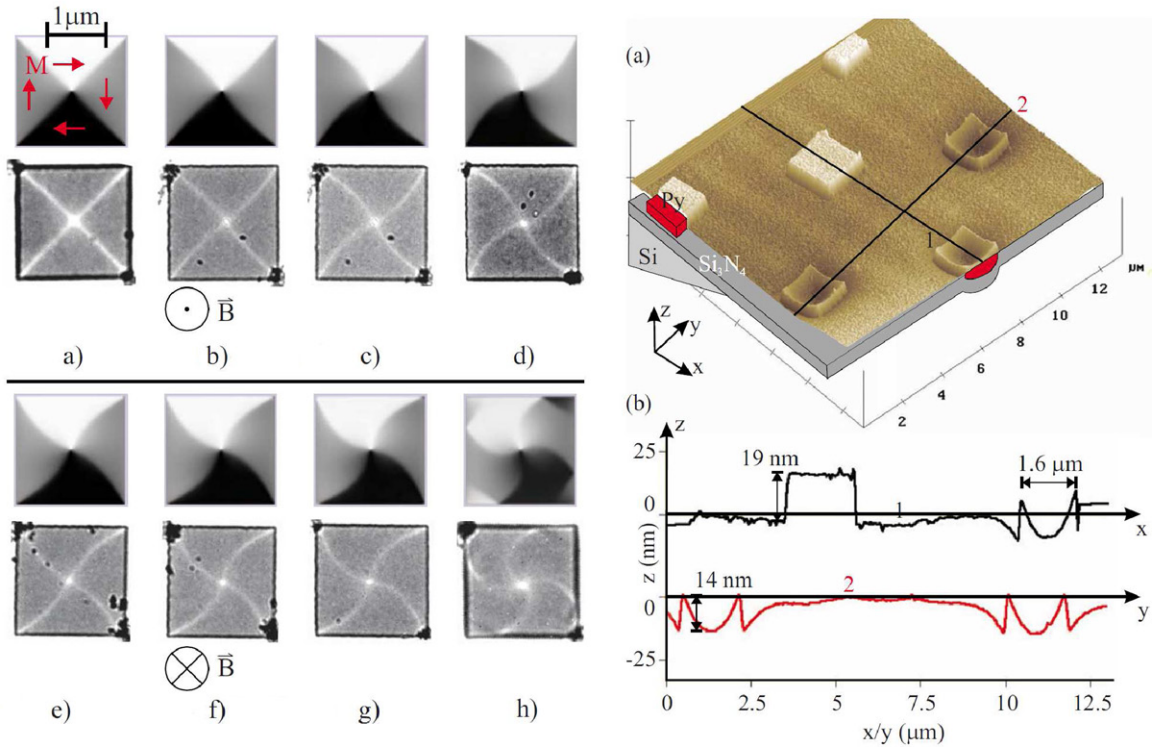

Figure 2. Left panel: Comparison of experiment (bottom rows) and simulation (top rows) for Permalloy squares with an edge length of 1.85 μm and a thickness of 19 nm. The images show the bending of the domain walls for different magnetic fields perpendicularly applied to the specimen. Right panel: (a) AFM image showing Permalloy squares on frame and Si_3N_4 membrane. (b) Line profiles of the AFM image: Microstructures on the frame are uniformly flat with a constant thickness of 19 nm; Squares on the membrane are significantly curved. Reprinted with permission from [32]. Copyright (2008) by the American Physical Society.

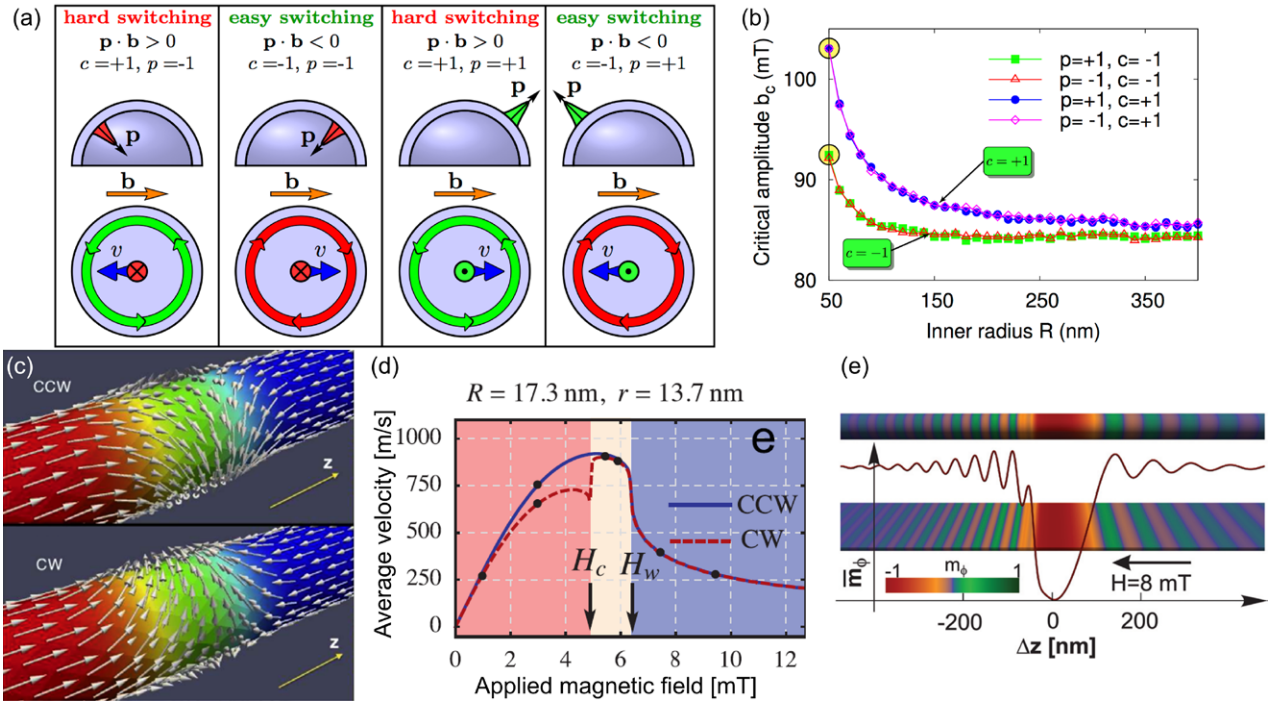

Figure 3. Magnetochiral effects in (a), (b) nanocaps and (c)–(e) nanotubes. (a) Chirality-dependent vortex core switching in magnetic cap structures: vortex core switching requires less excitation amplitude (b) for the vortex with negative chirality $c = -1$ when the projection of magnetic field $\boldsymbol{b}$ onto polarity p is also negative. Panels (a) and (b) are reprinted from [36] with the permission of AIP Publishing. (c) Chirality-dependent vortex domain wall propagation in a nanotube: two chiralities of head-to-head domain walls; (d) dynamical regimes upon field application. Panels (c) and (d) are reprinted from [190], with permission from Elsevier. (e) The domain wall with unfavorable chirality radiate spin waves while moving (from right to left) with different group velocity at front and back side (outer diameter: 60 nm; thickness: 10 nm). Panel (e) is reprinted from [33] with the permission of AIP Publishing.

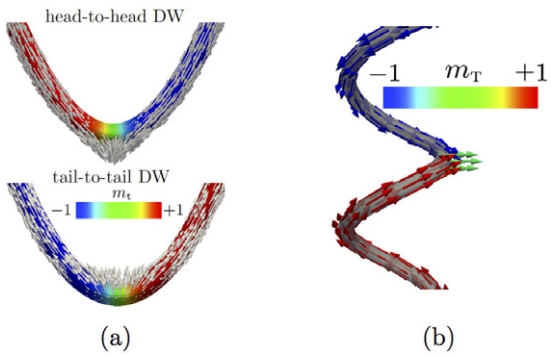

Figure 4. Symmetry breaking effects for domain walls in nanowires: (a) pinning of the domain wall in a flat wire bend, (b) structure of a head-to-head domain wall in a helix wire. Panel (a) is reprinted with permission from [216]. Copyright (2015) by the American Physical Society. Panel (b) is reprinted with permission from [220]. Copyright (2016) by the American Physical Society.

One can distinguish two typical situations where magnetochiral symmetry breaking occurs: (i) pattern-induced chirality breaking and (ii) geometry-induced chirality breaking.

2.2.1. Pattern-induced chirality breaking. The symmetry of the system is *per se* so high that magnetic states with the clockwise and counter-clockwise chiralities are degenerate. Such a situation takes place, for example, in straight cylindrical nanotubes that possess two energetically equivalent vortex domain walls with different chiralities (figure 3(c)). Using a 1D approximation, the problem of the domain wall dynamics can be reduced to a problem of a head-to-head (tail-to-tail) domain wall motion in a biaxial magnet. In this model the transversal anisotropy of easy-plane type is induced by magnetostatic surface charges while the longitudinal anisotropy of easy-axis type has two contributions: magnetostatic contribution and exchange contribution $\mathscr{E}_A \sim (\ell/R)^2$ with the characteristic magnetic length ℓ and the tube radius R.

One of the typical properties of a domain wall motion in biaxial magnet is the existence of a Walker breakdown [191]: the abrupt decrease of the domain wall velocity. This phenomenon was also found in tubular system (figure 3(d)), where the effective anisotropy rapidly decreases with increasing tube radius. Accordingly, the maximum average velocity is strongly dependent on radius [27] and domain wall chirality [27, 34, 35] (figure 3(d)). The dependence of the domain wall velocity on its chirality originates from magnetostatic volume charges [27, 34]. At a certain field value (velocity), the (slower) domain wall with the unfavorable chirality switches its chirality (figure 3(d); dashed line). This effect of chiral symmetry breaking for the vortex domain wall was studied analytically [35, 190] and by means of micromagnetic simulations [34, 35]. The switching is spatially uniform for small radii [27, 35] and essentially nonuniform via vortex-antivortex pair formation for large radii [34]. Further increase of the tube radius avoids the Walker threshold [37] leadig to Cherenkov radiation of magnons for fast domain walls (figure 3(e)) [33, 38].

It is well-known that the presence of Dzyaloshinskii–Moriya interaction [192, 193] breaks the degeneracy of spin waves and leads to an asymmetric spin-wave dispersion relation [194–196]. A similar effect of chiral symmetry breaking happens to spin waves propagating in azimuthally magnetized structures: the wave length of magnons at a given frequency is different for opposite propagation directions, which results in a splitting of the spin wave states with left- and right handed chiralities [26].

2.2.2. Geometry-induced chirality breaking. The simplest object to illustrate the interplay between geometrical and magnetic chiralities is a domain wall in curved wires. Novel concepts for magnetic logic [197–199] and storage [46, 200, 201] devices rely on domain wall motion inside curvilinear segments, e.g. a vertical configuration of the magnetic racetrack memory [46]. The pinning of magnetic domain walls in such wires due to local curvilinear defects is a well-known phenomenon [11, 12, 14]. Mechanisms of domain wall pinning have widely been studied: interaction with artificial notches [202–209], surface roughness [210–213] and inhomogeneities in the magnetocrystalline anisotropy distribution [213–215]. Recently, the role of the curvature in the domain wall pinning was elucidated [216]: a local bend of a nanowire becomes a source of pinning potential for a transversal domain wall [217–219]. The origin of the pinning potential is the curvature-induced DMI. As a result, the domain wall is pinned at the position of maximal curvature. When exposed to an external magnetic field, the wall oscillates in the pinning potential with a frequency determined by the product of wire curvature and its second derivative [216]. Moreover, a symmetry breaking occurs due to the curvature-induced DMI: the magnetization of a head-to-head (tail-to-tail) domain wall is directed outwards (inwards) (figure 4(a)). The latter effect was recently observed experimentally (figure 5) [209]. The symmetry breaking can be easily explained taking into account that DMI originates from exchange interaction: selecting the right domain wall direction defined by effective DMI makes the magnetization distribution more homogeneous and decreases the exchange energy. The energy gain caused by the effective DMI is proportional to the product of the domain wall charge and its chirality [216].

The presence of a torsion τ in e.g. helix wire breaks the geometrical chiral symmetry that is directly transferred to the magnetization distribution [19]. Simultaneously, curvature and torsion-induced DMI break the symmetry of spin waves inducing an effective magnetic field. The corresponding vector potential $\boldsymbol{A}$ is proportional to τ and constant for helices [19]. Hence, the effective magnetic flux density $\boldsymbol{B} = \nabla \times \boldsymbol{A}$ vanishes. Nevertheless, the presence of a magnetic field with the vector potential $\boldsymbol{A}$ breaks the mirror symmetry and lifts the degeneracy between magnetic excitations along different spatial directions known from planar systems. In this context, it is instructive to note the analogy between Dzyaloshinskii–Moriya interaction and Berry phase theory [221]. The geometrically induced DMI substantially changes the internal structure of the transverse domain wall [168]. In particular, the magnetization inside the domain wall rotates with a chirality opposite to that of the helix structure. The chiral symmetry breaking strongly impacts domain wall dynamics and provides means to move domain walls via different symmetry

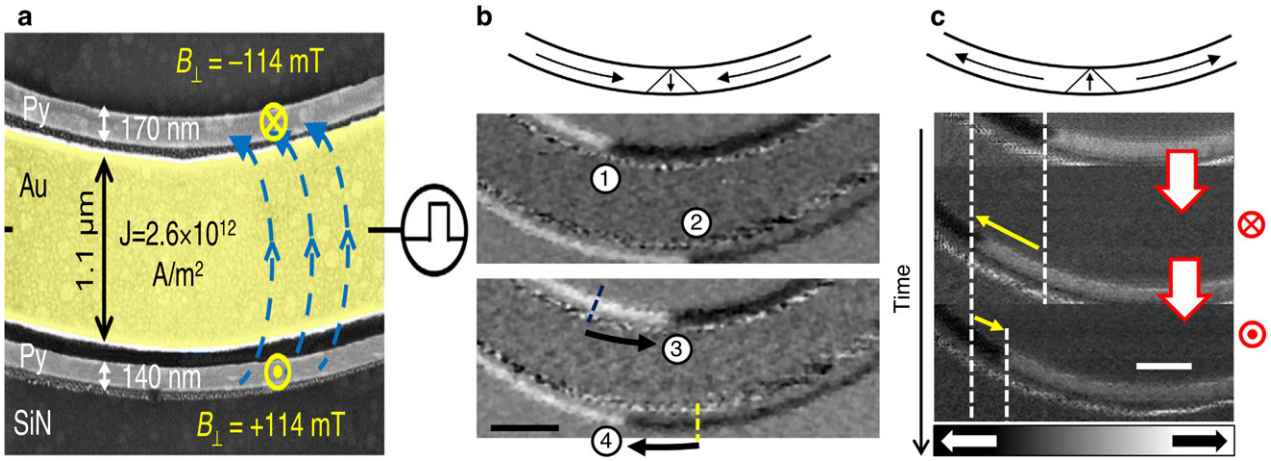

Figure 5. Lateral displacement of transverse walls (TW) triggered by out-of-plane (oop) magnetic field pulses. (a) Scanning electron microscopy (SEM) image of two curved planar nanowires embedding a strip line (yellow shaded), which generates out-of-plane magnetic fields with opposite direction at each nanowire. Panels (b) and (c) depict the scanning transmission x-ray microscopy (STXM) images visualizing magnetic domains and two (b) head-to-head ($p = 1$, $c = -1$) and (c) tail-to-tail ($p = -1$, $c = -1$) TWs. (b) Initial and final displacement of TWs after five subsequent field pulses as indicated in (a) revealing motion in opposite direction (840 ± 20) nm to the right and (-940 ± 20) nm to the left). Scale bar: 1 μm. (c) Same for upper nanowire and opposite current pulses. TW travels (680 ± 20) nm to the left and (340 ± 20) nm to the right, respectively. Scale bar: 500 nm. Reprinted with permission from [209]. Copyright (2014), Rights Managed by Nature Publishing Group.

spin currents, harnessing e.g. Rashba spin-orbit torque [168] and Zhang–Li torque [220].

A strong coupling between geometrical chirality and magnetochirality has been predicted for Möbius bands with topologically induced domain walls [29]. The energy gain associated with the effective DMI is proportional to the product of geometrical chirality of the Möbius band and domain wall magnetochirality [29].

3. Magnetic soft x-ray microscopy

Development and use of different magnetic imaging techniques are driven by the demand for measuring certain properties. In this respect, Kerr microscopy and scanning electron microscopy with polarization analyzer (SEMPA) [222–226] visualize magnetic surface domains at the micro- and nanoscale, respectively; Spin-polarized low-energy electron microscopy (SPLEEM) [227, 228] and spin-polarized scanning tunneling microscopy (SP-STM) [181, 229, 230] provide means to resolve inner structures of domain walls [231–233] and to study antiferromagnets [234, 235] and skyrmions [236–238] at an atomistic level, respectively. The enhanced spatial resolution of the latter two microscopies comes with the limitation to *in situ* characterization in ultra high vacuum and very clean (epitaxial) surfaces. Alternatively, recent advances in generating vortex electron beams with orbital angular momenta [239] pave the way towards magnetization-sensitive electron probes utilizing energy loss magnetic chiral dichroism (EMCD) [240] with electron holography (see section 7.3). These vortex beams are obtained as higher-order diffraction patterns after penetrating dislocation apertures [241], magnetic monopoles [242] or samples with magnetic fields aligned along the trajectory via the Aharonov-Bohm effect [243].

The analog of magnetooptical Kerr microscopy in the x-ray regime is magnetic x-ray microscopy that exploits the x-ray magnetic circular dichroism (XMCD) offering elemental and chemical state specificity at the nanoscale, variable probing depth and means to follow processes at the picosecond timescale. The magnetization in antiferromagnetic media can be further monitored utilizing x-ray magnetic linear dichroism (XMLD) [244]. The family of magnetic soft x-ray imaging consists of four techniques, i.e. scanning transmission x-ray microscopy (STXM) [245], full-field transmission x-ray microscopy (TXM) [111, 246–249], x-ray photoemission electron microscopy (XPEEM) [116, 250–252] and of lensless imaging with x-ray holography [253, 254]. The latter technique relies on coherent scattering of x-rays on domain walls and does not provide the elemental specificity known from XMCD-based approaches but offers the possibility to record ultrafast magnetization dynamics with a diffraction-limited spatial resolution ($\approx$1 nm). On the other hand, TXM and XPEEM combine advantages of utilizing XMCD and recording magnetization patterns at an instance. In fact, imaging field of views of about 20 μm with a spatial resolution of $\approx$20 nm as required for magnetic x-ray tomography (MXT) (see section 7.4) is accomplished within seconds, while taking two orders longer with STXM [255].

While high-order harmonic generation (HHG) [256, 257] of x-ray beams via femtosecond laser pulsing of ionized atoms is a rapidly evolving field with applications to magnetic systems [258, 259], commonly used synchrotron radiation sources [260] offer convenient access to brilliant and tunable x-ray radiation with adjustable polarization. Data discussed in this work is mainly collected at the Advanced Light Source (ALS), Lawrence Berkeley National Laboratory (LBNL) and at the Berliner Elektronenspeicherring-Gesellschaft für Synchrotronstrahlung (BESSY) II, Helmholtz-Zentrum Berlin (HZB). Existing beamlines allow for imaging remanent states

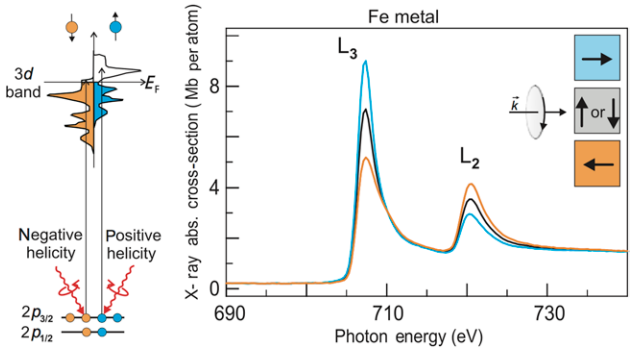

Figure 6. The number of free valence holes in the exchange-split 3*d* band determines the transition probability and thus white line intensity upon resonant x-ray absorption. Using circularly polarized light allows for selectively exciting electrons with minority or majority spins as reflected by the absorption spectra. Due to angular momentum transfer of the incidence photon to the excited electron, merely magnetization components along the x-ray propagation direction are distinguishable. The figure is reprinted from [244] with permission of Springer: Magnetism From Fundamentals to Nanoscale Dynamics, Interactions of polarized photons with matter, 2006, page 390, J. Stöhr and H. C. Siegmann, Figure 9.12. The experimental data on the right are from Chen *et al* [261] and have been corrected to correspond to 100% circular polarization.

and magnetization reversal processes as well as stroboscopic laser-, field- or current-driven magnetization dynamics at the sub-nanosecond timescale.

3.1. X-ray magnetic circular dichroism

Magnetic contrast in x-ray microscopies is provided by XMCD [111–115]. It describes the magnetization-dependent absorption of a circularly polarized x-ray beam penetrating a magnetic media [111–115]. When tuning the photon energy to a prominent resonance, such as the L_3 ($2p_{3/2} \rightarrow 3d$ electric transition) and L_2 ($2p_{1/2} \rightarrow 3d$ electric transition) edges in transition metals (Ni, Fe or Co), the x-ray absorption (electron excitation) strongly depends on the relative alignment of magnetization and x-ray propagation direction (photon angular momentum/ helicity) with a maximum for collinearity (figure 6) due to Stoner split valence bands; magnetization components perpendicular to the x-ray propagation direction are not distinguishable. It is common use to eliminate non-magnetic contributions by calculating the difference in the x-ray absorption for left- and right-circularly polarized light. Normalized by the sum of both absorptions, the XMCD signal becomes:

$$I_{\mathrm{XMCD}} = \frac{I_{\uparrow\downarrow} - I_{\uparrow\uparrow}}{I_{\uparrow\downarrow} + I_{\uparrow\uparrow}} = \frac{I_- - I_+}{I_- + I_+}. \qquad (8)$$

Here, $I_{\uparrow\uparrow}(I_+)$ and $I_{\uparrow\downarrow}(I_-)$ refer to absorption intensities with parallel and antiparallel alignment of magnetization and photon helicity, respectively. It is odd in magnetization and photon helicity, and reverses its sign upon switching either of them. The corresponding magnitude may reach 20% at the $L_{2,3}$ edges for transition metals due to large spin-orbit coupling [244].

The large XMCD effect at the $L_{2,3}$ edges originates from two fundamental properties [113, 114], namely conservation of angular momentum during photoelectron excitation and conservation of spin momentum during interband transition. In particular, the angular momentum of the photon is transferred to the excited photoelectron that is spin-polarized due to spin-orbit coupling. The opposite coupling for $2p_{3/2}$ $(l + s)$ and $2p_{1/2}$ $(l - s)$ causes an opposite spin polarization. The transition probability and thus the white line intensity is determined by the number of valence holes in the exchange-split 3*d* band. Consequently, the electron excitation with a minority spin is pronounced due to spin momentum conservation leading to an XMCD signal with opposite sign at the L_3 and L_2 edges (figure 6). Remarkably, the difference in absorption for left- and right-circularly polarized light (or opposite magnetization directions) at the L_3 and the L_2 edge provides further means to quantify element specifically spin and orbital momenta at a local scale [113, 114] as experimentally confirmed in the pioneering work by Chen *et al* [261].

3.2. Full-field soft x-ray microscopy

The brief description of full-field transmission soft x-ray microscopy (TXM) will be given on the example of the x-ray microscope XM-1 at beamline 6.1.2 (ALS) [249] which is used to visualize magnetic domain patterns in transparent magnetic nanomembranes. For this sake, the x-ray beam is diffracted while passing through a Fresnel condenser zone plate (CZP) and collimated after interacting with the transparent sample by an image-forming Fresnel micro zone plate (MZP) (figure 7(a)), usually consisting of circular patterns with radially alternating refraction indices and decreasing separation towards the edge [262–264]. Width of the outermost zone of the CZP, size and position of the pinhole define the energy resolution ($\lesssim$0.5 eV), while the lateral spatial resolution ($\lesssim$20 nm) is determined by the outermost zone width of the MZP [244, 245]. The field of view is fixed to 8 μm. The photon energy is tuned to a prominent resonance by varying the distance between CZP/ MZP and sample due to a wavelength-dependent diffraction angle/ focal length. Thus, ordinary bending magnets with high photon yield but broad energy spectra (with respect to undulators) can be used when inserting a slit before the CZP to select the photon helicity (circular polarization) [249]. The depth of focus is about 1 μm. Hence, magnetic domains distributed $\lesssim$1 μm along the x-ray beam propagation direction are in focus; Their contributions cannot be disentangled. Contributions originating from areas separated by more than 1 μm while one region is in focus can be discriminated due to varying sharpness of domain walls and overall XMCD signal. However, this implies knowledge about the magnetic properties of the local magnetization.

The sample is mounted onto a holder at ambient conditions. Out-of-plane and in-plane magnetization sensitivity is provided using sample holders with a surface normal tilted by 0° and 30° with respect to the x-ray beam propagation direction, respectively. External magnetic fields up to $H = \pm 200$ kA m^{-1} may be applied in-plane or at 60° to the sample surface allowing for in-field measurements. Pulse and frequency generators connected via SMA to strip lines/ coplanar wave guides can be facilitated to perform current- and field-driven excitation studies. Films are prepared on 2.5 mm × 2.5 mm Si_3N_4

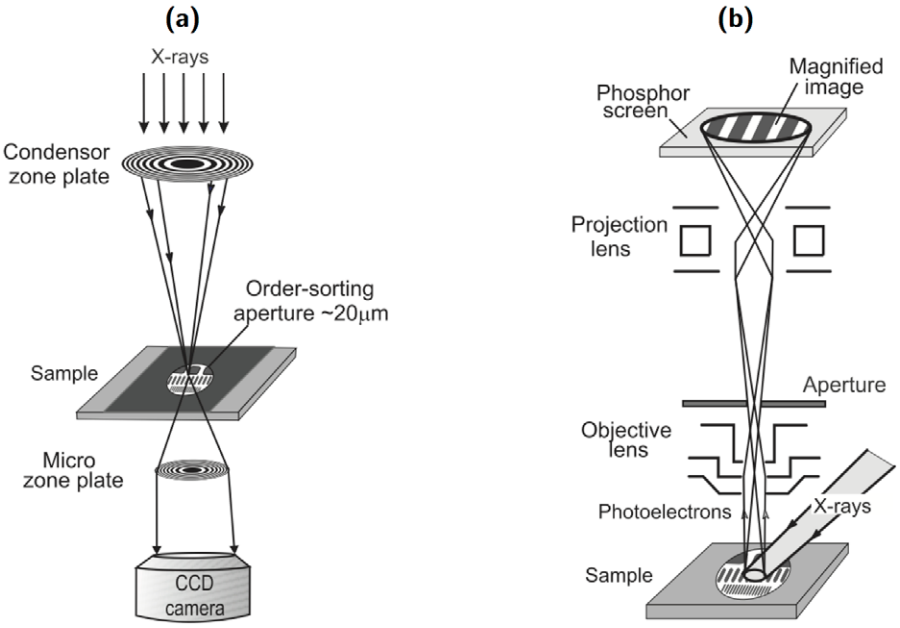

Figure 7. Schematics of (a) transmission x-ray microscopy (TXM) and (b) x-ray photoemission electron microscopy (XPEEM). (a) The incidence x-ray beam is deflected at a condenser zone plate (CZP), consisting of circular patterns with radially alternating diffraction indices and decreasing separation towards the edge. The x-ray energy is selected by adjusting the separation between CZP and sample according to the energy-dependent diffraction angle. After penetrating the transparent sample, the beam is collimated by the micro zone plate (MZP) that projects the sample onto the CCD camera. Spatial and energy resolution are determined by CZP and MZP. (b) A monochromatic x-ray beam excites secondary photoelectrons at a shallow incidence angle that are focused and collected by a PEEM. While the energy resolution is determined by the undulator, the spatial resolution is limited by the electron optics of the PEEM, size of the aperture and operation voltage. The figure is reprinted from [244] with permission of Springer: Magnetism From Fundamentals to Nanoscale Dynamics, X-rays and Magnetism: Spectroscopy and Microscopy, 2006, page 460, J Stöhr and H C Siegmann, Figure 10.17.

nanomembranes with a thickness $d \approx 200$ nm and a transmission $\approx$70% for x-ray energies in the range $(700 \sim 900)$ eV.

3.3. X-ray photoemission electron microscopy

Magnetization textures in very thin films ($d \approx 2$ nm) are preferentially visualized by surface sensitive XPEEM. The setup at BESSY II (UE49-PGM [116]) consists of a commercial spin-polarized PEEM (PEEM III with analyzer, Elmitec) with a spatial resolution of $\approx$30 nm and a variable field of view in the range $(3 \sim 50)$ μm. As the incidence angle of the x-rays is fixed to 74° with respect to surface normal, only one magnetization component can be accessed. Photoelectrons are resonantly excited while exposing the sample to a linearly or circularly polarized x-ray beam generated by an undulator with an energy resolution $\lesssim$0.2 eV (figure 7(b)). The number of emanating photoelectrons, i.e. secondary electrons, is directly proportional to the x-ray absorption at the L_3 or L_2 edge [265] and may analogously serve to visualize the magnetization based on XMCD. The normalization to the intensity of absorbed x-rays is particularly attractive for very thin films as much larger signal-to-noise ratios compared to MTXM can be obtained. The penetration/ information depth is determined by screening effects due to Auger electrons created after core excitation (secondary electron emanation) and is limited to $(5 \sim 10)$ nm at resonance in transition metals [115]. Small variations in the secondary electron momentum normal to the surface, originating from local modifications of the work function, electrostatic charging or topography, are accessible by tuning the start voltage. This means that contributions from regions with different surface normal as occurring on curved surfaces can be pronounced or compensated by adjusting the start voltage.

The sample, floating at $(5 \sim 20)$ kV to accelerate the photoelectrons, is mounted onto a rotation stage that is in contact with a thermal bath of variable temperature $T = (50 \sim 400)$ K. External magnetic fields up to $H = \pm 40$ kA m^{-1} may be applied parallel or normal to the sample surface allowing for in-field measurements. Recording images while applying a magnetic field requires to readjust alignments at each measurement point, since the photoelectrons are deflected due to the Lorentz force. Studies of global and local ground states by thermal demagnetization [266], coupling between plasmons and magnetization [267, 268] as well as all-optical switching processes in transition metal-rare earth compounds [269, 270] can be carried out by applying femtosecond laser pulses with variable polarization.

4. Magnetic cap structures

4.1. Hemispherical caps

The self-assembly of nonmagnetic spherical nanoparticles capped with a magnetic film resembles an elegant way to create curved magnetic nanostructure arrays (cap arrays) [20]. In these systems, the fundamental magnetic interactions

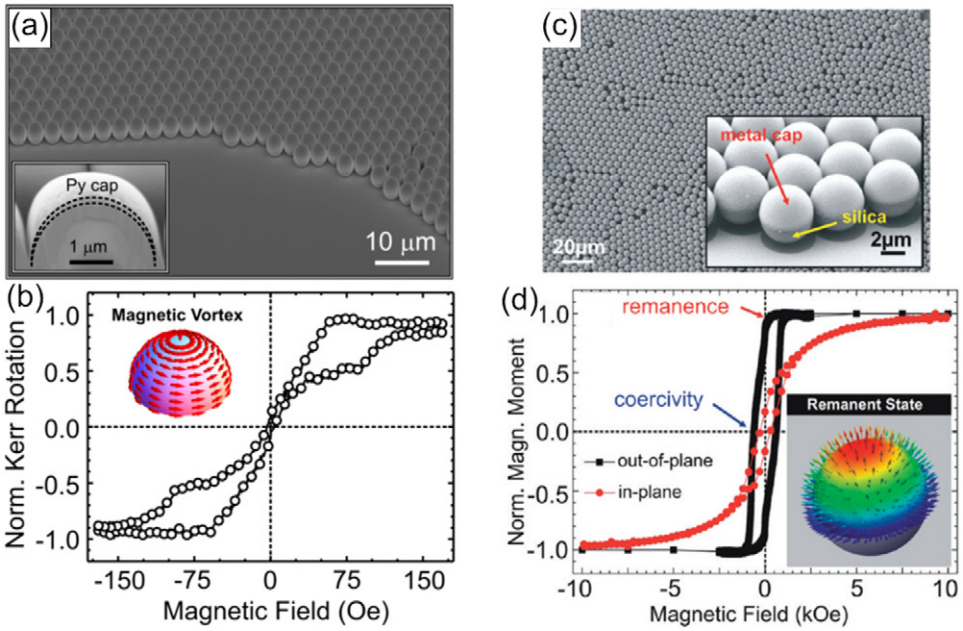

Figure 8. (a) Scanning electron microscopy (SEM) image of SiO_2 spheres monolayer capped with Pt(2 nm)/Py(100 nm)/Pt(2 nm) (diameter: 3 μm). Inset shows cross-section through a capped sphere cut by focused ion beam etching (FIB) (cap indicated by dashed lines). (b) Magnetic hysteresis loop measured with longitudinal Kerr magnetometry and magnetic field applied parallel to the substrate. Hysteresis loop suggests the formation of a magnetic vortex state (illustrated as inset). Panels (a) and (b) are reprinted with permission from [68]. Copyright (2013) American Chemical Society. (c) SEM image of an array of self-assembled spherical particles (diameter: 5 μm). Inset shows coating of the Janus particles with metal film assuring their catalytic (topmost Pt layer) and magnetic properties ($[Co/Pt]_5$ multilayer stack). (d) Magnetic hysteresis loop recorded with SQUID magnetometry. Inset illustrates distribution of the magnetic moments at remanence. Panels (c) and (d) are reprinted with permission from [69]. Copyright (2012) American Chemical Society.

(exchange and magnetostatic) can be easily tuned by varying the particle diameter as well as the material properties of the deposited magnetic films, e.g. possessing in-plane (figures 8(a) and (b)) or out-of-plane (figures 8(c) and (d)) easy axis of magnetization.

4.1.1. Fabrication of self-assembled arrays of nonmagnetic spherical particles. Using monolayers of self-assembled closely packed spherical particles [271–273] as curvature template offers both high symmetry of the resulting cap structure and the possibility to prepare highly ordered cap arrays. Depending on the purpose, either silica or polystyrene spheres with a diameter ∅ in the range from 50 nm to 5 μm are used. Metal deposition onto the curvature template results in a curvature-driven thickness gradient with a nominal thickness at the very center of the cap and a persistently decreasing thickness towards the equator (inset of figure 8(a)).

The propagation vector distribution within the sputter plasma assures deposition both through the interstitials of mono-, bi- and trilayers and under the particles [274, 275]. Upon removal of the particle monolayers using ultrasonication, a non-planar honeycomb lattice with periodically alternating thickness is obtained [274]. Lattice periodicity, thickness and width of the interconnects can be adjusted by changing particle size, thickness of deposited materials and plasma etching of polystyrene particles before metal deposition, respectively [266, 274, 275]. Engineering a height asymmetry into the honeycomb lattice is achieved by positioning the sample under the aperture with a radial offset. To increase the degree of order in the self-assembly process, template-directed self-assembly can be employed to arrange spherical particles into a polymer resist template with regular hole arrays, produced by extreme ultraviolet interference lithography (EUV-IL) [276].

4.1.2. Out-of-plane magnetized caps. Multilayers of $[Co/Pt]_N$ and $[Co/Pd]_N$ are common prototypical systems to investigate structural and magnetic properties of magnetic thin films with out-of-plane easy axis of magnetization grown on nanoparticle arrays. The magnetic anisotropy can be tuned adjusting the thickness of individual Co layers to tailor interface and shape anisotropy [277]. With increasing Co layer thickness, a so-called thickness-driven spin reorientation transition (SRT) occurs, which refers to the transformation from an easy-axis to easy-plane orientation [278, 279]. The crossover Co layer thickness is about $(0.3 \sim 1.7)$ nm [280–283], depending on substrate [281], Pt/Pd layer thickness, and the interfacial properties [282].

The deposition of metal films on a curved substrate leads to the formation of grains with tilted growth direction and lateral grain sizes, which become smaller with increasing tilt angle. The presence of the tilt in the growth direction has important consequences on the magnetic properties of the multilayer. The preferential orientation of the magnetization in $[Co/Pd]_5$ multilayers governed by the interface anisotropy [284, 285], follows the curvature of the particle's surface deviating from a simple easy-axis direction (figures 9(a) and (b)). Large deviations between deposition direction and particle surface normal as occurring near the equator result in a mixture of Co and Pd atoms instead of heterostructuring (figure 9(c)). For instance,

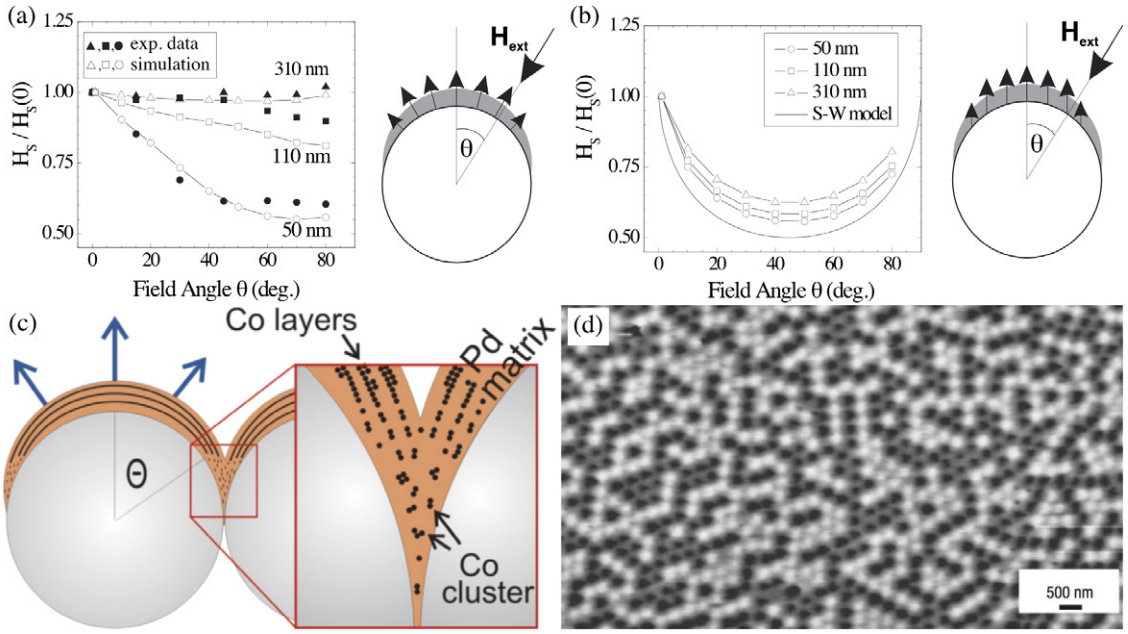

Figure 9. Magnetic cap structures with PMA. (a) Switching field of radially magnetized caps as a function of field direction (illustrated by schematics). (b) Simulations for caps assuming uniaxial anisotropy, including a representation of the Stoner-Wohlfarth model. The switching field Hs is normalized to its value at $\theta = 0$. Panels (a) and (b) are reprinted with permission from [24]. Copyright (2006) by the American Physical Society. (c) Schematics illustrating the transition from well-defined [Co/Pd]N multilayers to a Pd-rich Co-Pd alloy resulting in strong exchange decoupling of the neighboring cap structures in the array. Panel (c) is reprinted from [288] with the permission of AIP Publishing. (d) MFM image depicting exchange decoupled out-of-plane magnetized caps with diameters of 310 nm. Panel (d) is reprinted by permission from Macmillan Publishers Ltd: Nature Materials [20], copyright (2005).

$[Co(0.27\,nm)/Pd(0.8\,nm)]_N$ multilayers with thin Co layers are expected to form a Pd-rich Co-Pd alloy with a Curie temperature below 300 K [286, 287]. Consequently, the neighboring nanocaps structurally interconnected are exchange decoupled at room temperature due to the emergence of a paramagnetic intersection region (figure 9(d)) [20, 288].

4.1.3. Soft magnetic caps. For soft-magnetic films, such as $Ni_{80}Fe_{20}$ (Permalloy), the major role of the curvature is to alter the film thickness/ shape. Depending on sphere diameter and film thickness, magnetic layers in closely packed cap arrays are either modulated in thickness or structurally separated, which in turn provides means to tailor magnetic exchange and magnetostatic interactions.

In order to resolve the in-plane magnetization components of soft-magnetic nanostructures, x-ray spectromicroscopy techniques, such as X-PEEM or TXM (see section 3), that use XMCD as magnetic contrast mechanism have been applied. The in-plane sensitivity is provided by resonantly illuminating the sample with circularly polarized x-rays at a shallow incidence angle. As a reference, the dipolar XMCD contrast of a planar nanodisk (indicated by dashed circle) is shown in figure 10(a), referring to a magnetic vortex state [289]. The nanopattern was prepared by reactive ion etching (RIE) and is significantly underetched. Shallow incidence angle and partial transmission of the x-ray beam combined with XMCD and substantial vertical offset of the disk with respect to the planar substrate cause a magnetic contrast at the back side of the disk (lower part of figure 10(a)) that is referred to as XMCD shadow contrast (see also section 5.1.1) [59]. The contrast inversion in the shadow region originates from the attenuation of the x-ray beams while penetrating the disk according to the XMCD effect and different photoelectron excitation intensities on the substrate. In this sense, the substrate acts as a 2D sensor similar to the CCD screen in TXM. The lateral dimensions of direct and XMCD shadow contrast are similar as the disk is parallel to the substrate.

Single cap. The XMCD contrast of 3D magnetic objects is more complex than that of planar architectures due to multiple interactions with various magnetization orientations. In other words, the detected XMCD signal represents a net value with an enhanced, reduced, compensated or even inverted contrast. For instance, the XMCD signal of magnetic caps with a film thickness $d = 20\,nm$ and a diameter down to 100 nm (indicated by dashed circles) exhibits a quadrupole-like pattern accompanied by an inverted shadow contrast (figure 10(b)) [59]. The origin of the quadrupole XMCD contrast is of the same nature as the shadow contrast, namely a photoelectron excitation with circularly polarized light with distinct intensities. The XMCD contrast at the back side of the cap is weaker than that of the front side due to competing contributions. It is not compensated because of a significantly larger x-ray absorption during the first penetration due to thickness gradient and incidence angle. A non-zero background contrast is apparent as the surrounding planar substrate is also covered with the magnetic film. The peculiar fingerprint of magnetic vortices in cap structures is proven by applying an external magnetic field parallel to the x-ray propagation direction and recording the displacement of the vortex core perpendicular to the field direction

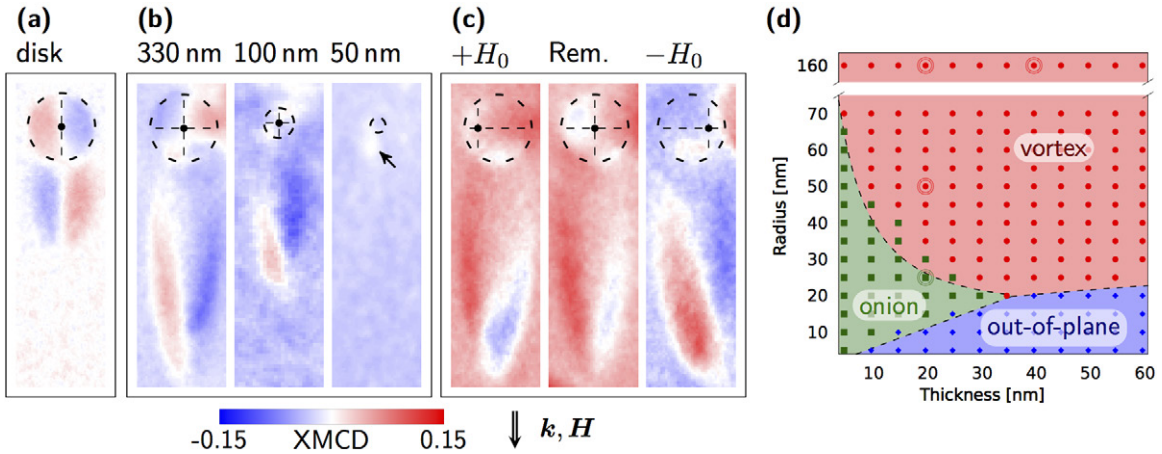

Figure 10. Magnetic domain patterns in individual hemispherical Py caps visualized by T-XPEEM. (a) Magnetic vortex in a planar disk with significant vertical offset from the substrate causes a dipolar XMCD contrast in the disk and an inverted shadow contrast at the back side. (b) The curvature of the cap leads to a quadrupole-like contrast due to interactions with front and back side and an extended shadow contrast. The shadow contrast can be used (b) to identify magnetic states below the spatial resolution limit or (c) to observe core displacements ($H_0 = 12$ kA m^{-1}) and even dynamics. (d) Numerically determined phase diagram of magnetic equilibrium states in caps (symbols) and disks (shaded areas) with inserted experimental data (double circle). Reprinted from [59] with the permission of AIP Publishing.

(figure 10(c)). The shallow angle illumination in transmission x-ray photoemission electron microscope (T-XPEEM) enlarges the XMCD signal of the cap structures along the x-ray propagation direction by a factor of ≈3.5 (=tan 16°). Additionally, the shadow contrast suffers less from local field distortions caused by the cap itself and can be used to determine the vortex core location during magnetization reversal and magnetization dynamics, or to identify magnetic states below the resolution limit (figure 10(b)) and to assemble a phase diagram for a single magnetic cap (figure 10(d)).

Cap array. Figures 11(a) and (b) depict the remanent states of closely packed cap arrays initially saturated by an in-plane magnetic field oriented 4° and −20° with respect to the lattice orientation, respectively. Each cap exhibiting a quadrupolar XMCD contrast is indicated by red and green circles referring to clockwise and counterclockwise circulation, respectively. The vortex circulation assemble to characteristic patterns, such as straights and steps, depending only on the lattice orientation as the magnetic properties of individual caps are isotropic. Analyzing its distribution for the two given lattice orientations, reveals a majority of straights and steps for alignments close to 0° and 30°, respectively, extended over several caps (figures 11(a) and (b)). The experimental observation of those ground states implies some kind of collective transition, since the system is not frustrated at remanence due to vanishing magnetostatic interaction between adjacent vortices. The term 'collective' refers to the fact that the circulation of each vortex is predetermined by the magnetostatic nearest neighbor interaction in the array during the vortex nucleation process. In particular, the local magnetization during the magnetization reversal process is affected by the lattice orientation of the closely packed cap array and forms meander-like flux-closure domains with nodes located at the intersect of adjacent caps [74]. These modulations eventually lead to the circulation patterns observed experimentally.

The virgin curve extracted from the front side of the cap undergoing a vortex nucleation is shown in figure 12(a) as

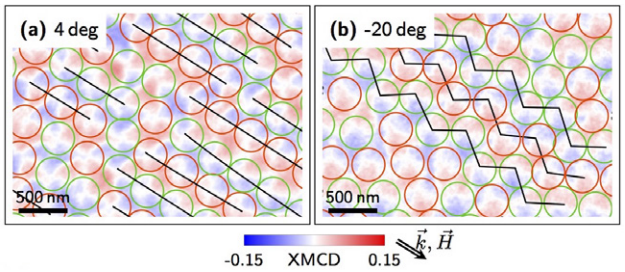

Figure 11. Vortex circulation patterns in closely packed Py(40/330) cap arrays. Remanent states after initially saturating with an in-plane magnetic field along (a) 4° and (b) −20° with respect to the lattice orientation. The vortex circulation is indicated by red and green circles. Analyzing the occurrence of straights and steps reveals an angle dependence and a non-vanishing vortex circulation coupling. Reprinted from [74] with the permission of AIP Publishing.).

blue symbols and reveals a transition at $H_{an} = (11.5 \pm 1.5)$ kA m^{-1}. This value matches very well the vortex annihilation field $H_{an} = (12.0 \pm 0.8)$ kA m^{-1} that were obtained by SQUID measurements. The agreement between local spatially resolved XMCD and integral SQUID measurements could be exploited to assemble magnetic phase diagrams of closely packed caps at $T = 300$ K and $T = 3$ K (figures 12(c) and (d)). The solid lines separating the two phases, vortex and onion state (figure 12(b)), are given as a guide-to-the-eye. Comparing the phase diagram for closely packed cap arrays (figure 12) with that of single caps (figure 10(d)) reveals an expanded onion phase due to magnetostatic intercap interaction during the vortex nucleation process. The third phase with out-of-plane magnetization for large aspect ratios is absent in closely packed cap arrays due to the formation of a thickness modulated extended film instead of individual caps favoring the onion state.

4.1.4. Imprinted non-collinear spin textures in hemispherical caps. Vertically stacking two well-studied systems,

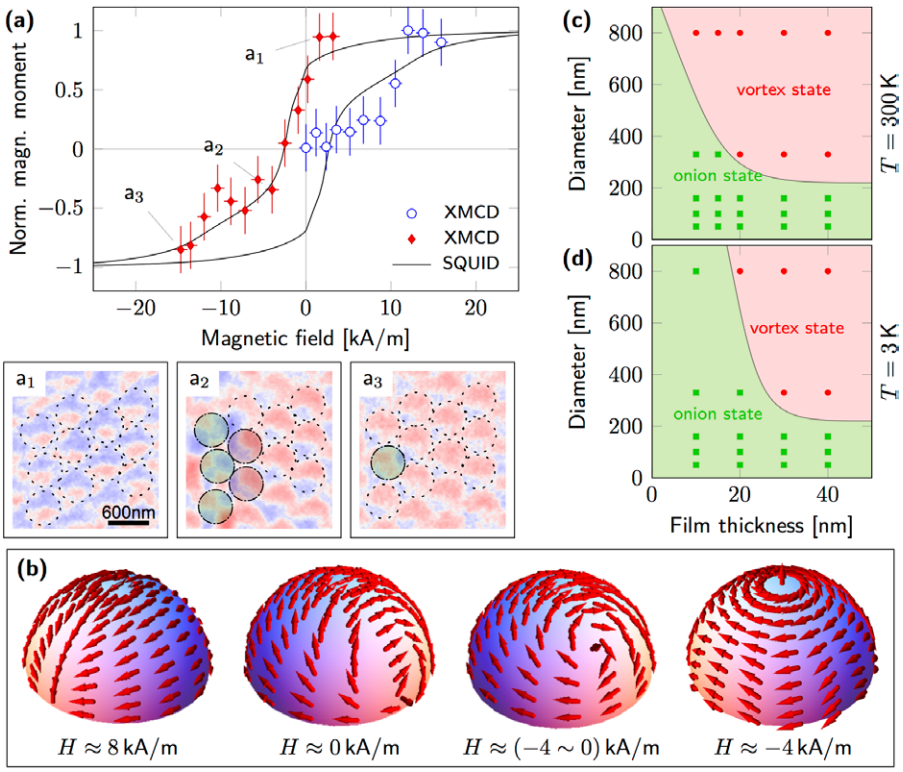

Figure 12. (a) Magnetization reversal of closely packed Py(20/330) caps (indicated by dashed circles) visualized by XPEEM. The images a_1, a_2 and a_3 illustrate remanent, transition and saturation state, respectively. Caps that exhibit vortex states are indicated by · –. The XMCD hysteresis curves are averaged over the front side of these vortices. The SQUID hysteresis loop is plotted as reference (solid). (b) Schematics of onion ($H \approx 8$ kA m^{-1}) and vortex ($H \approx -4$ kA m^{-1}) states exposed to in-plane magnetic fields. Panels (a) and (b) are reprinted with permission from [78]. Copyright (2012) by the American Physical Society. Panels (c) and (d) show the phase diagrams derived form the SQUID hysteresis loops at $T = 300$ K and $T = 3$ K, respectively. Boundary lines are shown as a guide-to-the-eye. Panels (c) and (d) are reprinted from [74] with the permission of AIP Publishing.

namely out-of-plane magnetized caps (see section 4.1.2) and soft-magnetic Py caps (see section 4.1.3), and providing an interlayer exchange coupling through a variable Pd spacer allows for imprinting non-collinear spin textures into the out-of-plane magnetized layers that resemble vortices, spiral domains and skyrmionic core textures (figure 13) [79]. These highly symmetric spin textures with distinct topology and tunable normal magnetization component/ opening angle offer interesting physical properties, such as core-tailored magnetization dynamics [290].

Layer stacks consisting of Pd(2)/[Co(0.4)/Pd(0.7)]$_5$/Pd(d)/Py(40)/Pd(2) with thicknesses in nm and variable Pd spacer thickness d ranging from 1 to 30 nm were prepared onto assemblies of non-magnetic SiO_2 spherical particles with a diameter of 500 nm. Changing the spacer thickness at small values ($d \lesssim 5$ nm) alters the magnetic properties of the Co/Pd spins, i.e. transforming the originally out-of-plane preferential orientation into an in-plane preference [79]. Utilizing XMCD with TXM and XPEEM, the magnetic states were imaged at remanence after applying magnetic fields $H = \pm 30$ kA m^{-1} perpendicularly to the sample surface. Figure 13 depicts simulated spin textures and experimental data revealing vortex, donut, spiral and saturated states with increasing Pd spacer thickness. Donut state type I (figure 13(b)) exhibits a white central region surrounded by a red area. The smallest observable core sizes range from 60 to 110 nm, which agrees well with 80 nm derived from micromagnetic simulations [79]. The experimental observation of these stabilized non-collinear spin textures at room temperature and remanence is intriguing as it provides means to reliably switch between donut state type I and type II with one and two domain walls, respectively (figures 13(b) and (c)), by applying out-of-plane magnetic fields below the switching field of the vortex core. The successful manipulation of donut states implies a switching of the skyrmion number S (also known as topological charge), i.e. between $S \approx 1$ and $S \approx 0$ [79], which might be appealing for prospective magnetic storage devices based on digital switching of topological charges.

Moreover, modifying topology of the imprinted states, interlayer exchange coupling and core sizes significantly alters the magnetization dynamics including gyro frequency and damping coefficients due to varying core masses [290] that can be described by the Thiele equation [292, 293]. The physical limitation to immobile skyrmionic core textures due to spatial confinement to cap or disk may be overcome by stabilizing non-collinear spin textures with controllable topological properties in extended non-planar honeycomb lattices [266]. The latter architectures are appealing for magnonic and spintronic applications due to stabilization of reconfigurable vortex circulation patterns with homocircular or staggered configuration (figure 14) [266]. The reconfigurability relies on the stray field contributions originating from

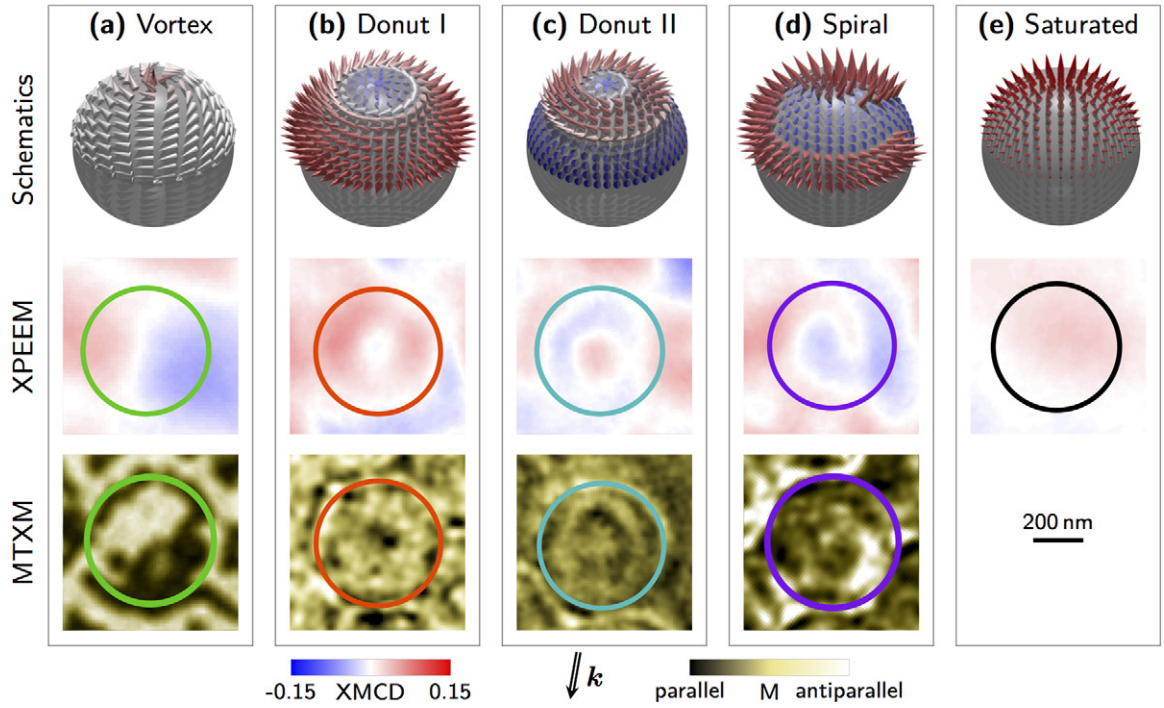

Figure 13. Experimental observation of imprinted non-collinear spin textures in hemispherical [Co/Pd]/Pd/Py caps using XPEEM and magnetic TXM (MTXM). Schematics illustrate corresponding state. Varying Pd spacer thickness leads to distinct states: (a) $d = 1$ nm: vortex; (b)–(d) $d = (4 \sim 5)$ nm: donut and spiral; (e) $d = 30$ nm: saturated. Circles indicate cap position with a diameter of 500 nm. XPEEM data is recorded at a constant x-ray beam incidence angle of 74° with respect to the surface normal. Out-of-plane and in-plane sensitivity of the MTXM data is provided by normal incidence and by tilting the sample 30° with respect to the x-ray beam, respectively. Reprinted with permission from [291].

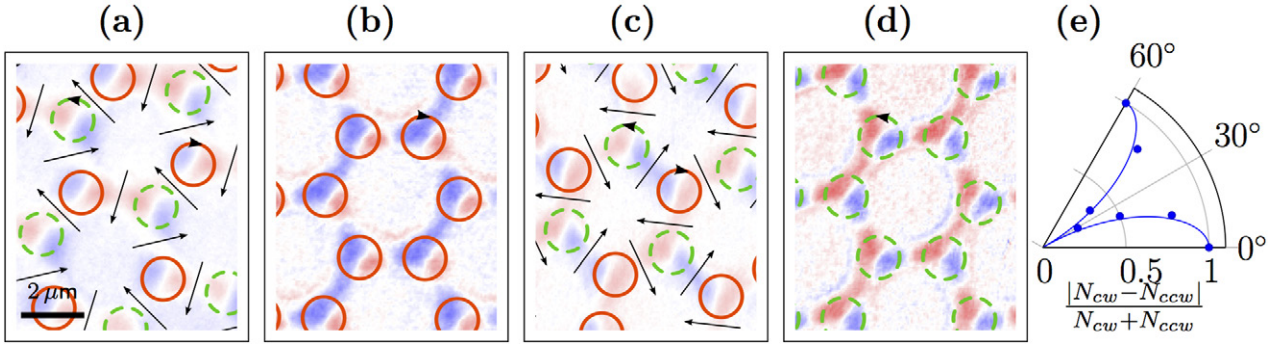

Figure 14. Reconfigurability of vortex circulation patterns in non-planar Py honeycomb lattices; Red-blue shading gives measured XPEEM data. (a) Staggered pattern obtained by ac-demagnetization. (b)–(d) Remanent state after field application along different directions: (b): 0°; (c): 40°; (d): 180°. The circulation sense of vortices is indicated by circles (red solid for clockwise, green dashed for counter-clockwise). Arrows show the orientation of wall sections between pairs of vortices. (e) Normalized difference between the number of vortices N_{cw} with clockwise (cw) and N_{ccw} counterclockwise (ccw) circulation as a function of the direction of the applied magnetic field. Symbols represent experimental data, connecting curve serves as a guide-to-the-eye. Reprinted with permission from [266]. Copyright (2015) by the American Physical Society.

the interplay between the height asymmetry of the vertices and the six-fold symmetry of the hexagonal honeycomb lattice. The latter one prefers a staggered arrangement with a vortex nucleation site located at the edge most normal to the applied magnetic field owing to a minimized energy of the magnetostatic surface charges. The essential requirement of these two competing mechanisms were confirmed by micromagnetic simulations and experimentally [266]. A demonstration of field- or current-driven displacement will require further optimization of structural and magnetic properties.

4.1.5. Magnetic data storage applications. In modern magnetic recording schemes, the bit patterned media (BPM) concept implies that one single bit of information is stored in an individual nanostructure with out-of-plane easy axis of magnetization, giving the possibility to significantly increase the areal density. However, even though there is an enormous progress in lithography techniques [294–299] it is rather challenging to create BPM with areal densities of about 1 Tbit/inch^2, equal to a pitch of 25 nm. This technological challenge has stimulated an intensive search for other ways to produce patterned templates using self-assembly techniques, such as

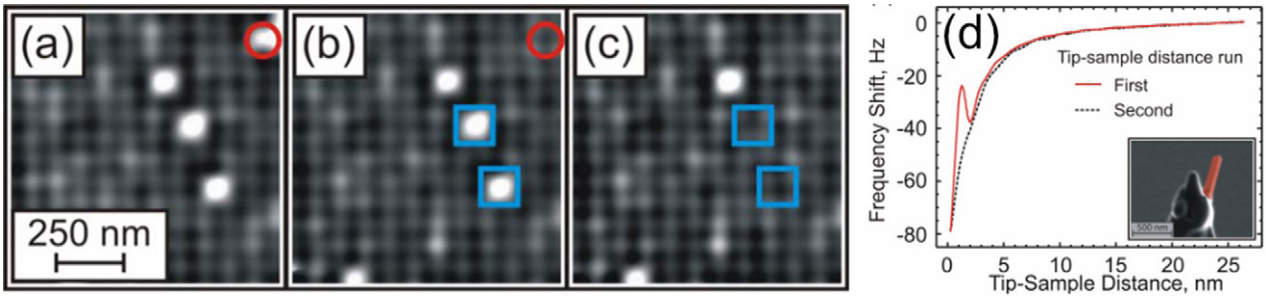

Figure 15. Probe recording on an array of nanocaps on 60 nm nanoparticles with a periodicity of 100 nm. (a)–(c) Series of MFM images demonstrating the capability to switch the magnetization of each dot (marked with a frame) via interaction with the tip from antiparallel (bright) to parallel (dark) configuration. (d) Force-distance curves displaying a kink when the magnetization of the nanocap switches. Inset depicts custom made rod-like tip used in the experiment. Reprinted from [276] with the permission of AIP Publishing.

anodized alumina (see section 5.1), phase separation in block co-polymers [300–303], surface instability induced by ion bombardment (see section 4.3), or self-assembled magnetic particles [304–307]. In this respect, deposition of magnetic thin films with out-of-plane easy axis of magnetization represents an attractive alternative to realize BPM [20, 58, 276]. Aside from fabrication challenges, methods to successfully write and read information in BPM need to be explored.

Writing requires a careful lateral adjustment of the recording head position on the track and the synchronization of write pulse to the media pattern [308, 309]. For this probe recording scheme, scanning tunneling microscopy and atomic force microscopy with a magnetic cantilever tip are promising techniques to read/ write information to each magnetic nanostructure [310]. Probe recording has also been achieved in nonmagnetic materials by either oxidizing the surface of the storage material, charge storage in semiconductors or forming indentations in polymers [311, 312]. However, these techniques suffer from the relatively slow reading and writing speed. Therefore, large scale parallelization of the tips is required to boost performance as demonstrated for example in the Millipede system [310, 311].

In order to perform probe recording on arrays of magnetic cap structures, MFM tips have to fulfill two critical requirements: The stray field of the MFM tip has to be sufficiently large to reverse the magnetization direction of the individual magnetic cap, and spatially confined (i.e. the stray field gradient has to be sufficiently steep) to preserve the magnetic state of adjacent magnetic nanostructures. The stray field of commercially available MFM tips (10 mT) is generally too weak for probe recording applications. In order to increase the tip's stray field, a series of MFM tips was specially manufactured by the group of H J Hug at EMPA (Dübendorf, CH) [276]. The largest stray field of 67.5 mT was achieved by using a 400 nm long Co rod with a diameter of 100 nm grown by electrochemical deposition inside an aluminum membrane and attached near the apex of the cantilever tip. The rod's apex was shaped into a cone with a diameter of <25 nm by focused ion beam etching to further confine its stray field (inset in figure 15(d)). In this study, template-directed self-assembly was employed to arrange spherical particles into a polymer resist template with periodically arranged holes, produced produced at the Paul Scherrer Institute (PSI Villigen, CH) using extreme ultraviolet interference lithography [276]. An array of magnetic caps was created depositing $[Pt(0.8\,nm)/Co(0.3\,nm)]_8/Pt(5\,nm)$ multilayers onto these patterns forming single domain cap structures with out-of-plane magnetization [276].

The proof-of-concept probe recording measurements were performed using a variable temperature UHV-MFM at a base temperature of 8 K operated by the group of H J Hug (EMPA, Dübendorf, CH). The magnetic state of the sample in an external magnetic field is presented in figure 15(a) revealing that the sample is almost magnetically saturated with only a few magnetic caps left with a reversed magnetization (in white) which were used for the probe recording trials. In order to initiate a magnetic writing event, the MFM tip was positioned over the nanocap. Then a force-distance curve was acquired by approaching the cantilever slowly in vertical direction (figure 15(d), red solid curve). The spectra shows a well-pronounced peak at a tip-sample separation distance of about 1.2 nm, indicating a magnetic switching event (island in red circular frame in figure 15(a)), which was confirmed by a subsequential MFM scan performed at larger tip-sample separation (figure 15(b)). The landing curve taken at the very same location after switching is featureless (figure 15(d), black dashed curve). Indeed, the presence of the peak in a force-distance curve is useful for tracking successful switching events in a magnetic probe recording concept. In addition, two further switching events are indicated by the blue square frames in figures 15(b)–(c), clearly demonstrating that using the field assisted probe recording approach, isolated single nanocaps can be switched in a controlled manner.

4.1.6. Magnetic cap structures in life sciences. Magnetic cap structures are not only fundamentally interesting, but also appealing for life science applications when functioning as self-propelled Janus micromotors due to feasible fabrication, tunable functionality and directionality of motion. Deterministic motion of autonomous self-propelled micromotors has emerged to a rapidly growing field because of its application relevance in medicine for targeted drug delivery [313, 314], hyperthermia for cancer treatment [315–317], microsurgery [318], etc. Catalytic propulsion of micromotors is one of the leading approaches in the field of intelligent synthetic micromachines [90, 317, 319–322]. Using a combination of magnetic and catalytic layers ensures a directed and autonomous motion in, for instance, H_2O_2. Redirecting

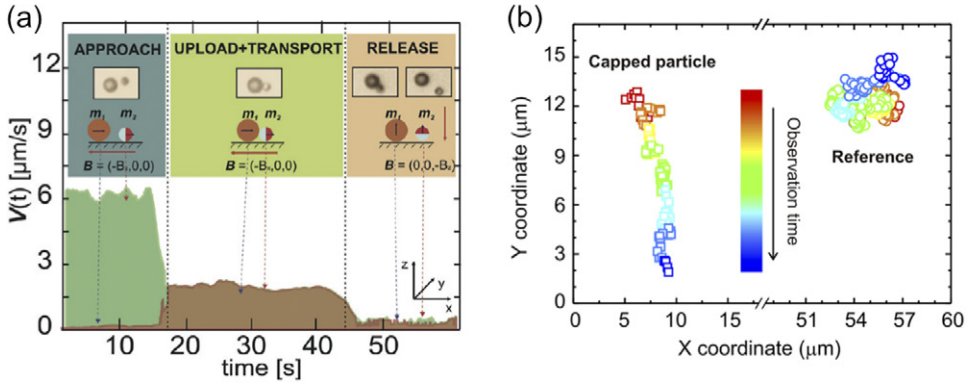

Figure 16. Magnetic cap structures applied as self-propelled micromotors for targeted drug delivery in life sciences. (a) Motion control via dc magnetic field of Janus particles with out-of-plane magnetization capped with a Pt layer to maintain catalytic reaction in H_2O_2. Velocity during all three steps of cargo transport: approach, pick up and transport, and release. Panel (a) is reprinted with permission from [69]. Copyright (2012) American Chemical Society. (b) Directional self-propulsion of Janus particles with a thick soft-magnetic cap driven by magnetically induced thermophoresis in water. Panel (b) is reprinted with permission from [68]. Copyright (2013) American Chemical Society.

the micromotor by means of magnetic fields requires a stable magnetic easy axis of the system usually given by its shape [322, 323].

An alternative route is to sputter deposit Co/Pt multilayer stacks with an out-of-plane magnetization directly onto monolayers of silica microbeads that resemble magnetic Janus particles [69]. An out-of-plane anisotropy provides magnetic field control, while the Pt (Pd) capping layer maintain the catalytic chemical reaction in H_2O_2. Targeted drug delivery, including pick up, transport and drop off, is achieved by reorienting the magnetic field and thus the Janus particle (figure 16(a); compare approach with release step).

In spite of numerous demonstrations, the catalytic concept suffers from the incompatibility of H_2O_2-based reactions with biological systems. Alternatives in liquid environment rely on various phoretic effects, such as electrophoresis [324, 325], diffusiophoresis [326, 327] and magnetophoresis [328]. Using Janus particles with thick soft-magnetic caps in combination with an ac magnetic field adds another phoretic effect, namely magnetically induced thermophoresis [68]. The heat generated by hysteretic losses (similar to those used for induction cooking) accumulates at the cap and induces a motion (figure 16(b)). The directed motion is ensured by the vortex polarity and a dc magnetic field.

In this case, amplitude of the ac field is limited by the vortex annihilation field to guarantee control over the trajectory. This restriction can be overcome by adding an out-of-plane magnetized film to the thick soft-magnetic layer. Avoiding any interlayer exchange coupling by choosing a thick spacer, keeps both subsystems independent of each other (see section 4.1.4) [79]. Distinct resonant frequencies for both subsystems would ensure a selected excitation of the soft-magnetic subsystem with potentially larger velocities.

4.2. Magnetically capped cylindrical objects

Confined cylindrically curved magnetic nanomembranes are fundamentally appealing, as curvature substantially alters magnetic properties like equilibrium magnetic domain patterns, magnetization reversal and magnetic coupling between neighboring magnetic segments. The latter, in turn, potentially allows one to overcome fundamental limitations imposed on the planar magnetic nanostructures. Applying rolled-up nanotech [87–90]—a strain engineering approach that exploits differential strain within a planar nanomembrane—provides means to fabricate on-chip integrable tubular architectures with cylindrical cross-section (see section 5.2). Curved magnetic cap structures are prepared by coating non-magnetic rolled-up tubes with a soft-magnetic 20 nm thick Permalloy ($Ni_{80}Fe_{20}$) film. Micromagnetic simulations and advanced characterization with XPEEM were carried out to probe the characteristic magnetic states (figure 17). Coming from long to short tube segments, the contrast transforms from uniform (bluish/reddish) over multi-domain (X-shape, Landau pattern) to uniform (white) highlighting the transition from longitudinal to azimuthal domain patterns via Landau/ vortex states, respectively. The curvature-driven thickness gradient of the magnetic nanostructures avoids stray fields perpendicular to the tube axis and reduces interaction between neighboring magnetic nanostructures. This feature preserves the vortex state, which is a bottleneck of planar stripes. Thus, a much larger areal density of magnetic wires compared to planar stripes might be achieved, which is beneficial e.g. to increase storage density of racetrack memory devices.

4.3. Ion beam-induced templates

Bottom-up approaches employing pre-structured templates prepared by self-organizing processes provide cost- and time-efficient nanostructuring throughout large areas [61, 329–334]. For example, the strain-induced growth of $Si_{1-x}Ge_x$ films on Si(0 0 1) leads to self-assembled patterns of nanopyramids, whose facets can be magnetically covered by shadow deposition [61, 335, 336]. Alternatively, regular patterns of densely packed nanostructures with a characteristic periodicity can be realized by low-energy ion beam sputtering of semiconductor and oxide surfaces [61, 337, 338] and subsequent pattern transfer to a magnetic film deposited on top [64, 331]. The formation mechanism of regular patterns at the nanoscale by ion beam irradiation relies on a self-organization process,

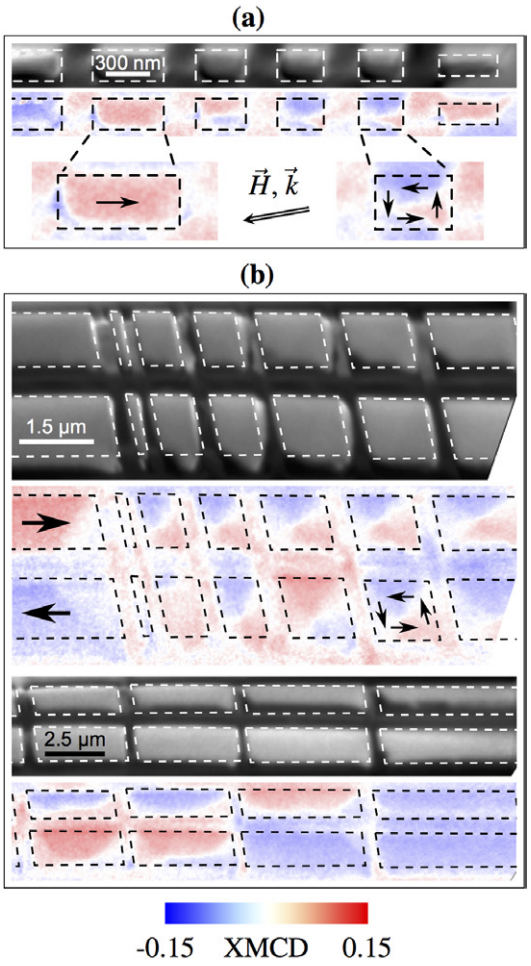

Figure 17. Magnetic equilibrium states in Py cap structures. XMCD-PEEM contrast with corresponding PEEM image for 20 nm thick Py caps on non-magnetic rolled-up nanomembranes (indicated by dashed rectangles) with a diameter of (a) 250 nm and (b) 1.7 μm. Red- and blue-colored regions refer to in-plane magnetization components with the orientation indicated by the arrows. The incidence angle of the beam is illustrated in (a). Coming from long to short tube segments, the contrast transforms from uniform (bluish/reddish) over multi-domain (X-shape, Landau pattern) to uniform (white) highlighting the transition from longitudinal to azimuthal domain patterns via Landau/ vortex states, respectively. From the arrangement of the vortex chirality in (b), an anisotropic magnetostatic interaction between neighboring Py caps is observed due to the curvature-driven thickness gradient. Reprinted with permission from [57]. Copyright (2012) American Chemical Society.

governed by the competition between roughening and smoothing due to ion sputtering and surface diffusion, respectively [339–343]. Examples of nanoscale periodic surface patterns range from ripples on Si [344] and MgO [62] over antidots in Ge [345] to GaSb nanocones [337] and dots [333], and various other nanostructures [346].

4.3.1. Geometrical tuning of the magnetic exchange coupling parameter at the nanoscale. Regular patterns of densely packed cone-like nanostructures can readily be prepared from a standard GaSb(0 0 1) wafer facilitating ion beam erosion [337]. Sputtering of the surface is carried out by a defocused Ar^+ ion beam directed normal to the surface. Tuning the energy of Ar^+ ions allows for producing nanocones with different dimensions. For instance, templates with a cone diameter of 28 nm and height of 32 nm were prepared using Ar^+ ions with a kinetic energy of 200 eV [64]. Growing CoCrPt:SiO_2 granular films onto GaSb nanocone templates with different cone sizes and periodicities provided means to study geometrical tailoring of the magnetic exchange coupling parameter [64]. These films have a high uniaxial magnetic anisotropy of about 5×10^6 erg/cm^3 [64, 347] and are used as a conventional magnetic recording material in the hard-drive industry [348]. The CoCrPt:SiO_2 films were optimized to consist of weakly exchange interacting magnetic single-domain grains separated by a SiO_2 shell.

A closer look at the morphology of the magnetic film by cross-sectional TEM reveals strong impact of the cone size (figure 18). Small columnar grains with a diameter of 5 nm cover the top of small cones (figure 18(a)). They even connect neighboring cones, as the closely packed stack is 44 nm high, which is thicker than the height of the cones. The CoCrPt:SiO_2 grains are tilted up to 20° with respect to the sample's normal (figure 18(a)). In contrast, larger cones ensure grain growth on the sidewalls of the cones (figures 18(b) and (c)). The easy axes are oriented predominantly normal to the local cone surface. A thickness variation of the stack emerges with 6 nm at the bottom between the cones and 15 nm (nominal thickness) near the top.

These distinct structural properties are reflected by the magnetic domain pattern characteristic of the samples. The sample with the smallest cone size reveals large magnetic domains (of about (40 ∼ 100) nm in width) that extend over several nanocones (figures 19(a) and (d)). Samples with larger cones show dark and bright spots each confined to a single cone (figures 19(b), (c), (e) and (f)). Correlating MFM with AFM and TEM proves an exchange coupling between grains on adjacent cones for small periodicity, which is absent for larger ones.

4.3.2. Geometry-induced crossover between surface and volume anisotropy. Nanoripple templates are obtained by irradiating Si(1 0 0) with Ar^+ or Xe^+ ions with an energy in the range of (0.3 ∼ 15) keV at an incident angle of 67° with respect to the surface normal and at a constant ion fluence of $(0.2 \sim 2) \times 10^{18}$ ions cm^{-2} [63]. Those conditions lead to self-organized ripple templates with a wavelength of (25 ∼ 90) nm and an average amplitude range of (1.5 ∼ 5) nm (figure 20) [63, 349, 350].

Growing polycrystalline Fe, Ni and Co with different thicknesses onto such ripples induces uniaxial magnetic anisotropy along the ripple crest direction [61, 63]. A thickness dependence study [63] identified two characteristic regions either governed by uniaxial surface or volume anisotropy. In the low thickness range of a few nanometers, the magnetization tries to follow the surface corrugation even though it never perfectly aligns with the surface morphology. Above the critical thickness of the SRT, dipolar stray fields originating from the surface determine the uniaxial anisotropy.

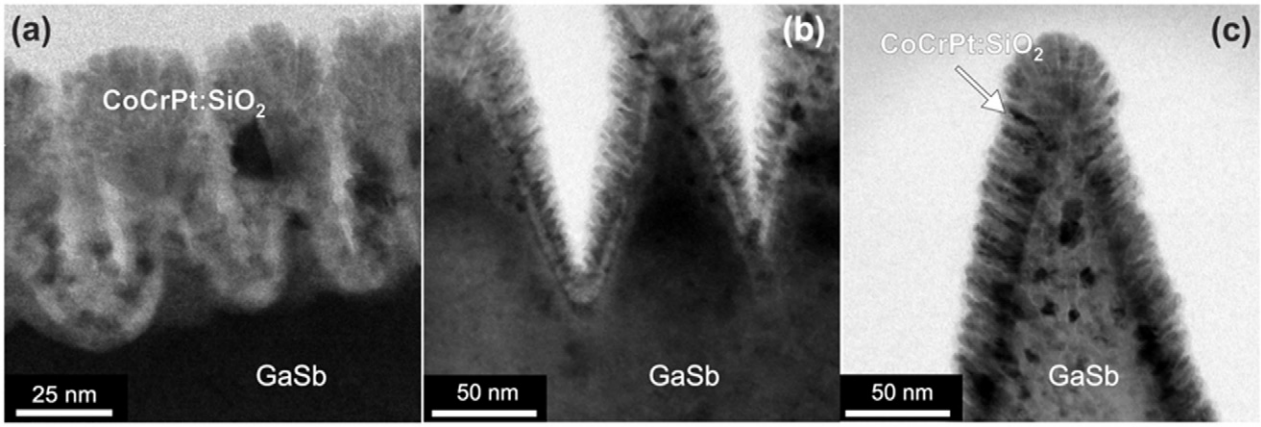

Figure 18. Cross-sectional TEM images of 15 nm thick CoCrPt:SiO_2 films (total thickness of the layer stack with auxiliary layers is about 45 nm) deposited on pre-structured GaSb(0 0 1) processed by Ar^+ ions irradiation with an energy of (a) 200 eV, (b) 800 eV and (c) 1200 eV. SiO_2 concentration is (a) 8 at.% and (b), (c) 12 at.%. Reprinted with permission from [64].

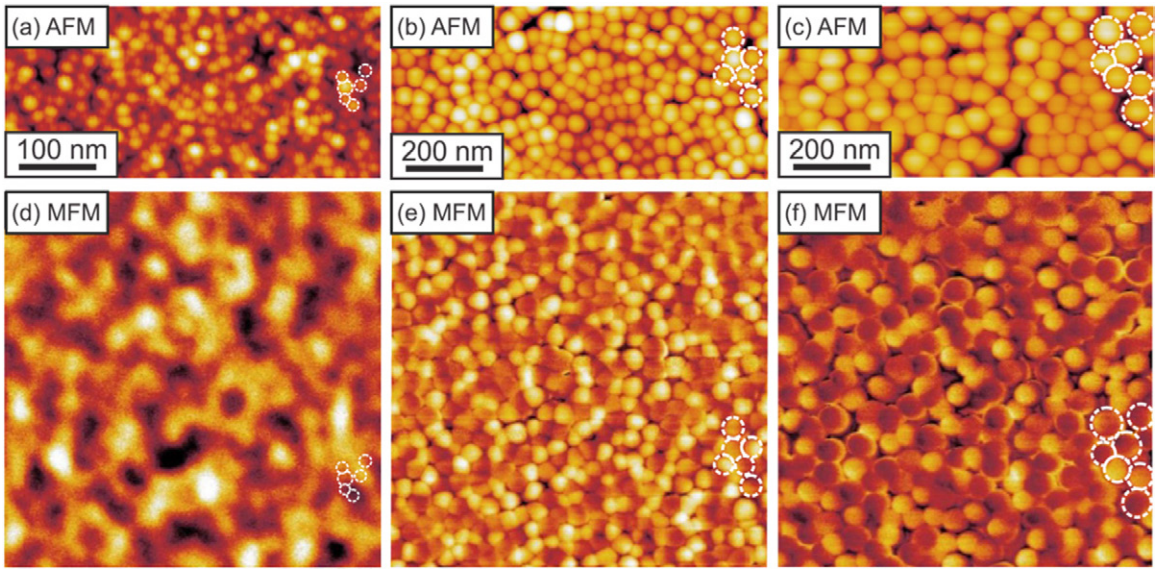

Figure 19. (a)–(c) AFM images and (d)–(f) corresponding MFM images of the demagnetized state of CoCrPt:SiO_2 coated nanocones (8 at.% SiO_2) prepared with ion energies of (a), (d) 200 eV, (b), (e) 800 eV, and (c), (f) 1200 eV. The circles indicate corresponding positions in the AFM and MFM images. Reprinted with permission from [64].

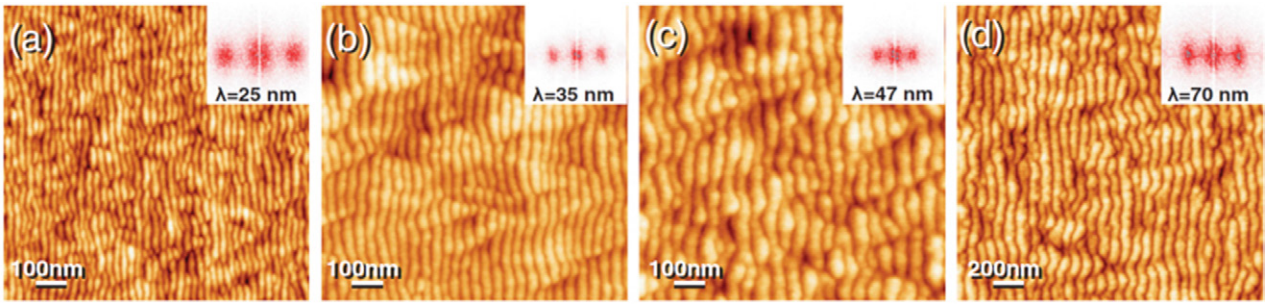

Figure 20. AFM scans of Si nanoripple templates with different ripple wavelengths. Insets show the corresponding 2D power spectrum density plots providing access to the wavelength λ of the pattern. Reprinted with permission from [63]. Copyright (2013) by the American Physical Society.

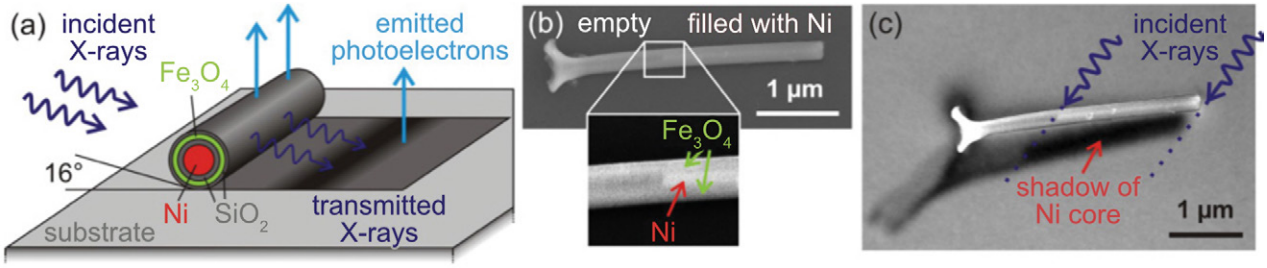

Figure 21. (a) Schematic of a core-shell wire during XPEEM imaging. (b) Scanning electron micrograph of an iron oxide tube partially filled with a nickel core. The blow up shows the transition from the empty tube (left) to the nickel core (right) that appears bright. (c) XPEEM image recorded at the nickel L_3 edge overlaid with SEM of the nanowire. The absorption of the nickel core can be distinguished in the shadow of the wire. Reprinted with permission from [52]. Copyright (2011) by the American Physical Society.

5. Tubular shaped objects

5.1. Cylinders and hollow tubes

The experimental realization of cylindrical magnetic objects is very demanding as high-quality films with acceptable surface roughness and well-defined magnetization textures are required to avoid domain wall pinning on imperfections, such as grain boundaries and edges, that may overshadow curvature effects.

Cylindrical structures may be fabricated by different synthesis approaches. Rods and tubes with diameters in the nanometer range are typically prepared via electro-chemical deposition into porous alumina templates [28, 48, 55, 75, 351]. These objects possess, due to small dimensions, rather simple domain patterns, e.g. longitudinal or azimuthal magnetization, and may successfully be studied using electron holography [76, 77] or magnetometry [28, 351]. While soft-magnetic nanocylinders with diameters $\varnothing \lesssim 50$ nm favor transverse domain walls as predicted by micromagnetic simulations, rods with larger dimensions reveal more complex spin textures with vortices located near structural defects [76], suggesting strong pinning and the disability to efficiently displace domain walls. This assumption was confirmed by cantilever magnetometry observing various metastable states in tubes with inner and outer diameters of $\varnothing_{in} \approx 200$ nm and $\varnothing_{out} \approx 300$ nm, respectively [28].

5.1.1. Imaging inner magnetization textures in tubular nanoobjects. Extending conventional XPEEM (section 3.3) imaging by a transmission experiment makes it possible to record magnetic information originating from both surface and internal components of a nanostructure and to separate those two contributions [52, 103, 352]. The capability of this approach was first demonstrated by Kimling *et al* [52] using magnetic core-shell nanowires. Such multilayer nanowires are synthesized filling the hexagonally ordered pores of an alumina membrane with different materials and various techniques [53]. Firstly, the pores are coated with SiO_2(5 nm)/Fe_2O_3(12 nm)/SiO_2(10 nm) by atomic layer deposition. Then, nickel is electrochemically deposited into the pores. The nickel core has a diameter of about 100 nm, which is determined by the pore diameter and the thickness of the shell layers. The schematic of a core-shell wire on a silicon wafer exposed to an x-ray beam hitting the sample surface at a shallow angle is shown in figure 21(a). Secondary photoelectrons emanate from the surface of wire and substrate with an intensity depending on the internal structure of the nanowire (figure 21(a)). Figure 21(c) depicts the overlay of a scanning electron micrograph and a XPEEM image recorded at the nickel L_3 edge. The nickel core can clearly be distinguished in the shadow of the structure due to resonant absorption. The nanowire is tilted by 45° with respect to the in-plane projection of the incident x-ray beam offering sensitivity to both azimuthal and longitudinal magnetization components and thus capabilities to image the magnetization reversal. In contrast, an angle of 90° would enlarge the shadow while providing a sensitivity only to the magnetization component perpendicular to the wire axis. Similarly, an angle of 0° reveals longitudinal magnetization components but projects the shadow underneath the nanowire preventing any means of detection.

Figure 22(a) shows XPEEM images of the core-shell wire recorded at the L_3 absorption edges of iron and nickel after background subtraction. Figures 22(b)–(e) are pairs of XMCD images (calculated according to (8)) visualizing the magnetization reversal process in both iron oxide shell (left) and the nickel core (right). The blue and red XMCD contrasts are proportional to the magnetization parallel and antiparallel to the direction of the in-plane projection of the incident x-ray beam, respectively. At the iron edge, magnetic contrast can be obtained from both wire and its shadow. The contrast in the shadow is inverted as the electron yield from the substrate is proportional to the intensity of the transmitted x-rays. At the nickel edge magnetic contrast can only be observed in a segment of the shadow.

5.1.2. Topologically protected magnetic textures in tubular nanoobjects. Bloch points are topologically protected 3D magnetic textures. The magnetization distribution of such a spin texture mapped onto a sphere cannot be described by a continuous magnetization field of finite magnitude. This applies e.g. to hedgehog and skyrmion configurations or more generally whenever all directions of magnetization can be mapped on a closed surface. The existence of Bloch point walls (BPWs) has been experimentally confirmed very recently. Da Col *et al* [352] used the XMCD shadow contrast in XPEEM to gather both surface and volume information of the magnetization configuration of domain walls in cylindrical nanowires. For

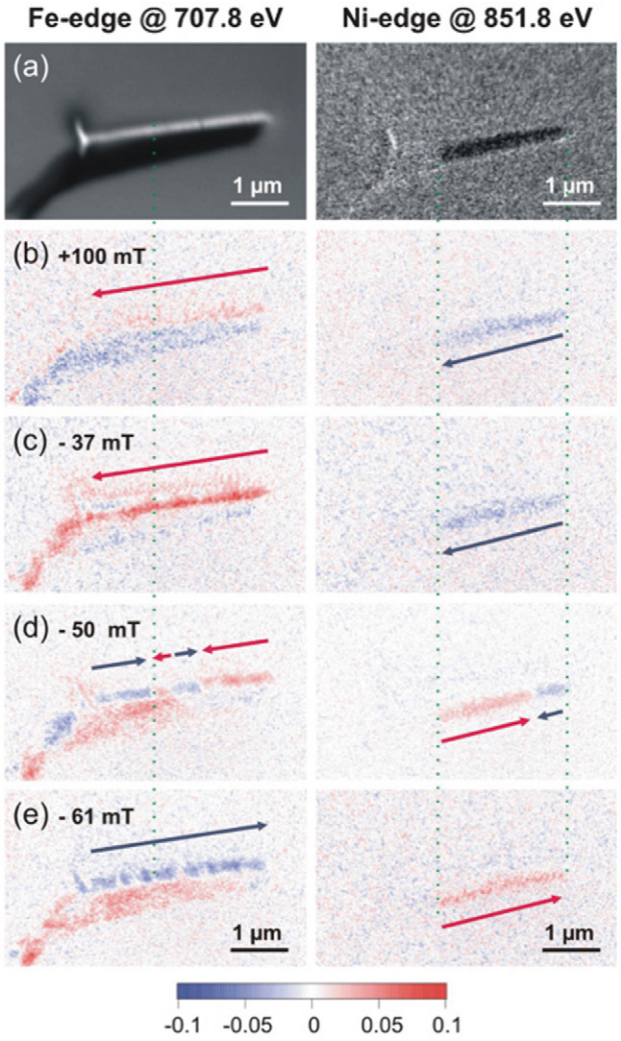

Figure 22. (a) XPEEM images of the core-shell wire recorded at the L_3 absorption edges of iron and nickel (background extracted). (b)–(e) XMCD images of the iron oxide tube (left) and the nickel core (right) recorded at various in-plane magnetic fields aligned along the x-ray propagation direction (45° with respect to the tube). The color bar indicates the direction of the magnetic contrast in arbitrary units. The arrows indicate the magnetization components along the wire axis. The green dotted lines mark the ends of the nickel core. Reprinted with permission from [52]. Copyright (2011) by the American Physical Society.

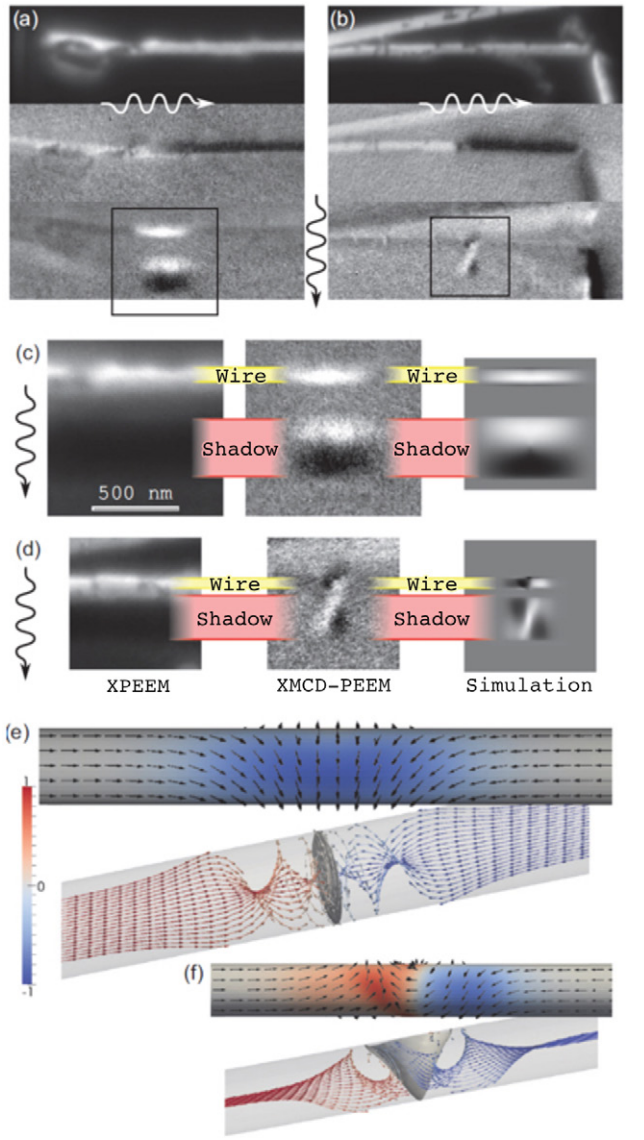

Figure 23. Identification of Bloch-point and transverse domain walls based on correlation of XPEEM with simulations. (a), (b) In each are three views of the same wire, at the same location and with a field of view (3 × 1) μm^2. From top to bottom: total absorption and XMCD contrast parallel and across the wires. (c), (d) From left to right: XPEEM (sum of images for the two polarizations), XMCD (enlargement of the square areas in (a) and (b)), and simulations of two DWs at the Fe L_3 edge. The photons arrive from the upper part of the images. (c) A wire of diameter 95 nm lifted 80 nm above the surface, with a Bloch-point type DW. (d) A wire of diameter 70 nm lifted 25 nm above the surface, with a transverse DW. (e), (f) Top and open view of the micromagnetic state used in the right parts of (c) and (d), with wire diameter 95 and 70 nm, respectively. Reprinted with permission from [352]. Copyright (2014) by the American Physical Society.

this study, micrometers-long Permalloy nanowires were electroplated in self-organized anodized alumina templates with modulated diameter of pores along their length [353].

In a first step, the wires are aligned along the x-rays to identify longitudinal domains and thus to determine the location of domain walls (DWs) (figures 23(a) and (b); top rows). In a second step, the sample is rotated by 90° to align the wires perpendicularly to the x-ray trajectory. With these conditions, contrast solely arises from DWs (figures 23(a) and (b); bottom row). By these means, two well-defined families of DWs were observed with typical examples depicted in figures 23(c) and (d). The first class is characterized by an orthoradial curling of magnetization (identified from XMCD shadow contrast), which is symmetric with respect to a plane perpendicular to the wire axis (directly from wire) (figure 23(c)). Notice the absence of contrast on the axis, as expected for the presence of a Bloch point (figure 23(e)). The second type of DW breaks the aforementioned symmetry and is characterized by a uniform contrast at the center of the DW, in the vicinity of the wire axis (figure 23(d)). This is a fingerprint of transverse walls (TWs) (figure 23(f)). Consistent with theoretical predictions [354], wires with a large diameter reveal Bloch point walls,

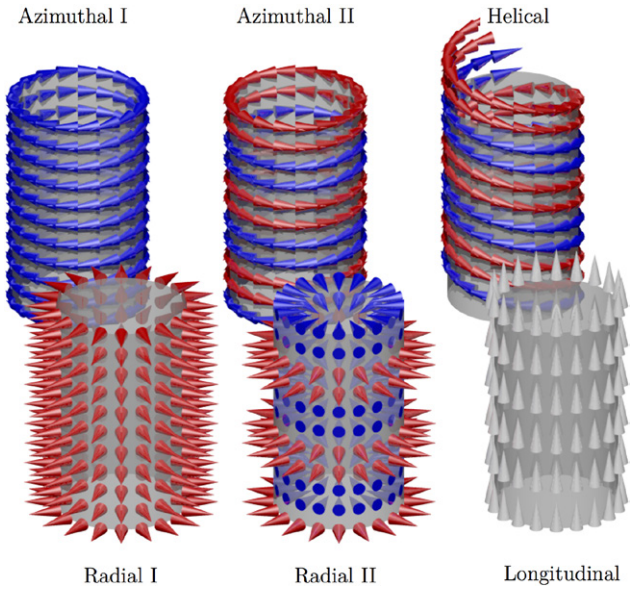

Figure 24. Schematics of magnetic domain patterns in ferromagnetic thin films resembling hollow cylinders. Top row: Circulating (in-plane) magnetization textures without (azimuthal) and with (helical) longitudinal components. Circulation sense is indicated by red or blue. Bottom row: Radial and longitudinal magnetization configuration. State radial II illustrates multidomain states with radially magnetized domains. Each configuration possessing distinct magnetic and magnetoelectric properties can be fabricated by rolling up planar films. Reprinted with permission from [291].

while small wires favor TW. The crossover diameter is in the range of $(70 \sim 90)$ nm.

5.2. Rolled-up magnetic nanomembranes: magnetic Swiss rolls

More complex, yet deterministic, domain patterns (figure 24) appear in tubular architectures with diameters in the lower micrometer range fabricated by strain engineering rolled-up nanotech. Rolled-up nanotech [87, 88] relies on differential strain in thin solid films deposited on top of a sacrificial layer (figure 25). Such systems can be realized by single materials (e.g. partially strain relaxed Si films), by bilayers of the same material class (InGaAs/GaAs bilayer [355]) or different material classes (InGaAs/metal [356, 357]). The membranes to be rolled-up are defined by either lithography patterning or mechanical scratching. The layer system is released from the substrate by e.g. wet chemical underetching. The strain gradient generates a bending moment to (partially) relax and initiates the rolling of the layer system. It is possible to design a strained layer system and to deposit an additional layer, e.g. magnetic materials. The functional layer inherits the radial symmetry of the rolled-up layer [358]. The resulting microscopic structure of these rolled-up nanomembranes resembles Swiss rolls, which are morphologically and topologically distinct to the cylinders and hollow tubes.

Rolled-up tubes with diameters down to only a few nanometers can be fabricated using strained semiconductor and sacrificial layers [359]. In this case, the samples consisting of

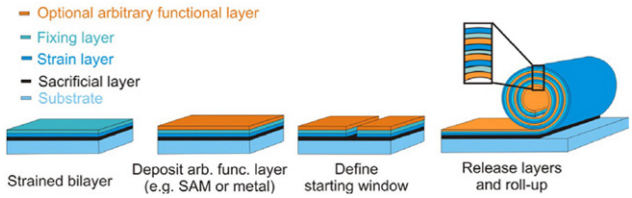

Figure 25. Schematic illustration of the fabrication of rolled-up tubes. An initially strained layer system is deposited on top of a sacrificial layer. An optional, arbitrary functional layer can be deposited on top. To obtain a rolled-up tube, a starting window is defined and the layer structure is released from the substrate by selective underetching. Reprinted with permission from [358].

epitaxial In(Ga)As/GaAs bilayers with different total thicknesses are grown using molecular beam epitaxy (MBE). The rolling process includes *ex situ* selective etching performed with diluted HF solutions enabling a selectivity to AlAs [360, 361]. Typical SEM images of the InGaAs/GaAs rolled-up tubes are shown in figure 26. Furthermore, the scaling of the nanotubes diameter with the total InAs/GaAs bilayer thickness is presented in figure 26(c) revealing the possibility to obtain rolled-up tubes with diameters down to several nanometers.

As small tube diameters can be achieved relying on lattice mismatched epitaxially grown superlattices, much efforts were devoted to optimizing the growth of magnetic-material-containing heterostructures to fabricate rolled-up magnetic nanomembranes of small diameters. Heusler alloys are compatible with compound and elemental semiconductors [362, 363] and provide as half-metallic compounds a spin polarization at the Fermi level of up to 100% [364–366], which is highly relevant for prospective spintronic applications. In particular, binary intermetallic Fe_3Si from the family of Heusler alloys can be grown on GaAs(0 0 1) substrates at nearly perfect lattice match [367–369]. Even for good crystalline quality of the radial superlattices (figure 27), e.g. in the case of InGaAs/Fe_3Si superlattices [100, 370, 371], typical diameters of the rolled-up architectures are 1.2 μm [371]. To form an epitaxial bilayer, the MBE-grown III–V surface of InGaAs is thermally deoxidized and a 20 nm-thick Fe_3Si layer is grown pseudomorphically on top of the InGaAs layer by coevaporation of Fe and Si at 350°C in a separate thermal evaporation chamber. Although the structural characterization reveals clear pseudomorphic growth of Fe_3Si on InGaAs and even indicates a lattice-matched crystalline bonding of the two layers (figure 27), no distinguishable interface region is observed as would be expected from other semiconductor/metal [357] or semiconductor/semiconductor rolled-up stacks [355, 372–374]. We speculate that by tuning the deposition conditions, growth temperature or thickness of Fe_3Si, one would be able to achieve tubes with smaller radii.

Similar diameters of Swiss rolls in the range of 4 μm are achievable when preparing heterostructures of strained semiconductor bilayers, e.g. InGaAs/GaAs with a ferromagnetic metal layer, e.g. Permalloy [41, 42, 104]. After rolling up, those structures (figure 28(a)) resemble novel ferromagnetic microtube ring resonators. Balhorn *et al* [41] investigated the spin-wave spectrum using high-resolution microwave

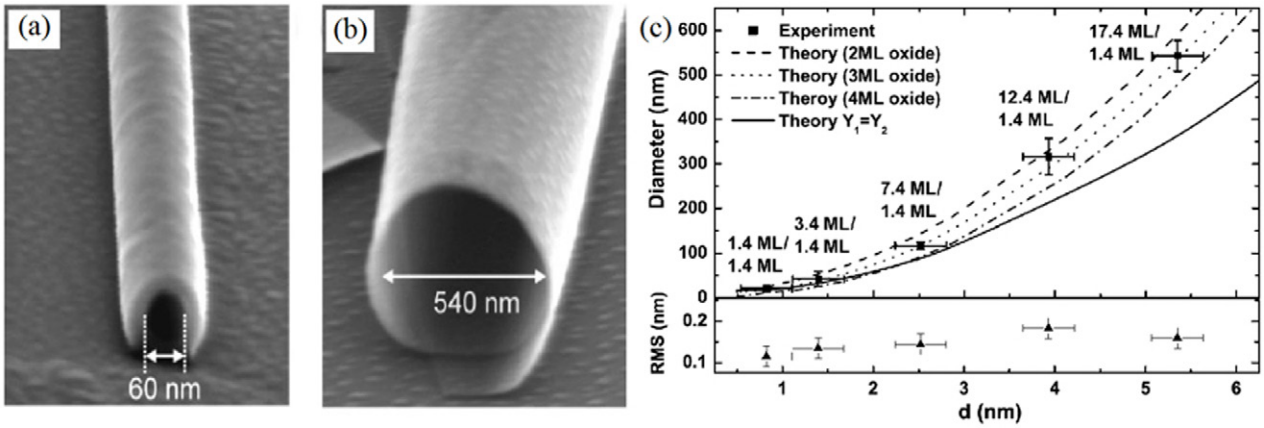

Figure 26. Typical tube openings consisting of the following as-grown bilayers: (a) 1.4 ML $In_{33}Ga_{67}As$/6.4 ML GaAs, (b) 14.1 ML $In_{33}Ga_{67}As$/19.1 ML GaAs. (c) InAs/GaAs tube diameter as a function of bilayer thickness. Bilayers were chosen highly asymmetric (see labeling for each datapoint). RMS roughness of surfaces is given in the bottom graph. Reprinted with permission from [359].

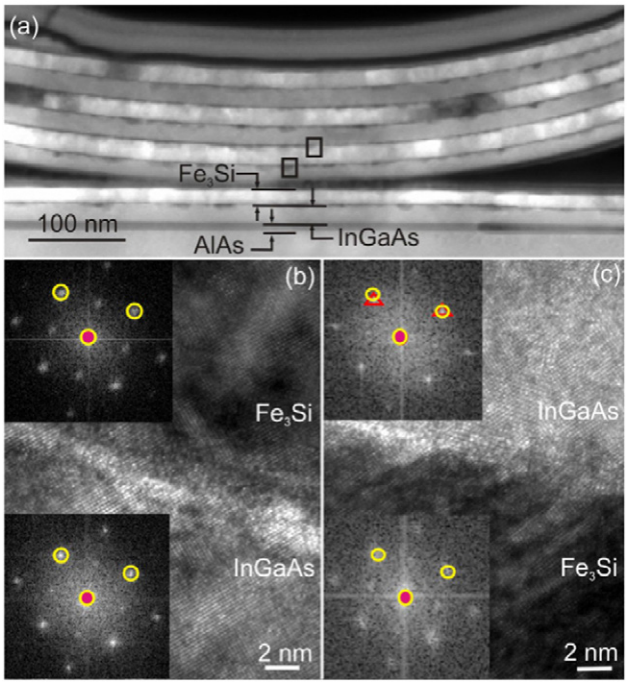

Figure 27. (a) Transmission electron microscopy (TEM) image of an InGaAs/Fe_3Si radial superlattice as well as the unreleased layer. The diameter of the tubular object is 1.2 μm. The positions of the high-resolution TEM (HRTEM) images are marked by rectangles. (b) HRTEM of the InGaAs/Fe_3Si growth interface as well as FFT of the lattices of InGaAs and Fe_3Si layers. Both HRTEM image and FFT indicate a clear pseudomorphic interface of the two layers and a corresponding relation of the lattice. (c) HRTEM image of the Fe_3Si—InGaAs bonding interface. Note the direct crystalline bonding and the small misalignment indicated by the FFT between the adjacent windings of the radial superlattice. Reprinted with permission from [371].

absorption spectroscopy. For the tube with a given diameter d and number of windings, four distinct resonances have been observed (figure 28(b)–(e)). The resonances in the spectra are found to be due to spin waves traveling around the tube perimeter. They form resonant modes $n = 0; 1; 2; \ldots$ if the periodic boundary condition for a ring resonator $n\lambda_s = \pi d$ is fulfilled. Here λ_s denotes the wavelength of the spin wave. It is important to note that due to the strong dipole–dipole interaction between windings, Swiss rolls behave magnetically as a single-layered tube with an effective thickness. The magnetostatic coupling automatically leads to a renormalization of the spin-wave mode frequencies as compared to a single-layered film.

The validity of this assumption was proven by imaging the magnetic domain pattern in tightly wound Swiss roll architecture (see section 5.2.1) [103].

5.2.1. Layer specific imaging of tubular magnetic objects. The crucial aspect of identifying domain patterns in buried magnetic films is exemplarily demonstrated for tightly and loosely wound rolled-up nanomembranes with a winding separation of about 200 nm. The curved thin films consist of $In_{33}Ga_{67}As(5)$/GaAs(5.6)/Py(15) layer stacks with units in nanometer and diameters $\varnothing \lesssim 3$ μm. The 11 nm-thick non-magnetic capping layer prevents Ni and Fe photoelectrons from leaving the surface due to inelastic scattering while lowering the x-ray beam intensity by merely 2% [103]. Thus, information about the magnetization can only be obtained in transmission by analyzing the XMCD shadow in XPEEM contrast at the back side of the 3D object. This possibility further enables an on-chip characterization of optionally encapsulated magnetic devices without the need to transfer them onto transparent nanomembranes as required for TXM.

5.2.2. Tightly wound rolled-up nanomembranes. The projected images of the magnetization in tightly wound rolled-up nanomembranes reveal large domains with a magnetization pointing either along or perpendicularly to the symmetry axis (figure 29). The dash-dotted lines enclose the shadow region of the tube located at the top. The magnetization components along the x-ray propagation direction, namely 45°, are color-coded in blue/ red. Note that white refers to a vanishing *net* XMCD signal originating from either a perpendicularly aligned magnetization or contrast compensation due to the penetration of x-ray beams through multiple windings with opposed magnetization orientations.

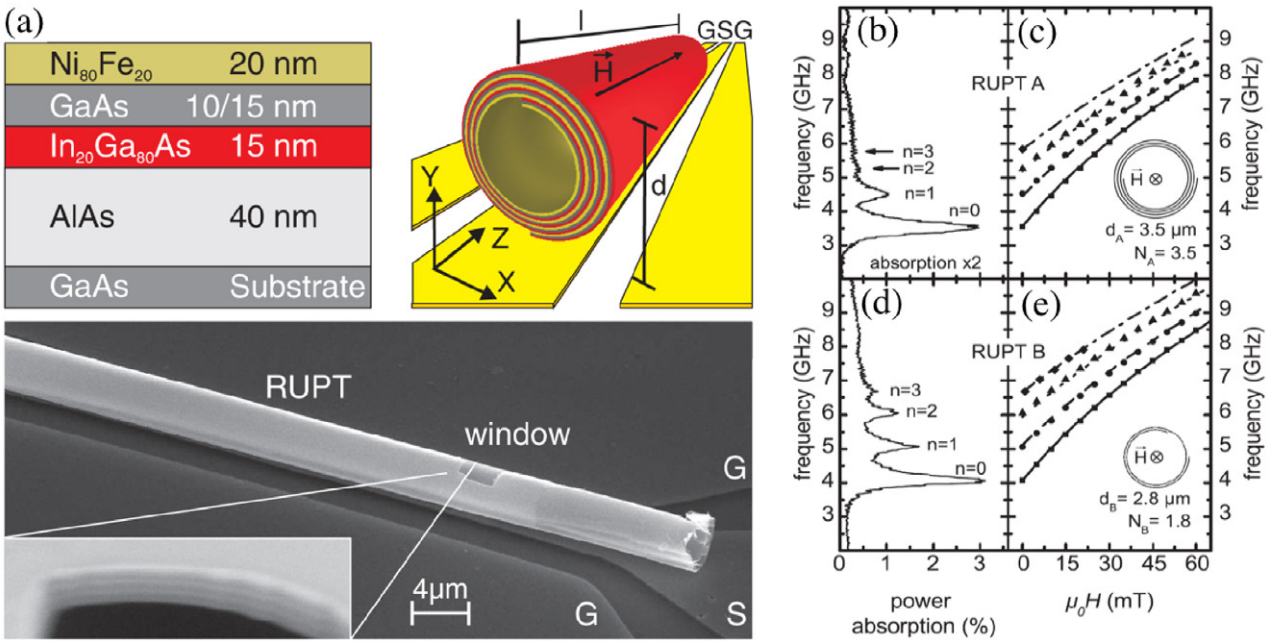

Figure 28. Ferromagnetic microtube ring resonator by rolling up a $Ni_{80}Fe_{20}$/GaAs/$In_{20}Ga_{80}As$ layer system (RUPT). (a) Layer stack, schematics and SEM image of RUPT positioned on the signal line (S) between the two ground lines (G) of a coplanar waveguide to perform microwave absorption measurements. The inset shows 3.5 tight windings of the strained layer system in a tube cross-section prepared by focused ion beam etching. (b)–(e) Ferromagnetic resonance spectroscopy of RUPT. (b) and (d) show microwave power absorption spectra at remanence for two Swiss roll architectures with different diameters d and number of windings N (see schematics in the inset). In both cases, four successive resonances corresponding to azimuthal spin-wave modes with number $n = 0;1;2;3$ can be identified. (c) and (e) show the magnetic field dependence of the measured resonance frequency peaks indicated by symbols. Lines plot the theoretical results derived by a spin-wave interference model. The magnetic field points along the tube axis. Reprinted with permission from [41]. Copyright (2010) by the American Physical Society.

An identification of the corresponding magnetization patterns were done by performing XMCD shadow contrast simulations taking into account a magnetization-dependent absorption of the circularly polarized x-ray beam penetrating a magnetic tube. The magnetization field is analytically defined on the tube assuming uniform distributions, such as longitudinal and azimuthal magnetization alignments. The absorption coefficient for (anti-)parallel alignment is approximated in first order as [103]:

$$\mu_{\pm} = \mu_{\pm}^{\mathrm{Fe}} \frac{a_{\mathrm{Fe\ in\ Py}}}{a_{\mathrm{Fe}}} + \mu_{\pm}^{\mathrm{Ni}} \frac{a_{\mathrm{Ni\ in\ Py}}}{a_{\mathrm{Ni}}}, \tag{9}$$

with the atomic density a. The individual absorption coefficients are estimated based on the work of Stöhr *et al* [115] (i.e. $\mu_{+}^{\mathrm{Fe}} \approx 1\ \mu\mathrm{m}^{-1}$, $\mu_{-}^{\mathrm{Fe}} \approx 5\ \mu\mathrm{m}^{-1}$, $\mu_{\pm}^{\mathrm{Ni}} \approx 3\ \mu\mathrm{m}^{-1}$ at the Fe L_3 absorption edge). Please note that μ_{+}^{Ni} and μ_{-}^{Ni} are the same at the Fe L_3 absorption edge due to non-resonant excitation. Contributions from the non-magnetic layers of 2% are neglected. The effective absorption coefficient is obtained by linear interpolation between $\mu_{\perp}$ and μ_{+} with the scalar product of magnetization $\boldsymbol{M}$ and x-ray propagation direction $\boldsymbol{k}$:

$$\mu_{\pm}^{*} = \mu_{\pm} + (\mu_{\mp} - \mu_{\pm})\frac{1}{2}(\boldsymbol{M} \cdot \boldsymbol{k} + 1). \tag{10}$$

The accordingly defined intensity at each point j of the tube is multiplied along the x-ray propagation direction and projected onto a plane representing the substrate.

The good correspondence between experiment and simulation suggests that indeed tightly wound rolled-up nanomembranes with multiple windings can be treated as a tube [42] with a magnetostatically driven commensurable domain pattern throughout all windings [103]. The conclusion on the strong magnetostatic coupling between the windings should be taken with care. Rolling up could result in a Swiss rolls with rather large voids between windings in the range of 100 nm. In this case, windings behave magnetically independent, each possessing its own magnetic domain pattern [103].

5.2.3. Loosely wound rolled-up nanomembranes. The capability to resolve layer specifically magnetic domain patterns is demonstrated on the example of rolled-up nanomembranes with loosely wound layers separated by approximately 200 nm. The corresponding XMCD signal of the object consists of narrow stripes aligned along the symmetry axis which refer to the magnetic contrast originating from each winding (figure 30). As the shadow contrast is analyzed on top of a uniformly magnetized planar Py film, an additional but non-disturbing offset has to be considered. The central shadow region refers to layers that experience mainly perpendicular magnetic field components. Hence, contrast changes appear at larger fields. Contrarily, the contrast at the edge of a winding fades and reverses at field values $H_c = (-1.3 \sim -1.0)\,\mathrm{kA\ m^{-1}}$ similar to those obtained by magnetooptical Kerr effect magnetometry [103]. The larger XMCD signal originating from

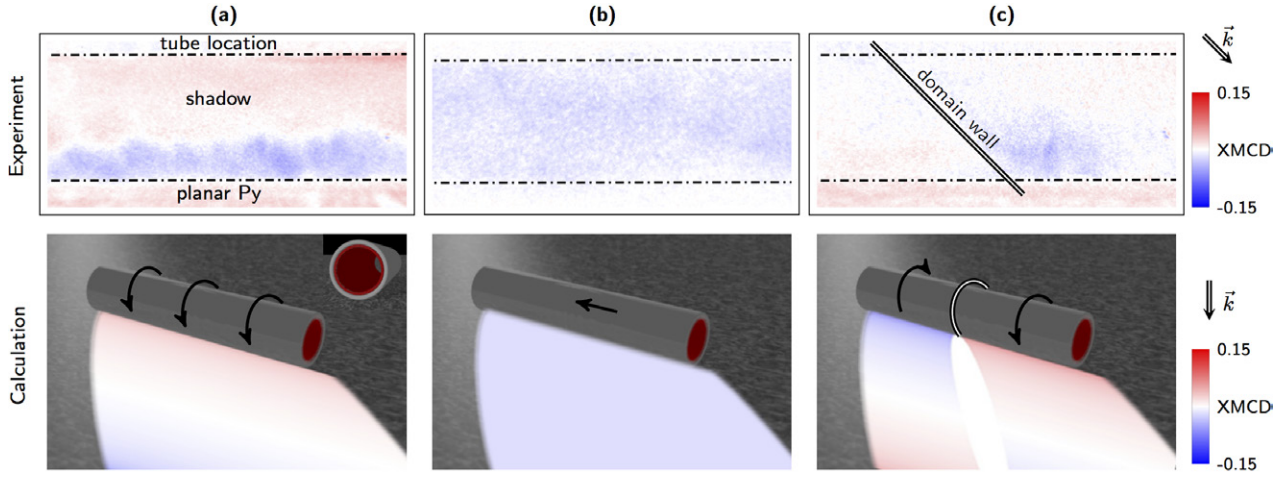

Figure 29. Comparison between experimental and simulated XMCD shadow contrast of (a) an azimuthally and (b) a longitudinally magnetized state within a magnetic tightly wound rolled-up nanomembrane with cylindrical shape. The orientation of the magnetic moments is indicated by arrows. X-ray beam hits the tube at a shallow angle of 16° and at 45° with respect to the symmetry axis. Dash-dotted lines enclose the shadow region of the tube with one winding. Panel (c) shows an azimuthal state with a 180° domain wall domain wall perpendicular to the symmetry axis (double line). Reprinted with permission from [103]. Copyright (2014) American Chemical Society.

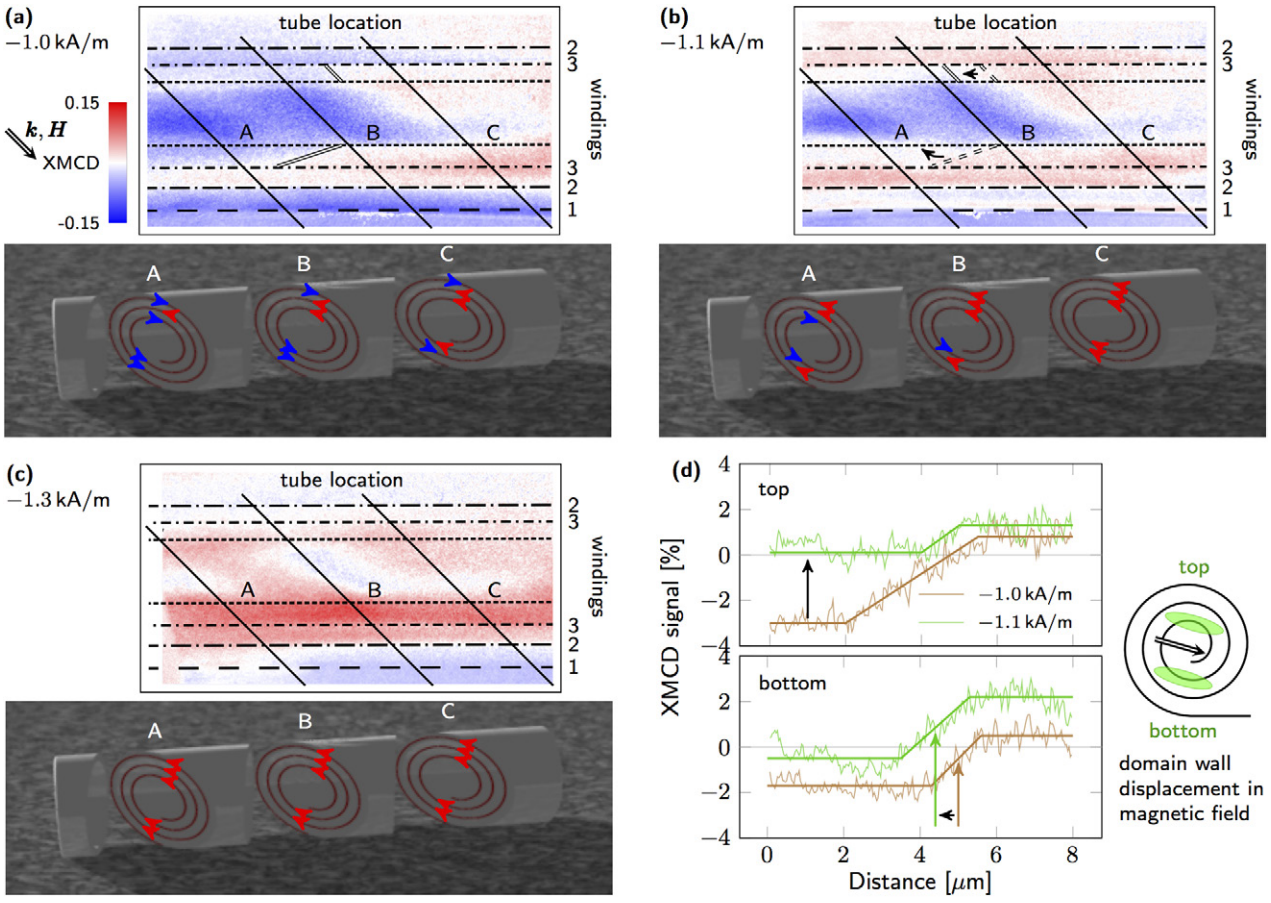

Figure 30. Layer-specific imaging of buried 3D magnetic rolled-up nanomembranes with multiple windings using T-XPEEM. The distinction between signals of different windings is accomplished as the absorption at the edges of the windings is pronounced (indicated by dash-dotted lines). (a)–(c) Snap shots of the magnetization reversal process while applying an in-plane magnetic field at 45° with respect to the symmetry axis after initially saturating at 2.4 kA m^{-1}. The planar magnetic film switches already at −0.2 kA m^{-1}. The magnetization at each winding can be reconstructed from the XMCD shadow contrast as shown for different line profiles (A, B, C) and reassembled along the symmetry axis. (d) Line profiles along the tube, i.e. of winding 3, provide insight into the magnetic field-driven evolution, including the distinction between domain wall displacement along or perpendicular to the symmetry axis (indicated by black arrow). Reprinted with permission from [103]. Copyright (2014) American Chemical Society.

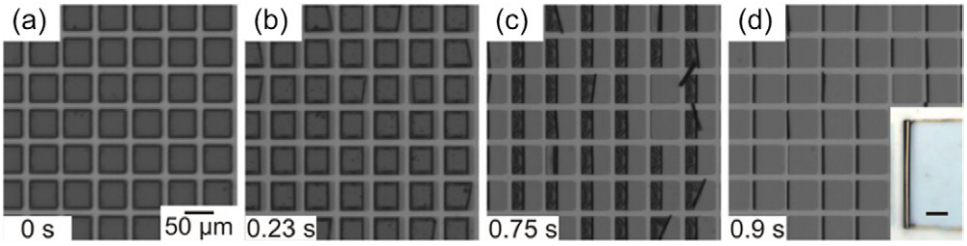

Figure 31. Temporal evolution of the rolling up process of magnetic films into tubes. Sequence recorded with a high-speed camera for an array of rolled-up (50 × 50) μm^2 square features of Pd/$Fe_{20}Ni_{80}$/Pd, where an angled deposition was used to promote the unidirectional rolling. Inset in (d) shows an image from a representative tube from the ensemble, with a diameter of 3 μm. The scale bar is 10 μm. Reprinted with permission from [97].

the edge of each winding allows for reconstructing more complex magnetization configurations within the 3D magnetic architectures. The dependence of the magnetization reversal on the local magnetization orientation (domains) emphasizes the importance of a non-destructive layer-specific imaging of individual windings. The magnetization orientation at each winding along the profile sections A, B and C are shown in the corresponding schematic 3D images (figure 30). Stacking multiple line profiles along the symmetry axis provides means to assess the magnetization configuration within the 3D object. The observation hints for a continuous domain pattern in the nanomembrane with oblique domain walls, thus appearing at different locations along the symmetry axis in each winding.

A more quantitative analysis of the magnetization including domain wall displacement during magnetization reversal is done by extracting the line profile of each winding along the symmetry axis, exemplarily shown for winding 3 in figure 30(d). The transition region marked by brown and green arrows for external magnetic fields of -1.0 and -1.1 kA m^{-1}, respectively, refer to the magnetic domain walls indicated by solid double lines. The dashed double lines represent for illustration the domain wall position at -1.0 kA m^{-1} (figure 30(b)). Analyzing the XMCD signal of the top and bottom part of winding 3 reveals a displacement perpendicular to and along the symmetry axis, respectively. Assuming a continuous pattern, such a change may be assigned to a combination of domain wall translation and rotation, which is likely to occur in soft-magnetic materials. Moreover, the similarity of the magnetic pattern in figures 30 and 29(c) suggests an azimuthal or slightly tilted magnetization in the inner winding, whose energetically unfavored domain decreases in size with increasing magnetic field by magnetization rotation and domain wall displacement.

5.2.4. Non-epitaxial strained layers. Alternative sacrificial layers, such as polymers (e.g. photoresist [39, 45, 97, 104]) or Ge [96, 101], have been introduced. The processing of the functional layer stack is as follows: First, patterns are defined on a substrate by photolithography. The materials of choice are deposited with conventional deposition techniques (electron beam vapor deposition, thermal evaporation, atomic layer deposition or sputtering). The angle of deposition can be adjusted from 0° to 90° in order to define a preferential rolling direction. Polymer sacrificial layer can be selectively removed with organic solvents (acetone, alcohols). Using polymers and acetone, almost any inorganic material or material combination including SiO/SiO_2, ZnO, Al_2O_3, TiO_2, Pt, Co, Permalloy/Pd, Ti/Fe/Pt, Co/Pt, Pd/Fe, Co/Au can be rolled-up into Swiss roll structures [90, 97]. The tube diameter can be tuned by changing layer thickness and strain gradient across the nanomembrane. Latter one strongly depends on the deposition parameters, e.g. deposition rate, deposition angle and substrate temperature.

There are numerous studies available on the realization and investigation of magnetic Swiss rolls relying on a photoresist [39, 45, 97, 104] or Ge-based [96, 101] sacrificial layers. Exemplarily, we describe the approach taken towards the fabrication of well-ordered ferromagnetic rolled-up tube structures facilitating photoresist as sacrificial layer in the roll-up process. The resist layers can be etched or dissolved with common organic solutions typically used in lift-off processes. In order to ensure deterministic rolling, the pattern size should be constrained in two lateral dimensions by patterning the resist underlayer. Then, the films are deposited at an angle with respect to the normal incidence of the material vapor flux. The corresponding lateral anisotropic strain defines the rolling direction that preferentially coincides with the deposition direction. In that case, the resist edge tilted towards and away from the material vapor flux will function as an anchor site and an etching window, respectively. Figure 31 shows a series of selected video microscopy images taken with a high-speed camera of the rolling sequence from a Pd(2 nm)/$Fe_{20}Ni_{80}$(8 nm)/Pd(2 nm) trilayer deposited at an angle of about 70° with respect to the normal incidence [97]. The images illustrate the roll-up process of an array with (50 × 50) μm^2 square features rolling together from right to left. In figure 31(d) the final result is a well ordered array of single rolled-up magnetic tubes. The inset in figure 31(d) shows an individual rolled-up tube from the ensemble, with a diameter of 3 μm.

The rolling process in thin solid films is determined by the built-in strain gradients across the layer thickness, and can represent either a roll-up or a roll-down process, depending on the sign and direction of the differential strain [97, 375]. Figure 32(a) shows an SEM image of a representative tube with a diameter of 4.6 μm, which rolled up from a circularly patterned Pd/$Fe_{20}Ni_{80}$/Pd trilayer system. As an inset, we show a schematic illustration of the roll-up process observed for this magnetic film system. The film was deposited at a

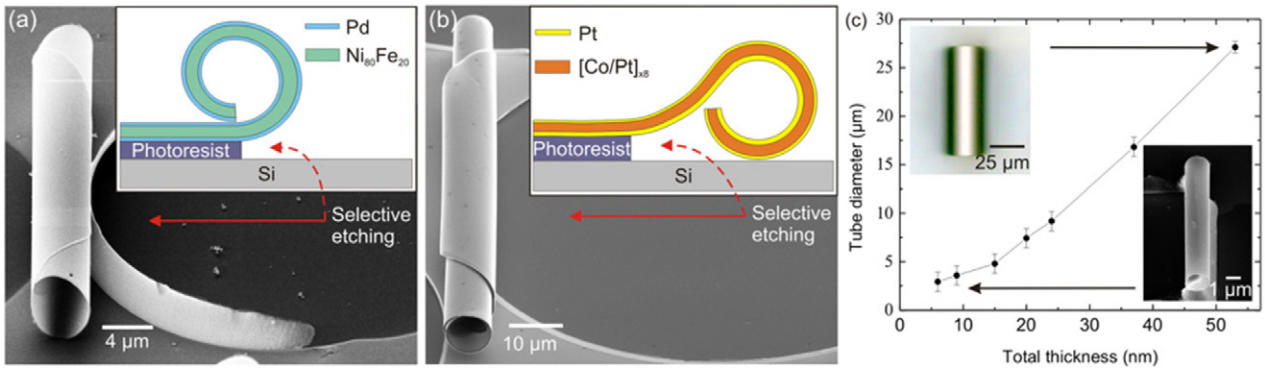

Figure 32. Roll-up and roll-down examples of ferromagnetic microtubes. (a) SEM image of a tube with a diameter of 4.6 μm rolled from a circularly patterned Pd/$Fe_{20}Ni_{80}$/Pd film. The inset illustrates the roll-up configuration. (b) SEM image of a tube consisting of Co/Pt with a diameter of 8.5 μm. The corresponding roll-down configuration is illustrated as an inset. (c) Scaling of tube diameter with total thickness for a series of Pd/$Fe_{20}Ni_{80}$/Pd samples. The top-left inset shows an optical microscopy image of a 25 μm diameter tube, while the bottom-right inset shows an SEM image of a tube with a diameter of 1.5 μm. Reprinted with permission from [97].

shallow angle in an electron beam evaporator and spontaneously rolled up towards the edge to which the deposition was directed when exposed to solvents. The other type of rolling (roll-down) is presented in figure 32(b). The inset illustrates the roll-down process observed for a Co/Pt multilayered system. For this type of film, we observed *in situ*, during the etching process under an optical microscope, that the film did not roll up but buckled upon solvent exposure, suggesting a preference to roll down. Due to the conformal coverage of the film at the edges of the resist, the buckled film remained pinned to the edges of the pattern.

Figure 32(c) plots the scalability of the tube diameter with the total layer thickness for the Pd/$Fe_{20}Ni_{80}$/Pd system. Note that figures 26(c) and 32(c) reveal a similar trend but at a different length scale. The insets correspond to optical and SEM images from representative tubes with the largest (top-left) and smallest (bottom-right) diameters obtained. The scaling allows for designing structures with deterministic dimensions, which can be tuned by substrate temperature, cooling rates and deposition fluxes. Proper choice of a sacrificial layer, e.g. water solvable Ge-based [40, 96, 101, 102, 376] or polymeric-based [45, 377, 378] layers, which is not affected during the standard optical lithography processing, makes it possible to realize magnetic rolled-up nanomembranes with integrated electrical contacts. This allows for instance to fabricate magnetic field sensor devices [39, 40, 45].

5.2.5. Self-assembled on-chip integrated giant magneto-impedance sensorics. The magnetic counterpart of conventional electro-encephalography [379], namely magneto-encephalography [43–45], relies on the detection of tiny magnetic fields generated by electrical currents in the nervous system. Being able to provide the same physiological information as conventional electro-encephalography, magneto-encephalography offers strong advantages in terms of sensitivity and the opportunity to identify diseases, e.g. epilepsy at early stages with superior spatial resolution [380]. Standard magneto-encephalography equipment is based on superconducting quantum interference devices (SQUID), which need permanent cooling with liquid helium and possess rather high fabrication and maintenance costs limiting their wide spread applicability. Development of cost-efficient yet high-performance and even portable magneto-encephalography equipment would bring these unique devices to regular medical institutions offering early stage disease diagnostics with great spatial resolution hence helping to minimize invasiveness upon surgical treatment.

Karnaushenko *et al* [45] realized arrays of on-chip integrated giant magnetoimpedance (GMI) sensors. The developed technology platform relies on novel photopatternable, thermally and chemically stable imide- and acrylic-based polymers, which allows for microelectronic processing including multiple fabrication steps, e.g. deposition and lithography. The key advantages offered by the self-assembly approach to fabricate arrays of high-performance GMI devices are twofold (figure 33) [45].

(i) A geometrical transformation from the initially planar layout into a tubular 3D architecture allows to achieve favorable azimuthal magnetic domain patterns without the need of rapid quenching of the magnetic layer stack in a magnetic field. A direct comparison with its planar counterpart reveals a GMI ratio that is almost two orders of magnitude larger. The tubular sensor reveals a maximum GMI of ≈90% at a magnetic field of 10 Oe and an excitation frequency of 75 MHz.

(ii) Integration of multiple functional elements in a single architecture including GMI sensors and pick-up coils, which are produced simultaneously in a single fabrication step. These compact GMI sensors equipped with pick-up coils operate at ambient condition and reveal a high sensitivity to small magnetic fields of 45 μV Oe^{-1}. The remarkably small excitation current of 1 mA is superior to state-of-the-art GMI devices.

It creates a solid foundation for future development of CMOS compatible arrays of gradiometers based on GMI sensorics needed for magneto-encephalography applications. Portable

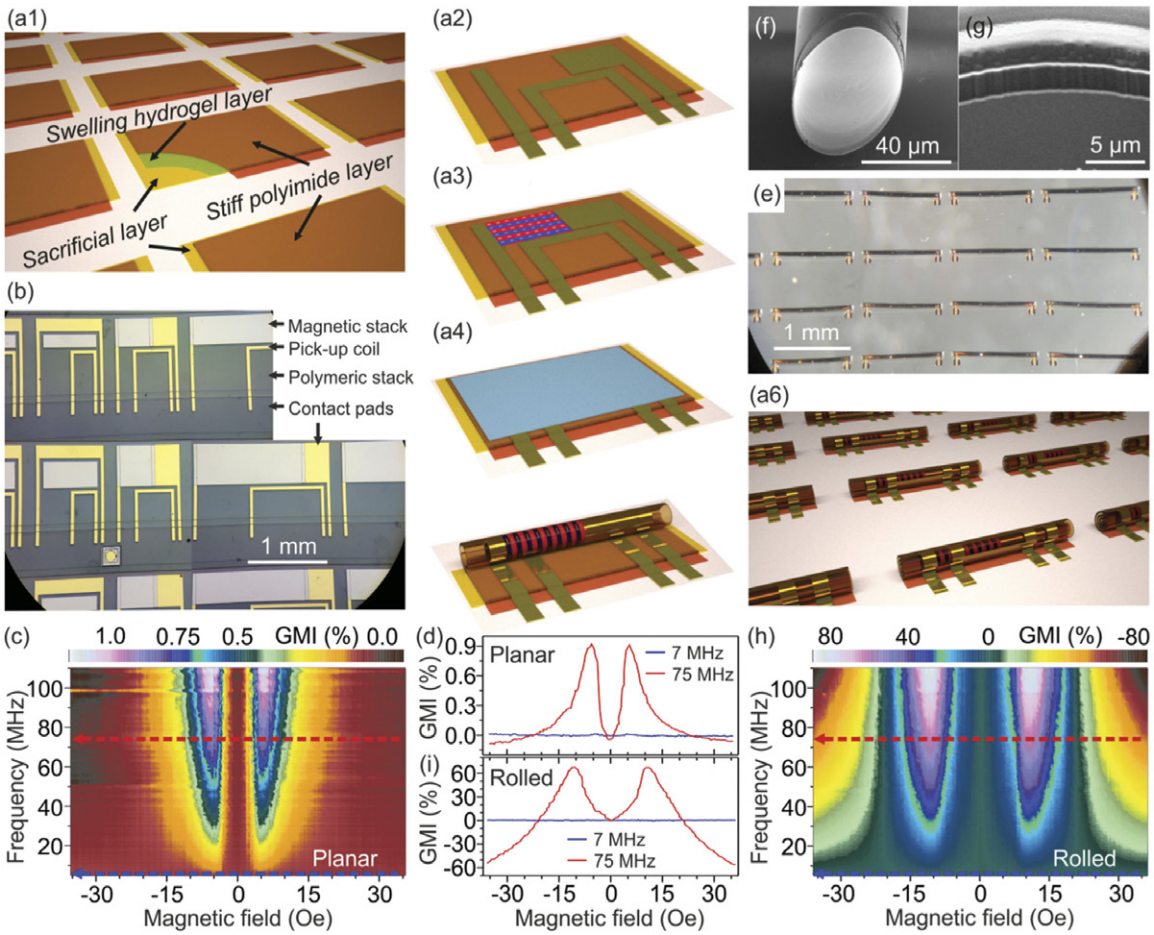

Figure 33. (a1) Patterned functional polymeric stack. (a2) Contacts and pick-up coil. (a3) Magnetic layer stack. (a4) Electrical insulation layer. (a5) Initiating the self-assembly. Fabrication and characterization of on-chip integrated GMI sensorics. (a) Schematics of the fabrication steps to realize arrays of tubular GMI sensor elements. Optical micrograph of an array of (b) planar and (e) self-assembled device. 3D map of the GMI response versus frequency and magnetic field measured of the (c) planar and (h) self-assembled device. Magnetic field dependences of the GMI response measured at 7 and 75 MHz of (d) planar and (i) self-assembled structure. (f) SEM image of the tube edge. (g) FIB cut through the tube revealing 2 windings firmly attached to each other without forming voids. Reprinted with permission from [45]. Copyright (2015) The Authors. Published by WILEY-VCH Verlag GmbH & Co.

light-weight magneto-encephalography devices bear great potential to revolutionize the field of smart prosthetics, brain-machine and brain-brain interfaces. This is because of its capability to precise volumetric localization and characterization of magnetic signals corresponding to particular mental activity not directly accessible by electro-encephalography and electro-corticography.

5.2.6. 3D compact giant magneto-resistive sensorics for microfluidics. Rolled-up nanotech enables the fabrication of multifunctional devices, which can be straightforwardly integrated into existing fluidic architectures [39]. We applied strain engineering to roll-up a functional nanomembrane consisting of a magnetic sensor element based on [Py/Cu] multilayers with giant magneto-resistance (GMR) response. The sensor's characteristics before and after the roll-up process are found to be similar, allowing for a reliable and predictable method to fabricate high quality ultra-compact GMR devices. The performance of the rolled-up magnetic sensor was optimized for high sensitivity to weak magnetic fields, as required in biomedical applications. We demonstrated that the rolled-up tube itself can be efficiently used as the fluidic channel guiding the magnetic objects to be detected, while the integrated magnetic sensor provides an important functionality to detect and to respond to a magnetic field. The performance of the rolled-up magnetic sensor for the in-flow detection of ferromagnetic CrO_2 nanoparticles embedded in a biocompatible polymeric hydrogel shell was highlighted.

6. Magnetic helices

The effect of topology plays an important role in the electromagnetic properties of architectures that have complex magnetic configurations. These complex systems include helimagnetic materials which are characterized by a gradual tilting of adjacent spins. Rather than depending on nature to produce such structures, there is another approach which relies on a continuous distribution of the magnetic moment through intelligent design, realized by micro-/nanofabrication techniques.

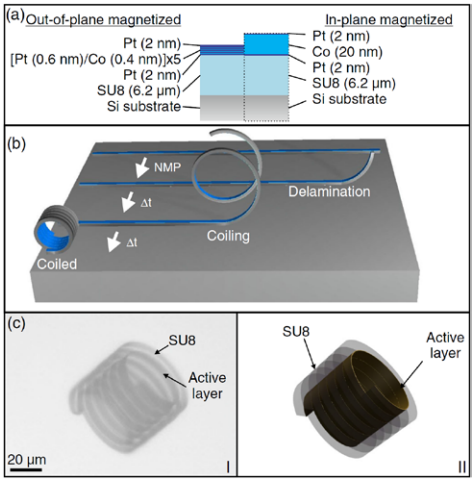

Figure 34. Makeup and assembly of differently magnetized hybrid coils. (a) Composition of the different layer stacks for a hard out-of-plane or in-plane magnetized active layer. (b) Self-assembled coiling process: A photolithographic step defines the SU8 pattern. The active layer is deposited on top of this. The SU8 is delaminated from the substrate in N-methyl-2-pyrrolidone, causing the gradient strain between the SU8 and active layer to lead to a roll-up. (c) An optical image (i) and artist rendition (ii) of a hybrid helix coil with an SU8 organic outer layer and an inorganic magnetic (active) inner layer. Reprinted with permission from [15]. Copyright (2011) by the American Physical Society.

6.1. Magnetic microhelix coils

Delaminating polymer stripes with an 'active' magnetic nanomembrane deposited on top provides means to create architectures (figure 34) that exhibit one of the three unique magnetic configurations: hollow-bar, corkscrew and radial magnetization (figures 35(a)–(c)) [15]. This approach is based on the self-assembly of strained polymeric structures [89] which delaminate from the host substrate to form microhelix coils [98]. For this purpose, a thick photosensitive polymer ($(2 \sim 10)\ \mu$m), SU-8, is spin-coated onto a cleaned Si substrate. Narrow stripes ($1\ \text{mm} \times 7\ \mu$m) are then defined by photolithography. The magnetic layer is sputtered onto the polymer, possessing either an in-plane (20 nm Co) or an out-of-plane ($[\text{Co}(0.4\,\text{nm})/\text{Pt}(0.6\,\text{nm})]_N$) easy axis magnetization. Next, the samples are placed into the delamination medium, e.g. N-Methyl-2-pyrrolidone (NMP), at an initial time t_i. The polymer absorbs the NMP, causing it to swell, which in turn, increases the differential strain in the structure. At a certain point, the strain becomes sufficiently large to delaminate the structure and to relax via curling up [87]. This curl-up turns into a full coil-up, as the structure completely delaminates from the substrate, forming compact microhelix structures at a final time t_f (figure 34). Using a 6.2 μm-thick SU-8 layer results in helices with a length of 50 μm and a radius of 35 μm.

Depending on the magnetization orientation of the magnetic stripe prior to rolling, hollow-bar (figure 35(a)), corkscrew (figure 35(b)) and radially (figure 35(c)) magnetized coils can be created. The latter two configurations are particularly interesting as they resemble a microscale helimagnet-like orientation and a radial magnetization that are not obtainable by other means. The uncompensated magneitzation of the microhelix coils leads for different magnetization configurations to distinct rotating motions when exposed to an oscillating magnetic field. The magnetic moment of the hollow-bar-magnetized coils points along the axis of the coils which triggers an end-over-end tumbling motion through the medium (figure 35(d)). The corkscrew-magnetized coil has a magnetic moment that spirals itself along the length of the structure resulting in a forward dancing motion (figure 35(e)). In contrast, the radially magnetized structure responds with a directionally-deterministic forward rotation (figure 35(f)) due to uncompensated magnetic moments pointing inwards [99, 381].

6.2. GLAD approach to realize helices at the nanoscale

Strain engineering allows to produce helices with dimensions in the range of some micrometers. Recently, glancing angle deposition (GLAD) or shadow deposition approach [17, 82, 83] emerged as a convenient tool to fabricate magnetic helical objects with ultimately small dimensions reaching a length of 50 nm and helix pitch of 25 nm (figure 36(a)) [86]. This method provides arrays of nanoobjects if the substrate is seeded with nanoparticles, which restrict the growth of the material. The size and periodicity of the seed nanoparticle determine the final morphology of the helix. Nanoscale objects in GLAD are obtained fabricating seeds with electron beam lithography [382] or using self-assembled arrays of nanoparticles realized, e.g. via block copolymer micelle lithography [17, 86]. The latter method paves the way towards wafer-scale processing.

Gibbs *et al* [86] reported the magnetic response of Ni and Co helix arrays with various pitch sizes (figure 36(a)). The hysteresis loop taken at room temperature with a SQUID is exemplarily shown for Co helices (180 nm long with a pitch of 90 nm) in figure 36(b). The saturation magnetization is estimated to be 630 kA m^{-1} which is considerably (about half) lower than that of bulk Co. The specific shape of the loop might indicate the alignment of the magnetic moment along the helix-shaped object. This assumption has recently been proven by Phatak *et al* [77] visualizing the magnetic induction in 3D Co helices with aberration-corrected Lorentz transmission electron microscopy (figure 41).

7. Tomographic imaging

Conventional visualization techniques, such as microscopy, record a 2D projection of a 3D attenuation field associated with the spatial distribution of atomic mass densities or electromagnetic fields. Depending on the experimental setup working either in reflection or transmission mode, information about outermost surfaces or thickness-integrated bulk regions are obtained, respectively. In order to retrieve the 3D information from a set of 2D projections, tomographic reconstruction algorithms have been developed [383] and applied to various classes of materials.

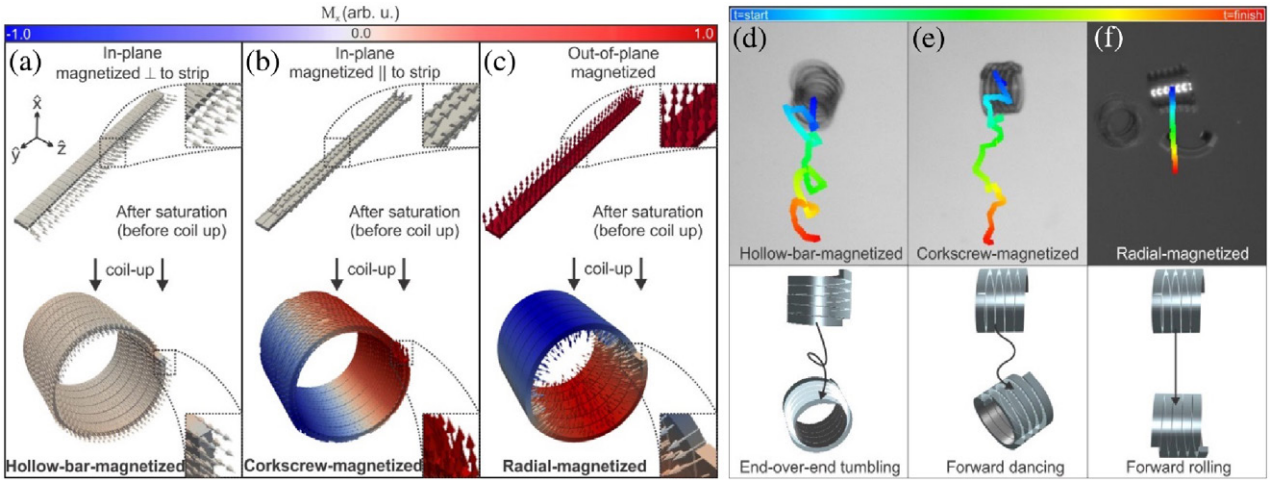

Figure 35. Creation of three unique magnetic configurations by coiling up magnetic stripes with either in-plane or out-of-plane magnetic easy axis: (a) hollow-bar-magnetized configuration, (b) corkscrew-magnetized coil, (c) radially magnetized coil. (d)–(f) Magnetic configuration probed by lateral propagation of coils in an alternating magnetic field. (d) Hollowbar-magnetized coils respond in an end-over-end tumbling motion. (e) Corkscrew-magnetized coils respond in forward dancing motion through the liquid. (f) Radial-magnetized coils roll directionally, deterministic forward. Reprinted with permission from [15]. Copyright (2011) by the American Physical Society.

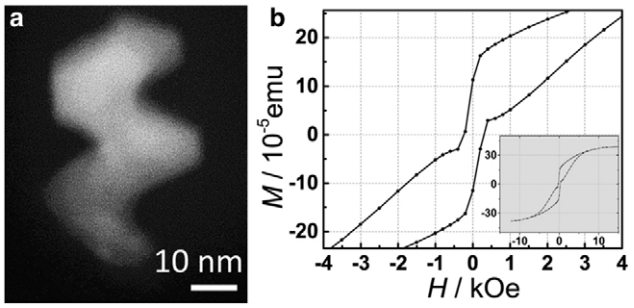

Figure 36. Magnetic nanohelices. (a) High-angle annular dark-field scanning transmission electron microscopy image of a Ni nanohelix with a length of about 50 nm. (b) Magnetic hysteresis loop of Co nanohelices (180 nm long with a pitch of 90 nm). Reproduced from [86] with permission of The Royal Society of Chemistry.

7.1. Radon transformation

The first work on the mathematical background of tomographic imaging traces back to Radon [384], who derived the reconstruction formula for a localized 2D function $\mu(x, y)$ whose integral values along certain directions are known. In particular, the integral value can be considered as the transmitted intensity:

$$I = I_0 \exp\left[-\int_{\mathcal{C}} \mu(x, y)\, \mathrm{d}r\right], \tag{11}$$

with the initial intensity I_0, the localized absorption coefficient $\mu(x, y)$, the integration path $\mathcal{C}$ parameterized by $r = -x \sin\alpha + y \cos\alpha$ with the projection angle α. The projection axis $s = -x \cos\alpha - y \sin\alpha$ is orthogonal to r (figure 37(a)). The Radon transform $\mathcal{R}(s, \alpha)$ (figure 37(b)) is obtained after rewriting (11) as:

$$\mathcal{R}(s, \alpha) = \ln\left(\frac{I}{I_0}\right) = \int_{\mathcal{C}} \mu(-s \sin\alpha - r \cos\alpha, s \cos\alpha - r \sin\alpha)\, \mathrm{d}r. \tag{12}$$

Its invariance under translation and rotation allows to perform Fourier transformations and to reconstruct μ from a set of projections using the Fourier slice theorem. Accordingly, calculating the 1D Fourier transform of $\mathcal{R}$ with respect to s $FT_1[\mathcal{R}(s, \alpha)] = \tilde{\mathcal{R}}(S, \alpha)$, with the reciprocal space vector component S, and performing the 2D inverse Fourier transformation $(FT_2)^{-1}$ leads to the spatial distribution of the absorption coefficient μ [384]:

$$\left.\begin{aligned}\mu(x, y) &= (FT_2)^{-1}\{FT_1[\mathcal{R}(s, \alpha)]\} = (FT_2)^{-1}[\tilde{\mathcal{R}}(S, \alpha)] \\ &\simeq \int_0^{\pi} \mathrm{d}\alpha \int_{\mathbb{R}} \mathrm{d}S \cdot \tilde{\mathcal{R}}(S, \alpha) H(S) \exp[2\pi \mathrm{i} S(-x \sin\alpha + y \cos\alpha)].\end{aligned}\right\} \tag{13}$$

The filter $H(S) = |S|\left[\Theta\left(S + \frac{1}{2\Delta s}\right) - \Theta\left(S - \frac{1}{2\Delta s}\right)\right]$, with the Heaviside function Θ, the pixel size of the screen Δs and the Nyquist frequency $\frac{1}{2\Delta s}$ [385], ensures a defined integral. The filtered backprojection (13) is basis for almost all tomography reconstruction algorithms.

Alternatively, the inverse Radon transform can be considered as a system of linear equations [383] similarly to the Radon transform (11) itself, since each trajectory r passes through a small fraction of space. Applying simultaneous algebraic reconstruction techniques, such as the Kaczmarz' method [386], allows to directly reconstruct $\mu(x, y)$ without applying the Fourier slice theorem (figure 37(c)). The avoidance of Fourier transformations provides means to reconstruct $\mu(x, y)$ from few projections (figures 37(d) and (e)), to increase the spatial resolution or to address each Radon transform individually. The latter aspect is crucial to treat vector fields, such as the magnetization.

Meanwhile, tomographic imaging has become a powerful technique that reveals internal structures in complex organic [122–124, 387–388] and inorganic [76, 77, 105, 106, 108–110, 119–121] objects by exploiting high penetrability and short wavelengths (high spatial resolution) of various

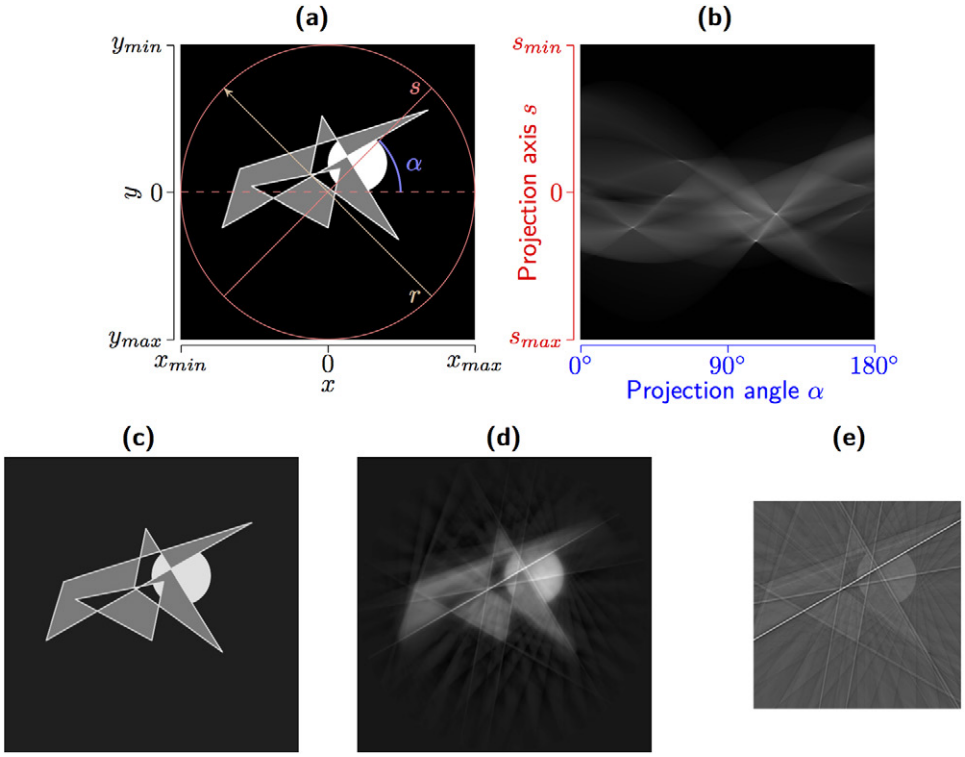

Figure 37. Schematics of Radon transformation and back projection in 2D. (a) Original image with indicated projection angle α and projection axis s. (b) Radon transform of (a). Direct iterative reconstruction with rotation step sizes (c) $\delta = 0.1°$ and (d) $\delta = 10°$. (e) Reconstruction with filtered back projection (FBP) and $\delta = 10°$. Reprinted with permission from [291].

kinds of radiation sources, including electron, neutron and x-rays. Among others, conditions during formation of minerals [119] and ceramics [121] as well as functioning and interplay of biological cells at subcellular level [122, 387] have been identified. Magnetic objects with macroscopic and nanoscopic expansions have been investigated using magnetic neutron tomography [105, 106] and electron-based techniques, including electron holography [76, 77, 107, 108, 388] and vector field electron tomography [109, 110], respectively.

7.2. Magnetic neutron tomography

The capability to characterize 3D spatial distributions of magnetic domains has been demonstrated by magnetic neutron tomography [105, 106] with a spatial resolution of ≈100 μm (figure 38). Neutron tomography relies on the detection of the phase shift, namely intensity difference, due to local variations in the refractive index originating from domain walls aligned parallel to the neutron propagation direction [389]. In particular, the refractive index with the spin-dependent term $\varphi = \pm\frac{1}{2}\mu_n B/E_n$ (magnetic moment of the neutron μ_n, and neutron kinetic energy E_n) [106] causes a distinct momentum transfer for parallel and anti-parallel neutron spin orientations with respect to the magnetic induction B. Hence, neutrons penetrating the media close to a domain wall experience a phase shift that is not compensated by subtracting intensities recorded for neutron beams with parallel and antiparallel spin orientation. The 3D spatial distribution of the domain walls is obtained from a set of projections (figure 38) via direct iterative reconstruction without applying the Fourier slice theorem [390] analogously to [386]. The treatment of individual projections provides the basis for capturing the angle-dependent phase shift contributions. Accordingly, an evaluation of the domain morphology can be given by identifying regions with dark contrast as volume domains.

The weak interaction between neutrons and induction B requires an accumulation of the phase shift over ≈100 μm. Thus, domain walls smaller than 100 μm or tilted against the neutron propagation direction cannot be resolved. On the other hand, an absorption coefficient of $\mu \approx 10^{-3}$ μm^{-1} (three orders smaller than those of x-rays) for transition metals and fast neutrons (2 MeV) allows to investigate bulky materials, e.g. single crystals, alloys and their modifications due to encapsulation or degradation relevant for industry. Constant phase shift and unaffected trajectory of neutrons when exposed to an homogeneous magnetic field provide further means to study magnetization reversal processes based on the evolution of the volume domain walls as no information about the magnetization itself or surface domains are accessible.

7.3. Electron-based 3D imaging

First successful attempts to access magnetic properties in 3D space with nanometer resolution have been accomplished in

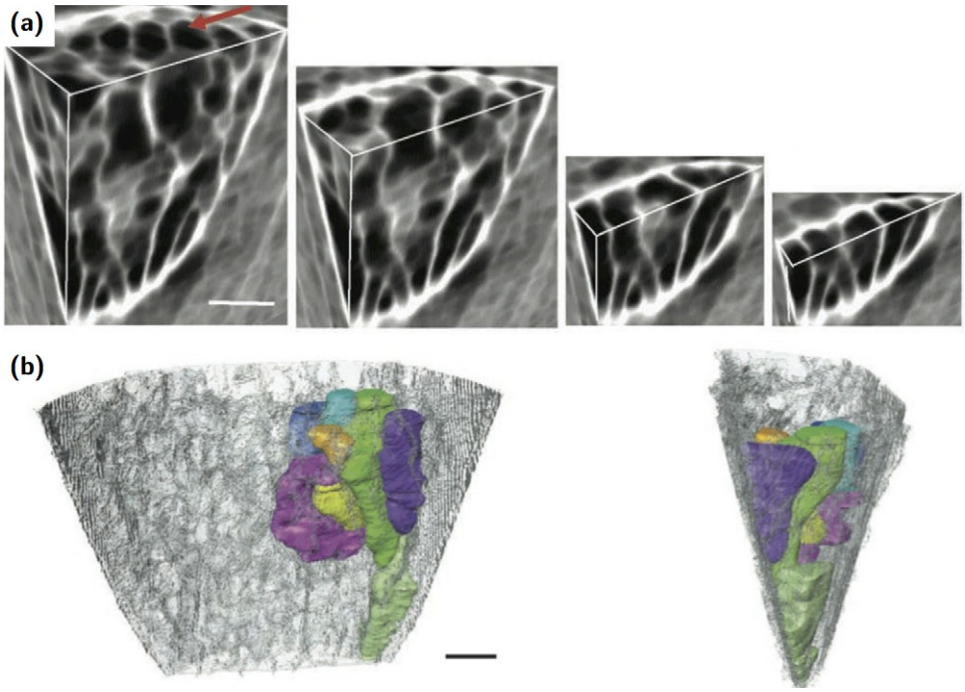

Figure 38. (a) Magnetic neutron tomography of a macroscopic FeSi wedge reveals the 3D spatial distribution of magnetic domain walls (bright) with a spatial resolution of about 100 μm. Subfigures show the very same region with a different top slice to visualize bulk regions. (b) Reconstructed domain distribution. Each color refers to a different domain. Information about surface domains and the magnetization itself cannot be retrieved with this approach. The scale bar is 1 mm. Reprinted by permission from Macmillan Publishers Ltd: Nature Communications [106], copyright (2010).

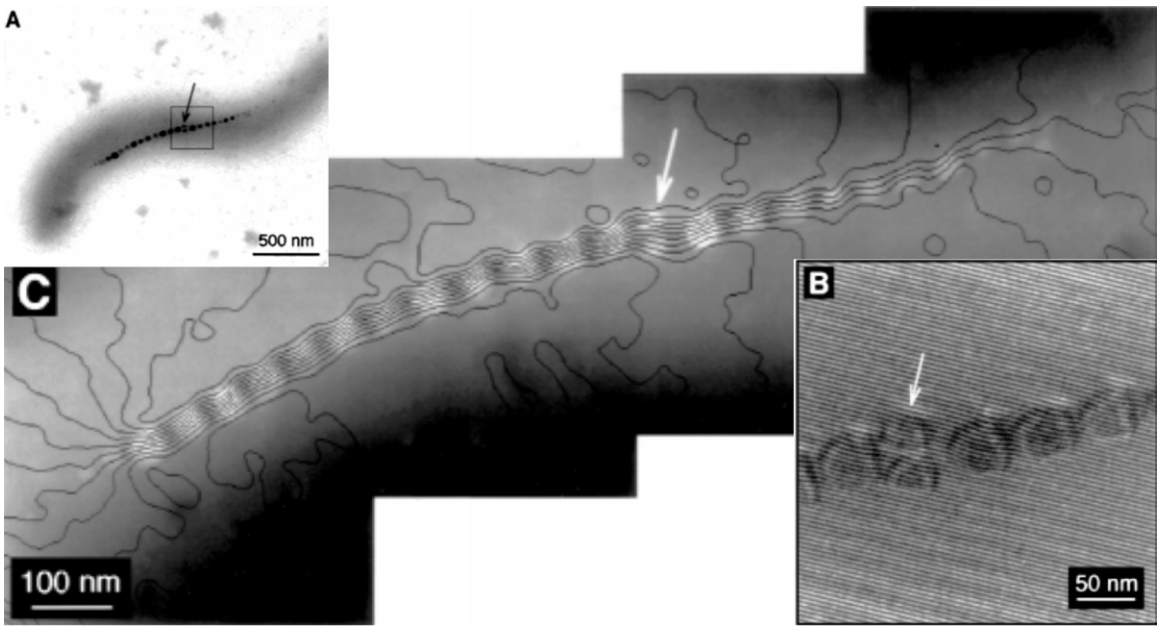

Figure 39. Electron holography of the magnetic induction of a chain of superparamagnetic nanoparticles in magnetotactic bacteria. (a) Transmission micrograph to identify strongly absorbing metal regions. (b) Recorded phase shift due to interaction with magnetic induction. (c) Reconstructed thickness-integrated field lines of the magnetic induction reveal magnetization vectors aligned along the chain. From [107]. Reprinted with permission from AAAS.

uniformly magnetized nanoparticles [108, 388], magnetotactic bacteria (figure 39) [107, 388] and nanorods/nanohelices (figure 40) [76, 77] with spatial expansions <100 nm by phase shift reconstruction with electron holography [391, 392] or Lorentz electron microscopy (LTEM) and employing the transport-of-intensity equation (TIE) [393, 394]. More recently, the capability of vector field electron tomography (VFET) [395, 396] was demonstrated by reconstructing magnetic vortex cores in soft-magnetic disks [109, 110].

7.3.1. Phase shift reconstruction. These approaches are based on the knowledge of the electron's phase shift traveling through

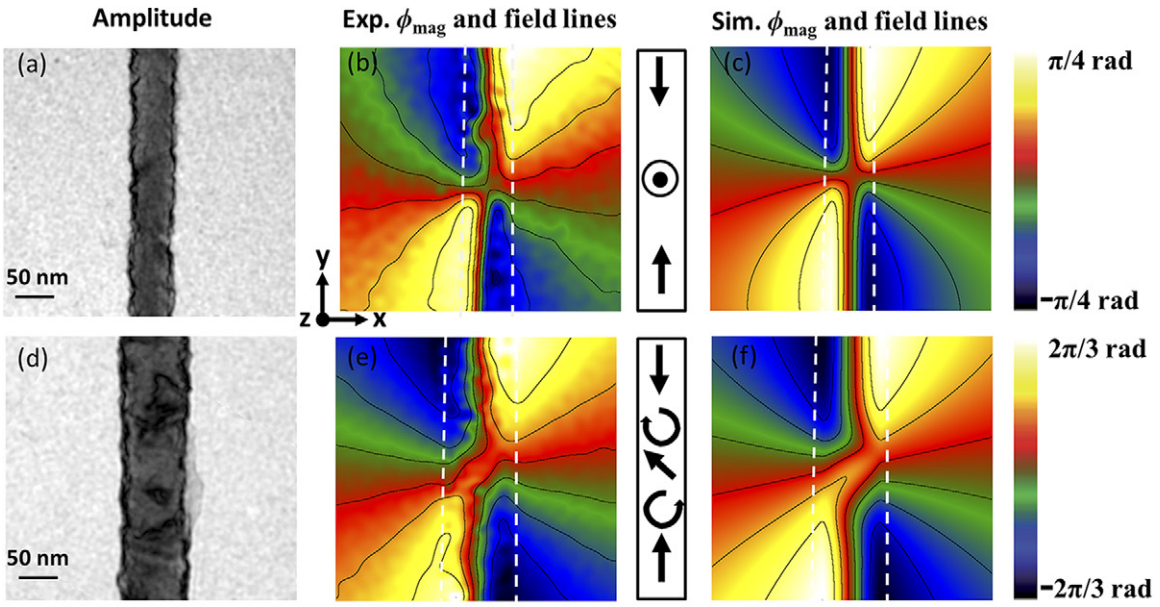

Figure 40. Magnetization configuration in soft-magnetic nanorods derived from phase shift images with electron holography. Panels (a)–(c) show transmission electron micrograph of a nanorod with $\varnothing \approx 50$ nm and corresponding experimental and simulated phase shift images, respectively, revealing a transverse domain wall. (d)–(f) Larger dimensions favor complicated spin textures like vortices. Reprinted with permission from [76]. Copyright (2013) American Chemical Society.

a 3D space with an electrostatic potential $V(\boldsymbol{r})$ and a magnetic vector potential $\boldsymbol{A}(\boldsymbol{r})$ [397]:

$$\left.\begin{aligned}\varphi(\boldsymbol{r}_\perp) &= \varphi_e(\boldsymbol{r}_\perp) + \varphi_m(\boldsymbol{r}_\perp)\\ &= C_e\bar{\varphi}_e(\boldsymbol{r}_\perp) + C_m\bar{\varphi}_m(\boldsymbol{r}_\perp)\\ &= C_e\int_{\mathcal{C}} V(\boldsymbol{r}_\perp + l\boldsymbol{\omega})\,\mathrm{d}l - C_m\int_{\mathcal{C}} \boldsymbol{\omega}\cdot\boldsymbol{A}(\boldsymbol{r}_\perp + l\boldsymbol{\omega})\,\mathrm{d}l.\end{aligned}\right\} \tag{14}$$

Similarly to the original formula (12), the thickness-integrated information (14) constitutes line integrals along the trajectory $\mathcal{C}$, parameterized by l, in the direction of $\boldsymbol{\omega}$. In fact, $\bar{\varphi}_e(\boldsymbol{r}_\perp)$ is the representation of (12) in 3D. The 2D position vector $\boldsymbol{r}_\perp$ lies in the projection plane so that $\boldsymbol{\omega}\cdot\boldsymbol{r}_\perp = 0$. Further are $C_e = e\pi/\lambda E_e$ and $C_m = e/\hbar$, with the electron wave length λ and the electron kinetic energy E_e.

Accordingly, the phase shifts of coherent electron beams reflect the thickness-integrated interaction with a magnetic induction $\boldsymbol{B}_\perp = (\nabla\times\boldsymbol{A})_\perp$ perpendicular to the electron beam propagation direction. In particular, isophase lines coincide with the magnetic field lines/ magnetization components lying in the projection plane. Thus, phase shift reconstructions performed with projections taken at the same angle may only be applied by correlation with simulations (figure 40) to reveal simple magnetization textures as occurring in e.g. uniformly magnetized nanoparticles [108, 388], nanorods [76, 77] or assemblies of those [107, 388].

7.3.2. Electron holography. Examples of chains of superparamagnetic nanoparticles in magnetotactic bacteria and magnetic nanorods are given in figures 39 and 40, respectively, recorded with electron holography [391, 392] that visualizes the phase shift between reference beam $\psi_1 = \mathrm{e}^{\mathrm{i}\boldsymbol{k}_1\boldsymbol{r}}$ and probe beam $\psi_2 = \xi(\boldsymbol{r})\mathrm{e}^{\mathrm{i}\boldsymbol{k}_2\boldsymbol{r}+\mathrm{i}\varphi(\boldsymbol{r})}$ by coherent interference on the CCD screen using an electron biprism [398]. Both amplitude

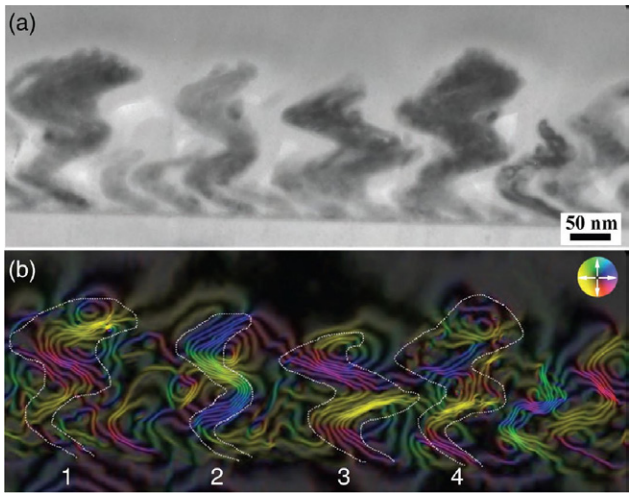

Figure 41. (a) In-focus image showing Co nanohelices. (b) Magnetization map obtained with LTEM using TIE formalism showing the direction of magnetization indicated by the colorwheel (inset). The magnetization map is overlaid with the cosine of phase shift (amplification factor of 3), which provides a visual indication of magnetic lines of induction. The dotted lines indicate the outline of the nanohelices. Reprinted with permission from [77]. Copyright (2014) American Chemical Society.

$\xi(\boldsymbol{r})$ and phase $\varphi(\boldsymbol{r})$ originating from interaction with electromagnetic fields of the sample are captured in the recorded intensity pattern according to:

$$\left.\begin{aligned}I(x) &= |\psi_1 + \psi_2|^2\\ &= 1 + \xi^2(\boldsymbol{r}) + \kappa\xi(\boldsymbol{r})\cos\left[(\boldsymbol{k}_1 - \boldsymbol{k}_2)\boldsymbol{r} - \varphi(\boldsymbol{r})\right].\end{aligned}\right\} \tag{15}$$

The contrast is reduced by the coefficient κ that takes into account temporal and spatial coherence of the electron beam.

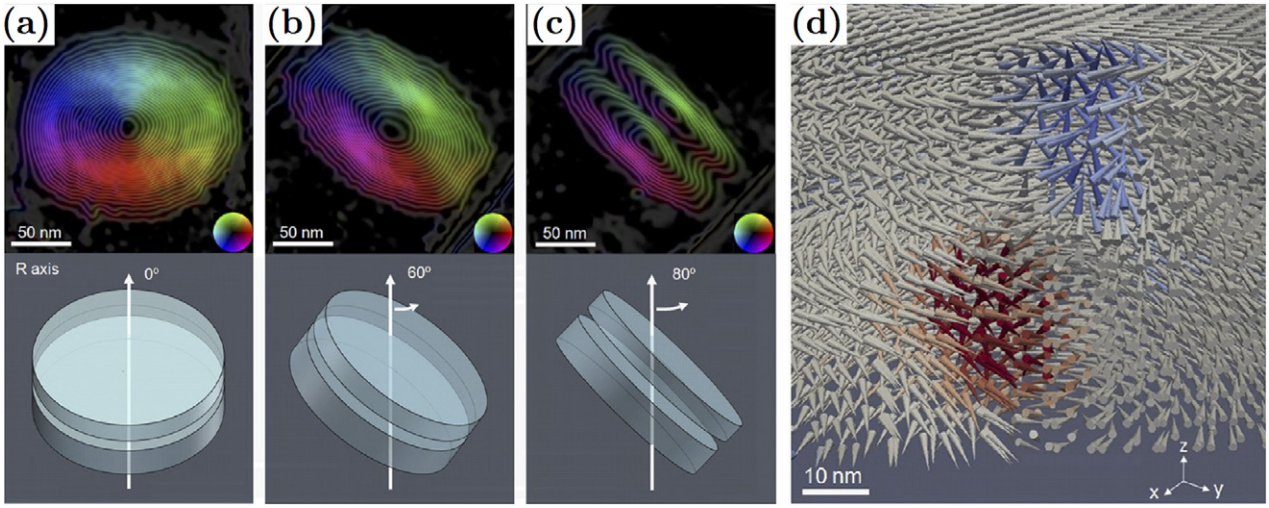

Figure 42. Vortex core interaction in vertically stacked soft-magnetic disks revealed by vector field electron tomography with transmission electron microscopy. (a)–(c) Acquiring phase shifts at various projection angles around at least two rotation axes allows to reconstruct the 3D spatial distribution of the magnetization at the nanoscale (d). Reprinted with permission from [110]. Copyright (2015) American Chemical Society.

7.3.3. Lorentz transmission electron microscopy utilizing the transport-of-intensity equation. In contrast, Lorentz microscopy with TIE omits the use of a reference beam by accumulating a through-focus series of images that reveals the thickness-integrated magnetic induction components perpendicular to the electron beam propagation direction according to $\nabla\varphi = C_m \boldsymbol{B}_\perp d$ with the sample thickness d [394]. Varying focus changes the size of the probing area and thus the amount of enclosed flux lines that is reflected by the gradient of the phase shift.

Figure 41(a) shows an in-focus TEM image of nanoscale helices prepared by GLAD [399] (see section 6.2 for further details). The diameter of the entire helix structure is 115 nm with the distance between the helices of 130 nm. The diameter of the Co wire, which forms the nanohelix, was measured to be 20 nm. The magnetization in the nanohelices were studied employing aberration-corrected Lorentz transmission electron microscopy (LTEM) [400] by obtaining maps of the local magnetic induction in and around the nanohelices using through-focus series of LTEM images prior to high resolution imaging. Employing the TIE formalism [394], the magnetic phase shift of the sample was retrieved; The gradient of the phase shift was calculated in order to obtain the thickness-integrated magnetic induction [401]. The color-coded magnetic induction map is shown in figure 41(b). The magnetic flux lines in- and outside the nanohelix correspond to the magnetization and the stray field perpendicular to the electron trajectory, respectively [77].

7.3.4. Vector field electron tomography. The loss of local information about the phase shift can be avoided by acquiring projections at different angles while rotating/ tilting the sample around at least two axes. Calculating the 1D Fourier transform of $\bar{\varphi}_e(\boldsymbol{r}_\perp)$ and $\bar{\varphi}_m(\boldsymbol{r}_\perp)$ with respect to reciprocal space vector $\boldsymbol{S}$ and applying the Fourier slice theorem (13) with the 1D Fourier transformation FT_1 and the inverse 2D Fourier transformation $(FT_2)^{-1}$, one obtains the mathematical basis of VFET [396]:

$$V(\boldsymbol{r}) = (FT_2)^{-1}\{FT_1[\bar{\varphi}_e(\boldsymbol{r}_\perp)]\} = (FT_2)^{-1}[\tilde{\varphi}_e(S_y, \alpha)], \tag{16}$$

$$B_x(\boldsymbol{r}) = (FT_2)^{-1}\{iS_y \cdot FT_1[\bar{\varphi}_m(\boldsymbol{r}_\perp)]\} = (FT_2)^{-1}[iS_y \cdot \tilde{\varphi}_m(S_y, \alpha)], \tag{17}$$

$$B_y(\boldsymbol{r}) = (FT_2)^{-1}\{iS_x \cdot FT_1[\bar{\varphi}_m(\boldsymbol{r}_\perp)]\} = (FT_2)^{-1}[iS_x \cdot \tilde{\varphi}_m(S_y, \alpha)]. \tag{18}$$

Equations (16) and (17) describe the angular dependence for rotations around the x-axis, while (18) considers rotations around y. The phase shift is accumulated along the trajectory $\mathcal{C}$ at the projection angle α. Note that α is determined by $\boldsymbol{r}_\perp$ in real space. Using the Maxwell equation $\nabla\boldsymbol{B} = 0$ allows to reconstruct the magnetic induction $\boldsymbol{B}$ from a set of projections around at least two rotation axes. Electrostatic contributions $\bar{\varphi}_e(\boldsymbol{r}_\perp)$ can be compensated by subtracting projections along opposite trajectories.

An experimental demonstration of the capability of VFET was very recently given by reconstructing the spin configuration in two vertically stacked planar soft-magnetic disks (figure 42) with a spatial resolution of few nanometers using a 1 MV holography electron microscope [110]. However, facilitating electrons as a probe is disadvantageous for in-field measurements on mesoscopic samples due to their electric charge and strong absorption coefficients, nor do they provide an element specificity. These highly demanded features can be offered by x-ray magnetic circular dichroism-based 3D imaging techniques.

7.4. Magnetic soft x-ray tomography

Contrary to magnetic neutron tomography and vector field electron tomography, magnetic x-ray tomography utilizing XMCD is directly sensitive to the magnetization [96]. As the XMCD signal contains information about the projection of the magnetization vector onto the x-ray beam propagation direction, nonuniform magnetization distributions in 3D magnetic

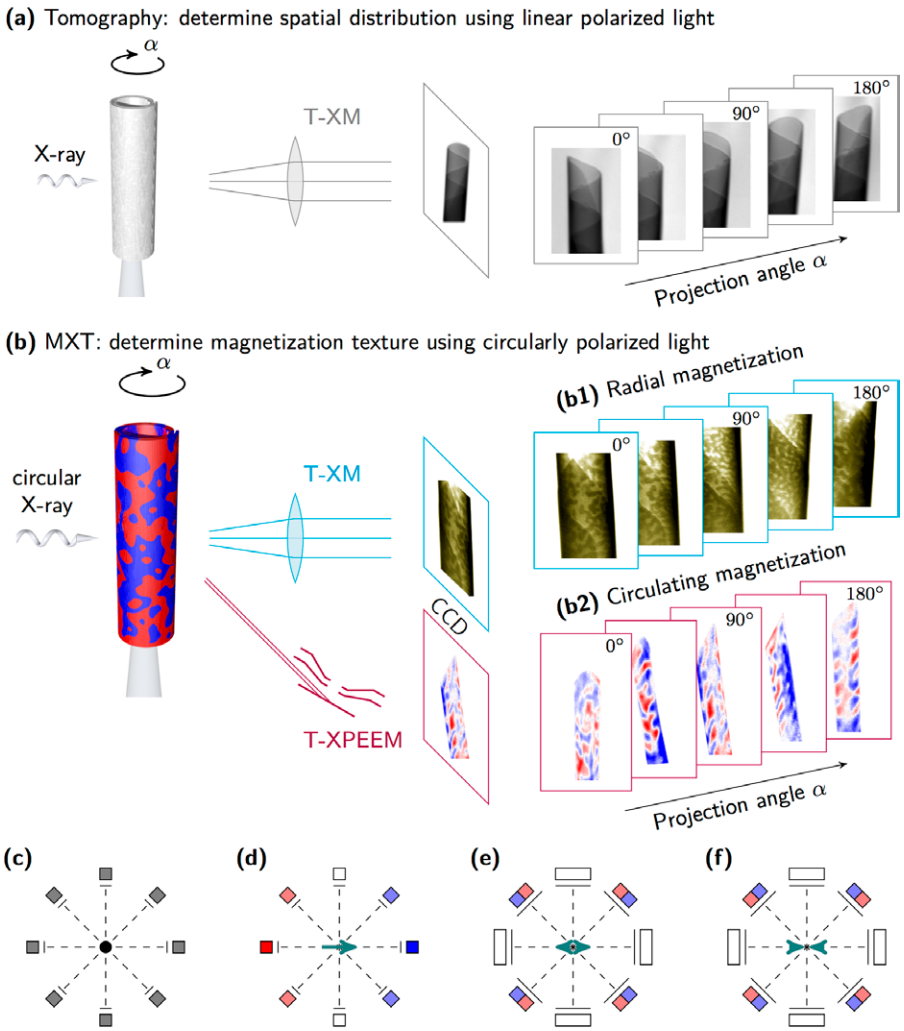

Figure 43. Comparison of the conceptual difference between (a) conventional scalar tomography and (b) magnetic x-ray tomography (MXT). (a) Light is attenuated when penetrating an object, e.g. tubular magnetic nanomembrane, according to its atomic mass distribution and angle-independently (c). The spatial distribution in 3D space is obtained from a set of 2D projections ranging from 0° to 180°. (b) Utilizing XMCD, the magnetization component along the beam propagation direction is visualized in (b1) radially and (b2) in-plane magnetized tubular architectures. (d) The XMCD signal shows an angular dependence that even reverses its sign for space-inverted x-ray propagation (red to blue, vice versa). White refers to a vanishing net XMCD signal. The corresponding underdetermined system of projections leads to an ambiguity of possible reconstruction when considering arrangements of two or more macrospins (e), (f) that may only be released by analyzing their evolution with varying projection angle. Reprinted with permission from [291].

objects cause a vector property induced non-additivity of the XMCD signal with complex ambiguous projections of the 3D magnetization (figure 43).

7.4.1. Algorithm. Mathematically, the contrast change with varying tilt angle describes the derivative of the magnetization with respect to the rotation angle. The approach proposed in [96] relies on solving systems of linear equations similar to those used for magnetic neutron tomography [106]. Using tubular architectures with well-defined magnetization orientations, e.g. radial or in-plane, provides means to consider 1D or 2D vector fields defined on the surface of the cylinder. In this respect, the determined magnetization component refers directly to the magnetization vector. Thus, data acquisition around one tilt axis coinciding with the symmetry axis of the tube is sufficient. However, valid restriction conditions, such as a spatial confinement of the magnetization vector field by locating the magnetic material using conventional scalar x-ray tomography and information on the preferential magnetization orientation, derived e.g. from the integral magnetic character, are needed. Note that a complete and consistent identification of the magnetization texture in extended samples with a rotation axis not coinciding with the local direction of the magnetization vector requires to record the XMCD contrast around several rotation axes. In contrast to vector field electron tomography, it is generally not sufficient to consider only two projection axes when dealing with nonuniform states due to a possible XMCD contrast compensation and locally varying saturation magnetization.

For contributions from front and back side (similar to section 4.1.3) described by $f(x)$ and $b(x)$ ($\propto \boldsymbol{M}\cdot\boldsymbol{k}$), respectively, the overall XMCD contrast at projection angle α_n and image position x perpendicularly to the rotation/ symmetry axis reads $I^{\alpha_n}(x) = f(x_n) + b(x_{-n})$ with $\alpha_n = \alpha_0 + n\delta$, $x_n = x + g\left(n\delta\frac{\varnothing}{2}\right)$

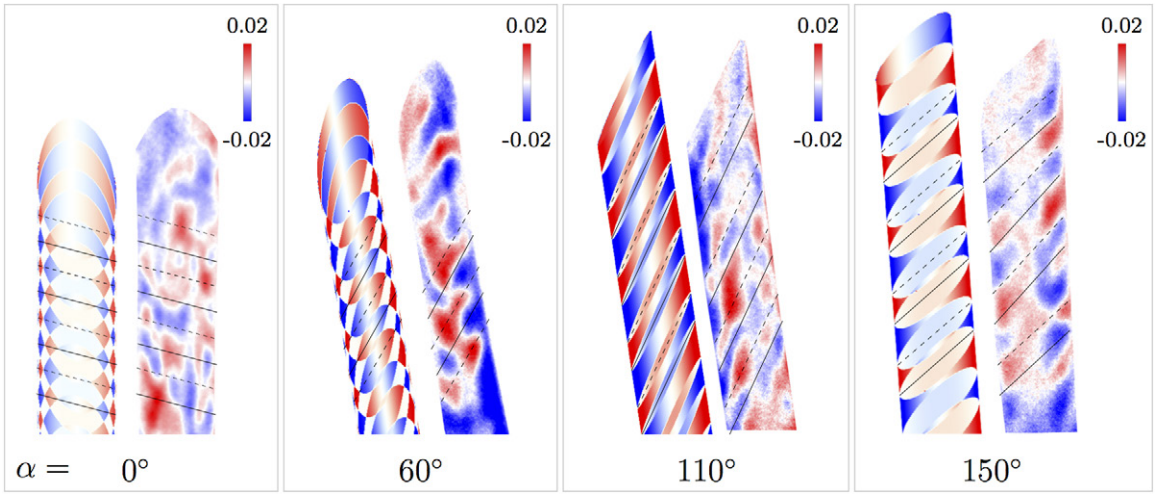

Figure 44. Correlation of experimental (right images) with simulated (left images) XMCD shadow contrast of azimuthal magnetization textures with alternating domain widths (0.9 μm & 1.2 μm (11% & 15%)) at different projection angles recorded with T-XPEEM. The projections reveal distinct and complex patterns that can only be assigned by simulation correlation to the corresponding magnetization textures. Solid lines serve as guide-to-the-eye. Reprinted with permission from [96]. Copyright (2015), Rights Managed by Nature Publishing Group.

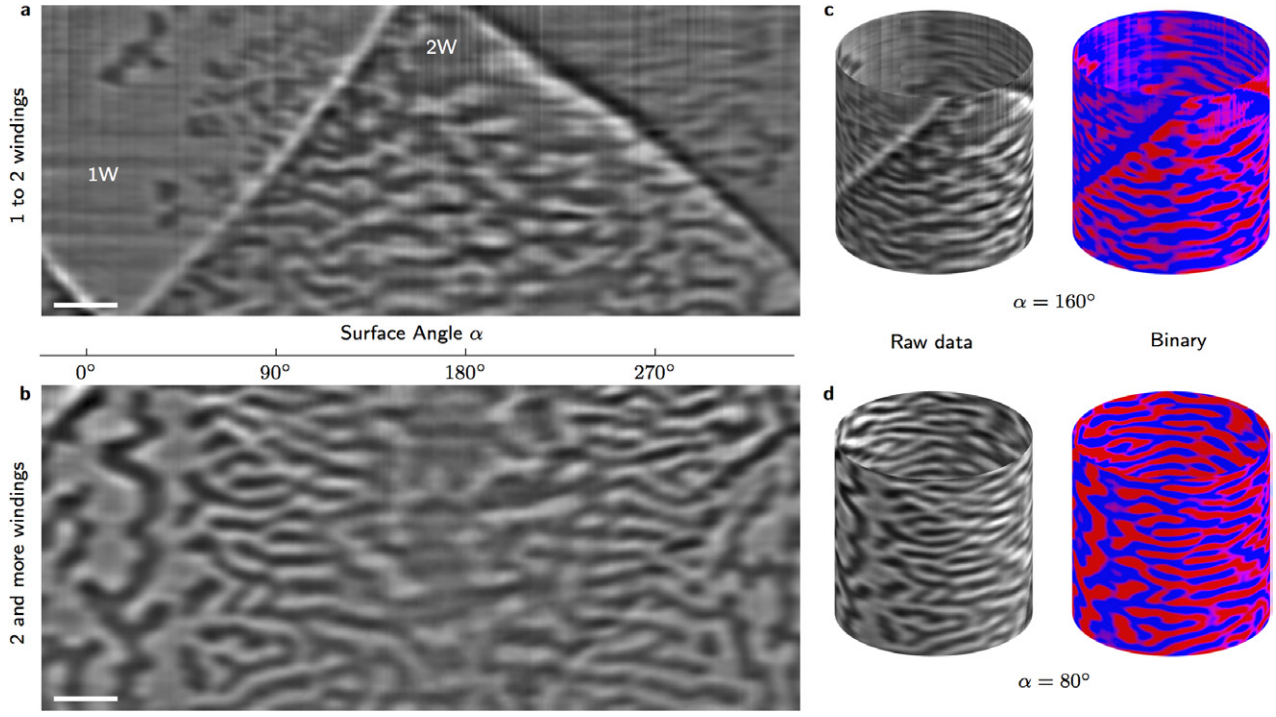

Figure 45. 3D reconstruction of a radial magnetization texture using MXT. (a), (b) Unrolled magnetic domain patterns for better visualization. 1W and 2W refer to regions with one and two overlapping windings, respectively. The transition from large isotropic to small azimuthal domains is obvious when approaching surfaces perpendicular to the direction of the initially applied magnetic field (180°). Dark contrast refers to strong absorption and a magnetization pointing outside the tube. (c), (d) 3D view of the magnetization in the thin films with cylindrical shape. In addition to the raw data (gray), the processed binary data with red and blue referring to radial magnetization vectors pointing outside and inside the tube, respectively, are shown. Reprinted with permission from [96]. Copyright (2015), Rights Managed by Nature Publishing Group.

and the rotation step size δ. The matrix transformation due to the curvature is taken into account by $g\left(n\delta\frac{\varnothing}{2}\right)$ with a lateral displacement at the very center of $\delta\frac{\varnothing}{2}$ perpendicularly to the symmetry axis. Thus, the XMCD contrast can be disentangled by integrating the difference between projections taken at α_0 and α_1 [96]:

$$\frac{1}{2\delta}\left[I^{\alpha_0}(x_0) - I^{\alpha_1}(x_{-1})\right] = \frac{1}{2\delta}\left[b(x_0) - b(x_0 - \delta\varnothing)\right] \approx \partial_x b^{(\alpha_0+\delta/2)}(x_0). \tag{19}$$

In this notation, $I^{\alpha_1}(x_{-1})$ is the XMCD contrast at $\alpha + \delta$ shifted by $g\left(-\delta\frac{\varnothing}{2}\right)$ perpendicularly to the symmetry axis to eliminate

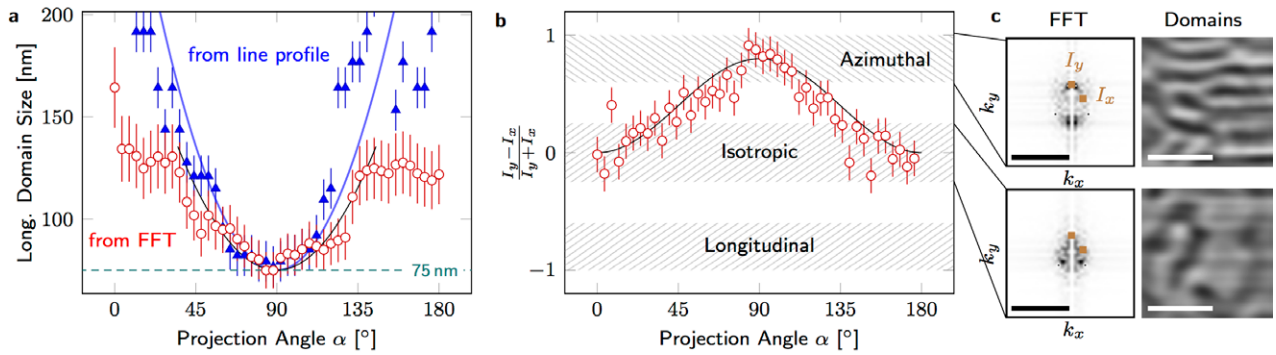

Figure 46. Angle dependence of the magnetic domain pattern. (a) Domain width in longitudinal direction reveals smallest values at $\alpha \approx 90°$. Data is extracted from line profiles of real space images and from peak positions of FFT images. (b) Continuous transition from an isotropic/ random domain configuration into an azimuthal ordering obtained from FFT. Solid lines serve as a guide-to-the-eye. (c) Corresponding FFT and real space images. Scale bars are $10\,\mathrm{nm}^{-1}$. Reprinted with permission from [96]. Copyright (2015), Rights Managed by Nature Publishing Group.

contributions from the front side. In case of a radially magnetized tube, the accordingly identified magnetization texture is unambiguously defined assuming a constant saturation magnetization. Spin textures with unknown magnetization orientation require to take projections around another rotation axis. In order to capture the magnetic domains in a correct way, the lateral shift $\delta\frac{\varnothing}{2}$ between two subsequent projections must not exceed the domain feature size. For instance, data recorded with rotation step sizes $\delta \approx 4°$ allows to reconstruct features as small as 40 nm at the surface with curvature radii of 1 μm (1 μm away from the rotation axis). Considering multiple projections and solving the corresponding system of linear equations further provides means to discriminate contributions from more than two surfaces [291].

7.4.2. Demonstration. Simple, deterministic magnetic domain patterns with e.g. straight magnetic domain walls as existent in circulating spin textures of tubular objects [96] may be identified by correlation with XMCD shadow contrast simulations. The projections shown in figure 44 for various angles reveal distinct features in both domain shape and contrast level and belong to an azimuthal domain pattern with periodically alternating domain width of (0.9 ± 0.2) μm and (1.2 ± 0.2) μm.

More complex spin textures, such as radially magnetized Co/Pd tubes, were identified by tomographic reconstruction using TXM (figure 45). The magnetization in areas with non-overlapping windings is saturated since the number of Co/Pd bilayers is optimized to ensure full remanence of the sample after magnetic saturation. The appearance of the multi domain state in the areas with two windings can be explained by an increased magnetostatic energy of the sample, which favors the multi domain state when doubling the number of Co/Pd repetitions [402]. Note that the uniaxial magnetic anisotropy of the sample is not expected to change due to the Ti spacer between each Co/Pd multilayer stack (winding). The magnetic states in figure 45 were obtained after the sample had been exposed to a magnetic field applied perpendicularly to the symmetry axis along $\alpha = 180°$ (perpendicular to the area with single winding). The morphology of the multi domain pattern is clearly changing with the angle featuring large isotropic domains with a size of more than 120 nm on the opposite side of the tube along the field direction and small domains with sizes down to 75 nm in surfaces perpendicular to the magnetic field (figures 45 and 46) [96]. This difference in morphology of the domain pattern is even more prominent in areas with two or more windings (figure 45, bottom row). Regions, which are perpendicular to the direction of the applied magnetic field, reveal narrow magnetic domains with lateral dimensions down to 75 nm along the symmetry axis and an elongation along the circumference of the tube (figure 45).

Reconstructing the magnetization configuration in tubular architectures with a spatial resolution of 40 nm is a first demonstration of the capabilities of MXT and a milestone towards establishing an x-ray based magnetization sensitive tomography for both qualitative and quantitative analysis of the magnetization vector field. MXT bears great potential to become a leading imaging technique to study 3D magnetic objects offering element specificity, inertia against electromagnetic waves and nanometer spatial resolution. Utilizing soft x-rays, samples with thicknesses up to 200 nm may be studied. This limitation originating from the strong resonant absorption of soft x-rays in metals can be lifted towards several micrometers facilitating hard x-rays with larger penetration depth and smaller absorption cross-section or off-resonance soft x-ray magnetic circular dichroism.

8. Conclusion and outlook

Recently, 3D curved magnetic objects, i.e. quasi-1D nanowires and 2D shells, have attracted much attention in both theoretical and experimental research due to striking properties [30, 31, 33, 34, 37, 38, 403] originating from curvature-induced contributions to the magnetic exchange energy [30, 31]. Theoretical works have predicted the existence of a curvature-induced effective anisotropy and DM-like interaction that enable novel effects including magnetochiral effects (chirality symmetry breaking) and topologically induced magnetization patterning.

Targeting those theoretical predictions, we presented relevant experimental approaches to synthesize curved magnetic objects. Curved quasi-1D nanowires can be formed using either anodization approaches or GLAD techniques, which allow to realize magnetic cylinders and hollow tubes, straight, bent or shaped as nanohelices. Remarkably small dimensions of nanohelices down to 50 nm diameter were achieved using GLAD approaches [86]. Those structures are fundamentally interesting since they are supposed to show curvature-induced effects; An experimental verification is yet to be given.

Ultimately small magnetic helices could be achieved by means of DNA origami [404]. It is a well-established method to realize chiral structures of, e.g. optically active Au nanoparticles at the nanoscale [405]. An application to magnetic materials, e.g. the realization of helices with magnetic nanoparticles, has not yet been reported. We hope that the work in hand will initiate close collaboration between the magnetism and DNA origami communities to address the fundamental question on the impact of curvature on the magnetic responses at the nanoscale.

Magnetic 2D shells can be prepared in a straightforward way by deposition of magnetic thin films on curvature templates, e.g. spherical, conical or cylindrical objects. We reviewed different methods, which can be applied to realize the curvature templates offering radii of curvature over three orders of magnitude (10 nm to 10 μm). Magnetic responses (mainly, statics) of distinct material systems with in-plane and out-of-plane easy axis of magnetization were discussed. A new approach of shaping initially planar magnetic thin films into 3D tubular objects relying on strain engineering was highlighted. Different shapes including Swiss rolls and microhelices have already been accomplished by those means, which allow for engineering artificial micro- and nano-structures with unique magnetic configurations. From a theoretical point of view, radially magnetized curved architectures like Swiss roll structures lack inversion- as well as time-reversal symmetry and are therefore characterized by a geometrically induced ferro-toroidic order. The possibility to design a finite toroidal moment by nanofabrication techniques could potentially open new avenues to study this type of long-range order and its role in multiferroic behavior.

The optimization of the magnetic and structural properties of these novel 3D architectures demands the development of new characterization methods, particularly those based on vector tomographic imaging. Magnetic neutron tomography [105, 106] and electron-based 3D imaging, such as electron holography [76, 77, 107, 108] and vector field electron tomography [109, 110], are well-established techniques to investigate macroscopic and nanoscopic samples, respectively. Electron-based tomography provided first insights into the magnetization patterns of nanohelices [77]. We envision that curvature effects in nanoobjects will be investigated using such techniques. On the other side, at the mesoscale, curved objects like Swiss rolls can be investigated using the novel method of magnetic soft x-ray tomography (MXT) [96]. Providing means to study samples with thicknesses up to 200 nm, MXT closes the gap between investigating 3D magnetic nanostructures and bulky crystals using electron-based 3D imaging and neutron tomography, respectively. Composite materials with even larger thickness may be investigated element specifically due to an effectively reduced absorption cross-section at resonance. To fully exploit its potential, further developments are required. They rely on three major aspects, namely generalization of the present algorithm, application to various sample architectures and realization of a 3D rotation of an object in an x-ray microscope. The latter requirement is technically challenging due to a fixed rotation axis in T-XPEEM [116] and a spatial separation of merely 2 mm between pinhole and vacuum window in TXM [249]. The realization may still be possible since tilts around two additional preferentially orthogonal rotation axes would be sufficient for most cases. We envision that these yet fundamental investigations will have strong impact on future explorations of the application potential of 3D objects as e.g. GMI-based sensors for magnetoencephalography in life sciences, as topology-induced magnetoelectrics, unidirectional magnonic systems or racetrack memory devices for green electronics, or as prototypical models for advancing vector field tomography, such as magnetic x-ray tomography. Developing next generation diffraction-limited x-ray sources and advancing coherent imaging techniques, such as x-ray holography [253, 406–414] and ptychography [415–423], will further promote soft x-ray based vector field tomography with nanometer spatial resolution in all three dimensions.

At the moment, most experimental works have been focused on static magnetic properties of curved magnetic thin films. However, dynamic aspects are even richer in physics with predicted unlimited domain wall velocities [37] as relevant for racetrack memory applications or Cherenkov-like effect for magnons [38]. Furthermore, the fabrication of curved heterostructures by tightly rolling up provides means to assemble magnetic field-tunable metamaterials based on magnonic excitations that function as hyperlenses with cylindrical shape [424–427]. On the other hand, rolling up magnetic honeycomb lattices [266] into cylindrical objects with well-defined orientation could result in 3D magnonic crystals, which offer a magnetic field control through the energy band gaps detectable by Brillouin light scattering (BLS) microspectroscopy [428].

In spite of experimental challenges to address the appealing theoretical predictions of curvature-induced effects, 3D magnetic architectures have already proven their application potential for life sciences, targeted delivery, realization of 3D spin-wave filters, and magneto-encephalography devices. The originally fundamental topic of the magnetism in curved geometries strongly benefited from contributions by the application-oriented community, which among others explore the shapeability aspect of the curved magnetic thin films. These activities resulted in the development of the family of shapeable magnetoelectronics [95] including flexible [429–431], printable [432–434], stretchable [91, 429] and even imperceptible [94] magnetic field sensorics.

The balance between fundamental and applied stimuli to the topic of magnetism in curved geometries is quite unique and triggered the development of new theoretical methods and novel fabrication/characterization techniques. This synergy will enable us to exceed the exploratory stage of research and paves the way towards novel device concepts, whose functionality and performance will harness the geometry of 3D magnetic thin films.

Acknowledgments

We appreciate insightful discussions with Dr U K Rößler, Dr C Ortix, Dr J I Mönch, D Karnaushenko and Prof R Schäfer (all IFW Dresden), Prof M Poggio (University of Basel), Prof R Hertel (University of Strasbourg), Dr A Kakay, Dr K Lenz and Prof J Faßbender (all Helmholtz-Zentrum Dresden-Rossendorf), Prof M Kläui (University of Mainz), Prof P Landeros and Dr J Otalora (Universidad Tecnica Federico Santa Maria), Prof M Albrecht (University of Augsburg), Dr A A Unal, Dr F Radu and Dr R Abrudan (all Helmholtz-Zentrum Berlin, BESSY II), Dr L Baraban (Dresden University of Technology), Prof K Liu (University of California, Davis), Prof J Deutsch (University of California, Santa Cruz), Dr A Petford-Long and Dr C Phatak (all Argonne National Laboratory) and Dr P Ercius (Lawrence Berkeley National Laboratory). We thank Dr M-Y Im (Lawrence Berkeley National Laboratory) for experimental help with the TXM at the Lawrence Berkeley National Laboratory. This work was financially supported in part via the European Research Council under the European Union's Seventh Framework program (FP7/2007-2013)/ ERC grant agreement n.306277, the Future and Emerging Technologies (FET) programme under FET-Open grant number 618083, the German Science Foundation (DFG) grant MA 5144/1-1, MA 5144/2-1, MA 5144/3-1, SCHM 1298/14-1 and the DFG Research Unit 1713. RS and PF acknowledge financial support by the Director, Office of Science, Office of Basic Energy Sciences, Materials Sciences and Engineering Division, of the U.S. Department of Energy under Contract No. DE-AC02-05-CH11231 in the Nonequilibrium Magnetic Materials program.

References

[1] Kuratsuji H 2012 *Phys. Rev.* E **85** 031150
[2] Tempere J, Gladilin V N, Silvera I F, Devreese J T and Moshchalkov V V 2009 *Phys. Rev.* B **79** 134516
[3] Fomin V M, Rezaev R O and Schmidt O G 2012 *Nano Lett.* **12** 1282–87
[4] Lopez-Leon T, Koning V, Devaiah K B S, Vitelli V and Fernandez-Nieves A 2011 *Nat. Phys.* **7** 391–4
[5] De Gennes P G and Prost J 1993 *The Physics of Liquid Crystals* 2nd edn (Oxford: Clarendon)
[6] Ganser B K, Li S, Klishko V Y, Finch J T and Sundquist W I 1999 *Science* **283** 80–3 (preprint www.sciencemag.org/content/283/5398/80.full.pdf)
[7] McMahon H T and Gallop J L 2005 *Nature* **438** 590–6
[8] Forgan R S, Sauvage J P and Stoddart J F 2011 *Chem. Rev.* **111** 5434–64
[9] Bowick M J and Giomi L 2009 *Adv. Phys.* **58** 449–563
[10] Turner A M, Vitelli V and Nelson D R 2010 *Rev. Mod. Phys.* **82** 1301–48
[11] Lewis E R, Petit D, Thevenard L, Jausovec A V, O'Brien L, Read D E and Cowburn R P 2009 *Appl. Phys. Lett.* **95** 152505
[12] Glathe S and Mattheis R 2012 *Phys. Rev.* B **85** 024405
[13] Tkachenko V S, Kuchko A N, Dvornik M and Kruglyak V V 2012 *Appl. Phys. Lett.* **101** 152402
[14] Burn D M, Chadha M, Walton S K and Branford W R 2014 *Phys. Rev.* B **90** 144414
[15] Smith E J, Makarov D, Sanchez S, Fomin V M and Schmidt O G 2011 *Phys. Rev. Lett.* **107** 097204
[16] Tkachenko V S, Kuchko A N and Kruglyak V V 2013 *Low Temp. Phys.* **39** 163
[17] Mark A G, Gibbs J G, Lee T C and Fischer P 2013 *Nat. Mater.* **12** 802–7
[18] Tomita S, Sawada K, Porokhnyuk A and Ueda T 2014 *Phys. Rev. Lett.* **113** 235501
[19] Sheka D D, Kravchuk V P, Yershov K V and Gaididei Y 2015 *Phys. Rev.* B **92** 054417
[20] Albrecht M, Hu G, Guhr I L, Ulbrich T C, Boneberg J, Leiderer P and Schatz G 2005 *Nat. Mater.* **4** 203–6
[21] Sapozhnikov M V, Ermolaeva O L, Gribkov B G, Nefedov I M, Karetnikova I R, Gusev S A, Rogov V V, Troitskii B B and Khokhlova L V 2012 *Phys. Rev.* B **85** 054402
[22] Kravchuk V P, Sheka D D, Streubel R, Makarov D, Schmidt O G and Gaididei Y 2012 *Phys. Rev.* B **85** 144433
[23] Nissen D, Mitin D, Klein O, Arekapudi S S P K, Thomas S, Im M Y, Fischer P and Albrecht M 2015 *Nanotechnology* **26** 465706
[24] Ulbrich T C, Makarov D, Hu G, Guhr I L, Suess D, Schrefl T and Albrecht M 2006 *Phys. Rev. Lett.* **96** 077202
[25] Soares M M, de Biasi E, Coelho L N, dos Santos M C, de Menezes F S, Knobel M, Sampaio L C and Garcia F 2008 *Phys. Rev.* B **77** 224405
[26] Hertel R 2013 *SPIN* **03** 1340009
[27] Landeros P and Núnez A S 2010 *J. Appl. Phys.* **108** 033917
[28] Weber D P, Rüffer D, Buchter A, Xue F, Russo-Averchi E, Huber R, Berberich P, Arbiol J, Fontcuberta i Morral A, Grundler D and Poggio M 2012 *Nano Lett.* **12** 6139–44
[29] Pylypovskyi O V, Kravchuk V P, Sheka D D, Makarov D, Schmidt O G and Gaididei Y 2015 *Phys. Rev. Lett.* **114** 197204
[30] Gaididei Y, Kravchuk V P and Sheka D D 2014 *Phys. Rev. Lett.* **112** 257203
[31] Sheka D D, Kravchuk V P and Gaididei Y 2015 *J. Phys. A: Math. Theor.* **48** 125202
[32] Dietrich C, Hertel R, Huber M, Weiss D, Schäfer R and Zweck J 2008 *Phys. Rev.* B **77** 174427
[33] Yan M, Andreas C, Kákay A, Garcia-Sanchez F and Hertel R 2011 *Appl. Phys. Lett.* **99** 122505
[34] Yan M, Andreas C, Kákay A, Garcia-Sanchez F and Hertel R 2012 *Appl. Phys. Lett.* **100** 252401
[35] Otálora J, López-López J, Vargas P and Landeros P 2012 *Appl. Phys. Lett.* **100** 072407
[36] Sloika M I, Kravchuk V P, Sheka D D and Gaididei Y 2014 *Appl. Phys. Lett.* **104** 252403
[37] Yan M, Kákay A, Gliga S and Hertel R 2010 *Phys. Rev. Lett.* **104** 057201
[38] Yan M, Kákay A, Andreas C and Hertel R 2013 *Phys. Rev.* B **88** 220412
[39] Mönch I, Makarov D, Koseva R, Baraban L, Karnaushenko D, Kaiser C, Arndt K F and Schmidt O G 2011 *ACS Nano* **5** 7436–42
[40] Müller C, Bof Bufon C C, Navarro Fuentes M E, Makarov D, Mosca D H and Schmidt O G 2012 *Appl. Phys. Lett.* **100** 022409
[41] Balhorn F, Mansfeld S, Krohn A, Topp J, Hansen W, Heitmann D and Mendach S 2010 *Phys. Rev. Lett.* **104** 037205
[42] Balhorn F, Jeni S, Hansen W, Heitmann D and Mendach S 2012 *Appl. Phys. Lett.* **100** 222402
[43] Liu L, Ioannides A and Streit M 1999 *Brain Topogr.* **11** 291–303
[44] Dumas T, Dubal S, Attal Y, Chupin M, Jouvent R, Morel S and George N 2013 *PLoS One* **8** e74145
[45] Karnaushenko D, Karnaushenko D D, Makarov D, Baunack S, Schäfer R and Schmidt O G 2015 *Adv. Mater.* **27** 6582–9
[46] Parkin S S P, Hayashi M and Thomas L 2008 *Science* **320** 190–4
[47] Nielsch K, Müller F, Li A P and Gösele U 2000 *Adv. Mater.* **12** 582–6

[48] Nielsch K, Wehrspohn R B, Barthel J, Kirschner J, Gösele U, Fischer S F and Kronmüller H 2001 *Appl. Phys. Lett.* **79** 1360
[49] Vock S, Hengst C, Wolf M, Tschulik K, Uhlemann M, Sasvári Z, Makarov D, Schmidt O G, Schultz L and Neu V 2014 *Appl. Phys. Lett.* **105** 172409
[50] Wegrowe J E, Kelly D, Franck A, Gilbert S E and Ansermet J P 1999 *Phys. Rev. Lett.* **82** 3681–4
[51] Sellmyer D J, Zheng M and Skomski R 2001 *J. Phys.: Condens. Matter* **13** R433–60
[52] Kimling J, Kronast F, Martens S, Böhnert T, Martens M, Herrero-Albillos J, Tati-Bismaths L, Merkt U, Nielsch K and Meier G 2011 *Phys. Rev.* B **84** 174406
[53] Chong Y T, Görlitz D, Martens S, Yau M Y E, Allende S, Bachmann J and Nielsch K 2010 *Adv. Mater.* **22** 2435–9
[54] Bachmann J, Jing J, Knez M, Barth S, Shen H, Mathur S, Gösele U and Nielsch K 2007 *J. Am. Chem. Soc.* **129** 9554–5
[55] Rüffer D, Huber R, Berberich P, Albert S, Russo-Averchi E, Heiss M, Arbiol J, Fontcuberta i Morral A and Grundler D 2012 *Nanoscale* **4** 4989
[56] Buchter A, Nagel J and Rüffer D 2013 *Phys. Rev. Lett.* **111** 067202
[57] Streubel R, Thurmer D J, Makarov D, Kronast F, Kosub T, Kravchuk V, Sheka D D, Gaididei Y, Schaefer R and Schmidt O G 2012 *Nano Lett.* **12** 3961–6
[58] Albrecht M and Makarov D 2012 *Open Surf. Sci. J.* **4** 42–54
[59] Streubel R, Kravchuk V P, Sheka D D, Makarov D, Kronast F, Schmidt O G and Gaididei Y 2012 *Appl. Phys. Lett.* **101** 132419
[60] Baraban L, Makarov D, Schmidt O G, Cuniberti G, Leiderer P and Erbe A 2013 *Nanoscale* **5** 1332–6
[61] Teichert C 2003 *Appl. Phys. A: Mater. Sci. Process.* **76** 653–64
[62] Liedke M O, Körner M, Lenz K, Grossmann F, Facsko S and Fassbender J 2012 *Appl. Phys. Lett.* **100** 242405
[63] Liedke M O *et al* 2013 *Phys. Rev.* B **87** 024424
[64] Ball D K, Lenz K, Fritzsche M, Varvaro G, Günther S, Krone P, Makarov D, Mücklich A, Facsko S, Fassbender J and Albrecht M 2014 *Nanotechnology* **25** 085703
[65] Makarov D, Ureña E B, Schmidt O G, Liscio F, Maret M, Brombacher C, Schulze S, Hietschold M and Albrecht M 2008 *Appl. Phys. Lett.* **93** 153112
[66] Makarov D, Klimenta F, Fischer S, Liscio F, Schulze S, Hietschold M, Maret M and Albrecht M 2009 *J. Appl. Phys.* **106** 114322
[67] Baraban L, Makarov D, Albrecht M, Rivier N, Leiderer P and Erbe A 2008 *Phys. Rev.* E **77** 031407
[68] Baraban L, Streubel R, Makarov D, Han L, Karnaushenko D, Schmidt O G and Cuniberti G 2013 *ACS Nano* **7** 1360–7
[69] Baraban L, Makarov D, Streubel R, Mönch I, Grimm D, Sanchez S and Schmidt O G 2012 *ACS Nano* **6** 3383–9
[70] Kumar A, Fähler S, Schlörb H, Leistner K and Schultz L 2006 *Phys. Rev.* B **73** 064421
[71] Vázquez M and Vivas L G 2011 *Phys. Status Solidi* B **248** 2368–81
[72] Brombacher C, Falke M, Springer F, Rohrmann H, Goncharov A, Schrefl T, Bleloch A and Albrecht M 2010 *Appl. Phys. Lett.* **97** 102508
[73] Guhr I L, van Dijken S, Malinowski G, Fischer P, Springer F, Hellwig O and Albrecht M 2007 *J. Phys. D: Appl. Phys.* **40** 3005–10
[74] Streubel R, Kronast F, Reiche C F, Mühl T, Wolter A U B, Schmidt O G and Makarov D 2016 *Appl. Phys. Lett.* **108** 042407
[75] Nielsch K, Wehrspohn R, Barthel J, Kirschner J, Fischer S, Kronmüller H, Schweinböck T, Weiss D and Gösele U 2002 *J. Magn. Magn. Mater.* **249** 234–40
[76] Biziere N, Gatel C, Lassalle-Balier R, Clochard M C, Wegrowe J E and Snoeck E 2013 *Nano Lett.* **13** 2053–7
[77] Phatak C, Liu Y, Gulsoy E B, Schmidt D, Franke-Schubert E and Petford-Long A 2014 *Nano Lett.* **14** 759–64
[78] Streubel R, Makarov D, Kronast F, Kravchuk V, Albrecht M and Schmidt O G 2012 *Phys. Rev.* B **85** 174429
[79] Streubel R, Han L, Im M Y, Kronast F, Rößler U K, Radu F, Abrudan R, Lin G, Schmidt O G, Fischer P and Makarov D 2015 *Sci. Rep.* **5** 8787
[80] Eimüller T, Ulbrich T C, Amaladass E, Guhr I L, Tyliszczak T and Albrecht M 2008 *Phys. Rev.* B **77** 134415
[81] Günther C M *et al* 2010 *Phys. Rev.* B **81** 064411
[82] Young N O and Kowal J 1959 *Nature* **183** 104–5
[83] Zhao Y P, Ye D X, Wang G C and Lu T M 2002 *Nano Lett.* **2** 351–4
[84] Dick B, Brett M J, Smy T J, Freeman M R, Malac M and Egerton R F 2000 *J. Vac. Sci. Technol. A: Vac. Surf. Films* **18** 1838
[85] He Y, Fu J, Zhang Y, Zhao Y, Zhang L, Xia A and Cai J 2007 *Small* **3** 153–60
[86] Gibbs J G, Mark A G, Lee T C, Eslami S, Schamel D and Fischer P 2014 *Nanoscale* **6** 9457
[87] Schmidt O G and Eberl K 2001 *Nature* **410** 168–8
[88] Prinz V, Seleznev V, Gutakovsky A, Chehovskiy A, Preobrazhenskii V, Putyato M and Gavrilova T 2000 *Phys. E: Low-Dimens. Syst. Nanostruct.* **6** 828–31
[89] Luchnikov V, Sydorenko O and Stamm M 2005 *Adv. Mater.* **17** 1177–82
[90] Mei Y, Huang G, Solovev A A, Ureña E B, Mönch I, Ding F, Reindl T, Fu R K Y, Chu P K and Schmidt O G 2008 *Adv. Mater.* **20** 4085–90
[91] Melzer M, Makarov D, Calvimontes A, Karnaushenko D, Baunack S, Kaltofen R, Mei Y and Schmidt O G 2011 *Nano Lett.* **11** 2522–6
[92] Melzer M, Lin G, Makarov D and Schmidt O G 2012 *Adv. Mater.* **24** 6468–72
[93] Melzer M, Karnaushenko D, Makarov D, Baraban L, Calvimontes A, Mönch I, Kaltofen R, Mei Y and Schmidt O G 2012 *RSC Adv.* **2** 2284
[94] Melzer M, Kaltenbrunner M, Makarov D, Karnaushenko D, Karnaushenko D, Sekitani T, Someya T and Schmidt O G 2015 *Nat. Commun.* **6** 6080
[95] Makarov D, Melzer M, Karnaushenko D and Schmidt O G 2016 *Appl. Phys. Rev.* **3** 011101
[96] Streubel R, Kronast F, Fischer P, Parkinson D, Schmidt O G and Makarov D 2015 *Nat. Commun.* **6** 7612
[97] Ureña E B, Mei Y, Coric E, Makarov D, Albrecht M and Schmidt O G 2009 *J. Phys. D: Appl. Phys.* **42** 055001
[98] Smith E J, Makarov D and Schmidt O G 2011 *Soft Matter* **7** 11309
[99] Fomin V M, Smith E J, Makarov D, Sanchez S and Schmidt O G 2011 *Phys. Rev.* B **84** 174303
[100] Schumann J, Lisunov K G, Escoffier W, Raquet B, Broto J M, Arushanov E, Mönch I, Makarov D, Deneke C and Schmidt O G 2012 *Nanotechnology* **23** 255701
[101] Streubel R, Makarov D, Lee J, Müller C, Melzer M, Schäfer R, Bufon C C B, Kim S K and Schmidt O G 2013 *SPIN* **03** 1340001
[102] Müller C, Bufon C C B, Makarov D, Fernandez-Outon L E, Macedo W A A, Schmidt O G and Mosca D H 2012 *Nanoscale* **4** 7155
[103] Streubel R, Han L, Kronast F, Ünal A A, Schmidt O G and Makarov D 2014 *Nano Lett.* **14** 3981–6
[104] Streubel R, Lee J, Makarov D, Im M Y, Karnaushenko D, Han L, Schäfer R, Fischer P, Kim S K and Schmidt O G 2014 *Adv. Mater.* **26** 316–23
[105] Kardjilov N, Manke I, Strobl M, Hilger A, Treimer W, Meissner M, Krist T and Banhart J 2008 *Nat. Phys.* **4** 399–403

[106] Manke I *et al* 2010 *Nat. Commun.* **1** 125
[107] Dunin-Borkowski R E, McCartney M R, Frankel R B, Bazylinski D A, Pósfai M and Buseck P R 1998 *Science* **282** 1868–70
[108] Tripp S L, Dunin-Borkowski R E and Wei A 2003 *Angew. Chem. Int. Ed.* **42** 5591–3
[109] Phatak C, Petford-Long A K and Graef M D 2010 *Phys. Rev. Lett.* **104** 253901
[110] Tanigaki T, Takahashi Y, Shimakura T, Akashi T, Tsuneta R, Sugawara A and Shindo D 2015 *Nano Lett.* **15** 1309–14
[111] Schütz G, Wagner W, Wilhelm W, Kienle P, Zeller R, Frahm R and Materlik G 1987 *Phys. Rev. Lett.* **58** 737–40
[112] Chen C T, Sette F, Ma Y and Modesti S 1990 *Phys. Rev.* B **42** 7262–5
[113] Thole B T, Carra P, Sette F and van der Laan G 1992 *Phys. Rev. Lett.* **68** 1943–6
[114] Carra P, Thole B T, Altarelli M and Wang X 1993 *Phys. Rev. Lett.* **70** 694–7
[115] Stöhr J 1995 *J. Electron Spectrosc. Relat. Phenom.* **75** 253–72
[116] Kronast F, Schlichting J, Radu F, Mishra S, Noll T and Dürr H 2010 *Surf. Interface Anal.* **42** 1532–6
[117] Evans N D, Gentleman E and Polak J M 2006 *Mater. Today* **9** 26–33
[118] Fischer P *et al* 2001 *Rev. Sci. Instrum.* **72** 2322
[119] Arnold J R, Testa J P, Friedman P J and Kambic G X 1983 *Science* **219** 383–4
[120] Carlson W D and Denison C 1992 *Science* **257** 1236–9
[121] Kinney J H, Breunig T M, Starr T L, Haupt D, Nichols M C, Stock S R, Butts M D and Saroyan R A 1993 *Science* **260** 789–92
[122] Carrascosa J L, Chichón F J, Pereiro E, Rodríguez M J, Fernández J J, Esteban M, Heim S, Guttmann P and Schneider G 2009 *J. Struct. Biol.* **168** 234–9
[123] Schneider G, Guttmann P, Heim S, Rehbein S, Mueller F, Nagashima K, Heymann J B, Müller W G and McNally J G 2010 *Nat. Methods* **7** 985–7
[124] Hummel E, Guttmann P, Werner S, Tarek B, Schneider G, Kunz M, Frangakis A S and Westermann B 2012 *PLoS One* **7** e53293
[125] DeWitt B S 1957 *Rev. Mod. Phys.* **29** 377–97
[126] Jensen H and Koppe H 1971 *Ann. Phys.* **63** 586–91
[127] da Costa R C T 1981 *Phys. Rev.* A **23** 1982–7
[128] Kaplan L, Maitra N T and Heller E J 1997 *Phys. Rev.* A **56** 2592–9
[129] Wang Y L and Zong H S 2016 *Ann. Phys.* **364** 68–78
[130] Burgess M and Jensen B 1993 *Phys. Rev.* A **48** 1861–8
[131] Gaididei Y B, Mingaleev S and Christiansen P 2000 *Phys. Rev.* E **62** R53
[132] Aoki H, Koshino M, Takeda D, Morise H and Kuroki K 2001 *Phys. Rev.* B **65** 035102
[133] Entin M and Magarill L 2002 *Phys. Rev.* B **66** 205308
[134] Gorria C, Gaididei Y B, Soerensen M P, Christiansen P L and Caputo J G 2004 *Phys. Rev.* B **69** 134506
[135] Chaplik A V and Blick R H 2004 *New J. Phys.* **6** 33–3
[136] Magarill L I, Chaplik A V and Entin M V 2005 *Phys.—Usp.* **48** 953–8
[137] Gaididei Y B, Christiansen P L, Kevrekidis P G, Büttner H and Bishop A R 2005 *New J. Phys.* **7** 52
[138] Ferrari G and Cuoghi G 2008 *Phys. Rev. Lett.* **100** 230403
[139] Jensen B and Dandoloff R 2009 *Phys. Rev.* A **80** 052109
[140] Cuoghi G, Ferrari G and Bertoni A 2009 *Phys. Rev.* B **79** 073410
[141] Korte A P and van der Heijden G H M 2009 *J. Phys.: Condens. Matter* **21** 495301
[142] Ortix C, Kiravittaya S, Schmidt O G and van den Brink J 2011 *Phys. Rev.* B **84** 045438
[143] Bittner S, Dietz B, Miski-Oglu M, Richter A, Ripp C, Sadurní E and Schleich W P 2013 *Phys. Rev.* E **87** 042912
[144] Belov V V, Dobrokhotov S Y and Tudorovskii T Y 2004 *Theor. Math. Phys.* **141** 1562–92
[145] Belov V V, Dobrokhotov S Y, Maslov V P and Tudorovski T Y 2005 *Phys.—Usp.* **48** 962
[146] Belov V V and Nikolaev S V 2007 *Dokl. Math.* **75** 147–52
[147] Ortix C 2015 *Phys. Rev.* B **91** 245412
[148] Kamien R 2002 *Rev. Mod. Phys.* **74** 953–71
[149] Nelson D, Weinberg S and Piran T 2004 *Statistical Mechanics of Membranes and Surfaces* 2nd edn (River Edge, NJ: World Scientific)
[150] Pismen L M 1999 *Vortices in Nonlinear Field* (Oxford University Press)
[151] Napoli G and Vergori L 2012 *Phys. Rev. Lett.* **108** 207803
[152] Napoli G and Vergori L 2012 *Phys. Rev.* E **85** 061701
[153] Napoli G and Vergori L 2013 *Soft Matter* **9** 8378
[154] Napoli G and Vergori L 2013 *Int. J. Nonlinear Mech.* **49** 66–71
[155] Segatti A, Snarski M and Veneroni M 2014 *Phys. Rev.* E **90** 012501
[156] Manyuhina O V 2014 *Phys. Rev.* E **90** 022713
[157] de Oliveira E J L, de Oliveira I N, Lyra M L and Mirantsev L V 2016 *Phys. Rev.* E **93** 012703
[158] Vitelli V and Turner A M 2004 *Phys. Rev. Lett.* **93** 215301
[159] Saxena A, Dandoloff R and Lookman T 1998 *Phys. A: Stat. Theor. Phys.* **261** 13–25
[160] Carvalho-Santos V L, Moura A R, Moura-Melo W A and Pereira A R 2008 *Phys. Rev.* B **77** 134450
[161] Carvalho-Santos V L, Moura-Melo W A and Pereira A R 2010 *J. Appl. Phys.* **108** 094310
[162] Freitas W A, Moura-Melo W A and Pereira A 2005 *Phys. Lett.* A **336** 412–22
[163] Moura-Melo W, Pereira A, Mol L and Pires A 2007 *Phys. Lett.* A **360** 472–80
[164] Dandoloff R, Villain-Guillot S, Saxena A and Bishop A R 1995 *Phys. Rev. Lett.* **74** 813–5
[165] Dandoloff R and Saxena A 2011 *J. Phys. A: Math. Theor.* **44** 045203
[166] Carvalho-Santos V L, Elias R G, Fonseca J M and Altbir D 2015 *J. Appl. Phys.* **117** 17E518
[167] Carvalho-Santos V L and Dandoloff R 2012 *Phys. Lett.* A **376** 3551–4
[168] Pylypovskyi O V, Sheka D D, Kravchuk V P, Yershov K V, Makarov D and Gaididei Y 2016 *Sci. Rep.* **6** 23316
[169] Landeros P, Allende S, Escrig J, Salcedo E, Altbir D and Vogel E E 2007 *Appl. Phys. Lett.* **90** 102501
[170] Landeros P, Guzman P R, Soto-Garrido R and Escrig J 2009 *J. Phys. D: Appl. Phys.* **42** 225002
[171] Landeros P, Suarez O J, Cuchillo A and Vargas P 2009 *Phys. Rev.* B **79** 024404
[172] González A, Landeros P and Núñez Á S 2010 *J. Magn. Magn. Mater.* **322** 530–5
[173] López-López J A, Cortés-Ortuño D and Landeros P 2012 *J. Magn. Magn. Mater.* **324** 2024–9
[174] Kläui M, Vaz C A F, Lopez-Diaz L and Bland J A C 2003 *J. Phys.: Condens. Matter* **15** R985–1024
[175] Guimarães A P 2009 *Principles of Nanomagnetism* (*NanoScience and Technology*) (Berlin: Springer)
[176] Milnor J 1978 *Am. Math. Mon.* **85** 521–4
[177] Yoneya M, Kuboki K and Hayashi M 2008 *Phys. Rev.* B **78** 064419
[178] Berry M V 1984 *Proc. R. Soc.* A **392** 45–57
[179] Hubert A and Schäfer R 1998 *Magnetic Domains: the Analysis of Magnetic Microstructures* (Berlin: Springer)
[180] Shinjo T, Okuno T, Hassdorf R, Shigeto K and Ono T 2000 *Science* **289** 930–2 (preprint www.sciencemag.org/cgi/reprint/289/5481/930.pdf)
[181] Wachowiak A, Wiebe J, Bode M, Pietzsch O, Morgenstern M and Wiesendanger R 2002 *Science* **298** 577–80

[182] Curcic M *et al* 2008 *Phys. Rev. Lett.* **101** 197204
[183] Vansteenkiste A, Weigand M, Curcic M, Stoll H, Schütz G and Waeyenberge B V 2009 *New J. Phys.* **11** 063006
[184] Im M Y, Fischer P, Yamada K, Sato T, Kasai S, Nakatani Y and Ono T 2012 *Nat. Commun.* **3** 983
[185] Sheka D D, Kravchuk V P, Sloika M I and Gaididei Y 2013 *SPIN* **3** 1340003
[186] Yershov K V, Kravchuk V P, Sheka D D and Gaididei Y 2015 *J. Appl. Phys.* **117** 083908
[187] Sheka D D, Yastremsky I A, Ivanov B A, Wysin G M and Mertens F G 2004 *Phys. Rev.* B **69** 054429
[188] Guslienko K Y, Slavin A N, Tiberkevich V and Kim S K 2008 *Phys. Rev. Lett.* **101** 247203
[189] Guslienko K Y, Aranda G R and Gonzalez J M 2010 *Phys. Rev.* B **81** 014414
[190] Otálora J, López-López J, Landeros P, Vargas P and Nunez A 2013 *J. Magn. Magn. Mater.* **341** 86–92
[191] Schryer N L and Walker L R 1974 *J. Appl. Phys.* **45** 5406–21
[192] Dzialoshinskii I E 1957 *Sov. Phys.—JETP* **5** 1259–72
[193] Dzyaloshinsky I 1958 *J. Phys. Chem. Solids* **4** 241–55
[194] Zakeri K, Zhang Y, Prokop J, Chuang T H, Sakr N, Tang W X and Kirschner J 2010 *Phys. Rev. Lett.* **104** 137203
[195] Cortes-Ortuno D and Landeros P 2013 *J. Phys.: Condens. Matter* **25** 156001
[196] Zakeri K 2014 *Phys. Rep.* **545** 47–93 (elementary spin excitations in ultrathin itinerant magnets)
[197] Allwood D A, Xiong G, Cooke M D, Faulkner C C, Vernier D A N and Cowburn R P 2002 *Science* **296** 2003–6
[198] Allwood D A, Xiong G, Faulkner C C, Atkinson D, Petit D and Cowburn R P 2005 *Science* **309** 1688–92
[199] Xu P, Xia K, Gu C, Tang L, Yang H and Li J 2008 *Nat. Nanotechnol.* **3** 97–100
[200] Hayashi M, Thomas L, Moriya R, Rettner C and Parkin S S P 2008 *Science* **320** 209–11
[201] Catalan G, Seidel J, Ramesh R and Scott J F 2012 *Rev. Mod. Phys.* **84** 119–56
[202] Kläui M, Vaz C A F, Rothman J, Bland J A C, Faini W W G and Cambril E 2003 *Phys. Rev. Lett.* **90** 097202
[203] Kläui M *et al* 2005 *Appl. Phys. Lett.* **87** 102509
[204] Hayashi M, Thomas L, Rettner C, Moriya R, Jiang X and Parkin S S P 2006 *Phys. Rev. Lett.* **97** 207205
[205] Bedau D, Klaui M, Krzyk S, Rudiger U, Faini G and Vila L 2007 *Phys. Rev. Lett.* **99** 146601
[206] Atkinson D, Eastwood D S and Bogart L K 2008 *Appl. Phys. Lett.* **92** 022510
[207] Bogart L, Atkinson D, O'Shea K, McGrouther D and McVitie S 2009 *Phys. Rev.* B **79** 054414
[208] Petit D *et al* 2010 *Appl. Phys. Lett.* **97** 233102
[209] Kim J S *et al* 2014 *Nat. Commun.* **5** 3429
[210] Nakatani Y, Thiaville A and Miltat J 2003 *Nat. Mater.* **2** 521–3
[211] Thiaville A, Nakatani Y, Miltat J and Vernier N 2004 *J. Appl. Phys.* **95** 7049–51
[212] Thiaville A, Nakatani Y, Miltat J and Suzuki Y 2005 *Europhys. Lett.* **69** 990–6
[213] Ivanov A A and Orlov V A 2011 *Phys. Solid State* **53** 2441–9
[214] Uhlíř V *et al* 2010 *Phys. Rev.* B **81** 224418
[215] Gerhardt T, Drews A and Meier G 2011 *J. Phys.: Condens. Matter* **24** 024208
[216] Yershov K V, Kravchuk V P, Sheka D D and Gaididei Y 2015 *Phys. Rev.* B **92** 104412
[217] Hayward T J, Bryan M T, Fry P W, Fundi P M, Gibbs M R J, Allwood D A, Im M Y and Fischer P 2010 *Phys. Rev.* B **81** 020410
[218] Hayward T J, Bryan M T, Fry P W, Fundi P M, Gibbs M R J, Im M Y, Fischer P and Allwood D A 2010 *Appl. Phys. Lett.* **96** 052502
[219] Hodges M P P, Bryan M T, Fry P W, Im M Y, Fischer P and Hayward T J 2014 *J. Appl. Phys.* **116** 123914
[220] Yershov K V, Kravchuk V P, Sheka D D and Gaididei Y 2016 *Phys. Rev.* B **93** 094418
[221] Freimuth F, Blügel S and Mokrousov Y 2014 *J. Phys.: Condens. Matter* **26** 104202
[222] Koike K and Hayakawa K 1984 *Japan. J. Appl. Phys.* **23** L187
[223] Koike K and Hayakawa K 1984 *Appl. Phys. Lett.* **45** 585–6
[224] Oepen H P and Kirschner J 1989 *Phys. Rev. Lett.* **62** 819–22
[225] Scheinfein M R, Unguris J, Kelley M H, Pierce D T and Celotta R J 1990 *Rev. Sci. Instrum.* **61** 2501–27
[226] Oepen H and Hopster H 2005 *SEMPA Studies of Thin Films, Structures, and Exchange Coupled Layers* (Berlin: Springer) pp 137–67
[227] Duden T and Bauer E 1995 *Rev. Sci. Instrum.* **66** 2861–4
[228] El Gabaly F, Gallego S, Munoz C, Szunyogh L, Weinberger P, Klein C, Schmid A K, McCarty K F and de la Figuera J 2006 *Phys. Rev. Lett.* **96** 147202
[229] Bode M 2003 *Rep. Prog. Phys.* **66** 523
[230] Pratzer M, Elmers H J, Bode M, Pietzsch O, Kubetzka A and Wiesendanger R 2001 *Phys. Rev. Lett.* **87** 127201
[231] Chen J P, Wang Z Q, Gong J J, Qin M H, Zeng M, Gao X S and Liu J M 2013 *J. Appl. Phys.* **113** 054312
[232] Chen G *et al* 2013 *Phys. Rev. Lett.* **110** 177204
[233] Chen G and Schmid A K 2015 *Adv. Mater.* **27** 5738–43
[234] Heinze S, Bode M, Kubetzka A, Pietzsch O, Nie X, Blügel S and Wiesendanger R 2000 *Science* **288** 1805–8
[235] Pietzsch O, Kubetzka A, Bode M and Wiesendanger R 2000 *Phys. Rev. Lett.* **84** 5212
[236] Heinze S, von Bergmann K, Menzel M, Brede J, Kubetzka A, Wiesendanger R, Bihlmayer G and Blugel S 2011 *Nat. Phys.* **7** 713–8
[237] Romming N, Hanneken C, Menzel M, Bickel J E, Wolter B, von Bergmann K, Kubetzka A and Wiesendanger R 2013 *Science* **341** 636–9 (preprint www.sciencemag.org/content/341/6146/636.full.pdf)
[238] Sonntag A, Hermenau J, Krause S and Wiesendanger R 2014 *Phys. Rev. Lett.* **113** 077202
[239] Schattschneider P and Verbeeck J 2011 *Ultramicroscopy* **111** 1461–8
[240] Schattschneider P, Rubino S, Hebert C, Rusz J, Kunes J, Novák P, Carlino E, Fabrizioli M, Panaccione G and Rossi G 2006 *Nature* **441** 486–8
[241] Verbeeck J, Tian H and Schattschneider P 2010 *Nature* **467** 301–4
[242] Beche A, Van Boxem R, Van Tendeloo G and Verbeeck J 2014 *Nat. Phys.* **10** 26–9
[243] Bliokh K Y, Schattschneider P, Verbeeck J and Nori F 2012 *Phys. Rev.* X **2** 041011
[244] Stöhr J and Siegmann H C 2006 *Magnetism: from Fundamentals to Nanoscale Dynamics* (*Solid State Sciences* vol 75) (Berlin: Springer)
[245] Kirz J and Rarback H 1985 *Rev. Sci. Instrum.* **56** 1–13
[246] Schmahl G and Rudolph D 1969 *Optik* **29** 577–85
[247] Niemann B, Rudolph D and Schmahl G 1976 *Appl. Opt.* **15** 1883–4
[248] Fischer P, Schütz G, Schmahl G, Guttmann P and Raasch D 1997 *Z. f. Phys.* B **101** 313
[249] Fischer P, Kim D H, Chao W, Liddle J A, Anderson E H and Attwood D T 2006 *Mater. Today* **9** 26–33
[250] Tonner B P and Harp G R 1988 *Rev. Sci. Instrum.* **59** 853–8
[251] Nolting F *et al* 2000 *Nature* **405** 767–9
[252] Schneider M, Hoffmann H, Otto S, Haug T and Zweck J 2002 *J. Appl. Phys.* **92** 1466–72
[253] Eisebitt S, Luning J, Schlotter W F, Lorgen M, Hellwig O, Eberhardt W and Stohr J 2004 *Nature* **432** 885–8
[254] Chapman H N and Nugent K A 2010 *Nat. Photon.* **4** 833–9

[255] Guttmann P, Bittencourt C, Rehbein S, Umek P, Ke X, Van Tendeloo G, Ewels C P and Schneider G 2012 *Nat. Photon.* **6** 25–9
[256] McPherson A, Gibson G, Jara H, Johann U, Luk T S, McIntyre I A, Boyer K and Rhodes C K 1987 *J. Opt. Soc. Am.* B **4** 595–601
[257] Li X F, L'Huillier A, Ferray M, Lompré L A and Mainfray G 1989 *Phys. Rev.* A **39** 5751–61
[258] Mathias S *et al* 2012 *Proc. Natl Acad. Sci. USA* **109** 4792–7
[259] Turgut E *et al* 2013 *Phys. Rev. Lett.* **110** 197201
[260] Lightsources.org Collaboration (Canadian Light Source) www.lightsources.org
[261] Chen C T, Idzerda Y U, Lin H J, Smith N V, Meigs G, Chaban E, Ho G H, Pellegrin E and Sette F 1995 *Phys. Rev. Lett.* **75** 152
[262] Baez A V 1961 *J. Opt. Soc. Am.* **51** 405–12
[263] Sakdinawat A and Liu Y 2007 *Opt. Lett.* **32** 2635–7
[264] Rehbein S, Heim S, Guttmann P, Werner S and Schneider G 2009 *Phys. Rev. Lett.* **103** 110801
[265] Stöhr J, Padmore H A, Anders S, Stammler T and Scheinfein M R 1998 *Surf. Rev. Lett.* **05** 1297–308
[266] Streubel R, Kronast F, Rößler U K, Schmidt O G and Makarov D 2015 *Phys. Rev.* B **92** 104431
[267] Buckanie N, Kirschbaum P, Sindermann S and Meyer zu Heringdorf F J 2013 *Ultramicroscopy* **130** 49–53
[268] Gierster L, Pape L, Ünal A A and Kronast F 2015 *Rev. Sci. Instrum.* **86** 023702
[269] Ostler T A *et al* 2012 *Nat. Commun.* **3** 666
[270] Le Guyader L, Savoini M, El Moussaoui S, Buzzi M, Tsukamoto A, Itoh A, Kirilyuk A, Rasing T, Kimel A V and Nolting F 2015 *Nat. Commun.* **6** 5839
[271] Micheletto R, Fukuda H and Ohtsu M 1995 *Langmuir* **11** 3333–6
[272] Burmeister F, Schäfle C, Matthes T, Böhmisch M, Boneberg J and Leiderer P 1997 *Langmuir* **13** 2983–7
[273] Haynes C L and Van Duyne R P 2001 *J. Phys. Chem.* **105** 5599–611
[274] Kosiorek A, Kandulski W, Chudzinski P, Kempa K and Giersig M 2004 *Nano Lett.* **4** 1359–63
[275] Zhang W and Haas S 2010 *Phys. Rev.* B **81** 064433
[276] Kappenberger P *et al* 2009 *Appl. Phys. Lett.* **95** 023116
[277] Carcia P F, Meinhaldt A D and Suna A 1985 *Appl. Phys. Lett.* **47** 178–80
[278] Johnson M, Bloemen P, den Broeder F and de Vries J 1996 *Rep. Prog. Phys.* **59** 1409
[279] Hellwig O, Berger A, Kortright J B and Fullerton E E 2007 *J. Magn. Magn. Mater.* **319** 13–55
[280] Hashimoto S, Ochiai Y and Aso K 1989 *J. Appl. Phys.* **66** 4909–16
[281] Lin C J, Gorman G, Lee C, Farrow R, Marinero E, Do H, Notarys H and Chien C 1991 *J. Magn. Magn. Mater.* **93** 194–206
[282] Kim J and Shin S 1996 *J. Appl. Phys.* **80** 3121–3
[283] Guo V W, Lu B, Wu X, Ju G, Valcu B and Weller D 2006 *J. Appl. Phys.* **99** 08E918
[284] den Broeder F, Hoving W and Bloemen P 1991 *J. Magn. Magn. Mater.* **93** 562–70
[285] Engel B N, England C D, Van Leeuwen R A, Wiedmann M H and Falco C M 1991 *Phys. Rev. Lett.* **67** 1910–3
[286] Bagguley D and Heath M 1967 *Proc. Phys. Soc.* **90** 1029
[287] Childress J R, Duvail J L, Jasmin S, Barthélémy A, Fert A, Schuhl A, Durand O and Galtier P 1994 *J. Appl. Phys.* **75** 6412–4
[288] Kimling née Moser J, Kunej V, Pernau H F, Scheer E and Albrecht M 2010 *J. Appl. Phys.* **107** 09C506
[289] Choe S B, Acremann Y, Scholl A, Bauer A, Doran A, Stöhr J and Padmore H A 2004 *Science* **304** 420–2 (preprint www.sciencemag.org/cgi/reprint/304/5669/420.pdf)
[290] Streubel R, Fischer P, Kopte M, Schmidt O G and Makarov D 2015 *Appl. Phys. Lett.* **107** 112406
[291] Streubel R 2015 Imaging spin textures on curved magnetic surfaces *PhD Thesis IFW* Dresden/ TU Chemnitz
[292] Thiele A A 1973 *Phys. Rev. Lett.* **30** 230–3
[293] Makhfudz I, Krüger B and Tchernyshyov O 2012 *Phys. Rev. Lett.* **109** 217201
[294] Ross C 2001 *Ann. Rev. Mater. Res.* **31** 203–35
[295] Adeyeye A O and Singh N 2008 *J. Phys. D: Appl. Phys.* **41** 153001
[296] Terris B 2009 *J. Magn. Magn. Mater.* **321** 512–7 (current perspectives: perpendicular recording)
[297] Albrecht T R, Hellwing O, Ruiz R, Schabes M E, Terris B D and Wu X Z 2009 Chapter Bit-patterned magnetic recording: nanoscale magnetic Islands for data storage *Nanoscale Magnetic Materials and Applications* (Boston, MA: Springer) pp 237–74
[298] Grobis M K, Hellwig O, Hauet T, Dobisz E and Albrecht T R 2011 *IEEE Trans. Magn.* **47** 6–10
[299] Albrecht T R *et al* 2013 *IEEE Trans. Magn.* **49** 773–8
[300] Bita I, Yang J K W, Jung Y S, Ross C A, Thomas E L and Berggren K K 2008 *Science* **321** 939–43
[301] Ruiz R, Kang H, Detcheverry F A, Dobisz E, Kercher D S, Albrecht T R, de Pablo J J and Nealey P F 2008 *Science* **321** 936–9
[302] Hellwig O, Bosworth J K, Dobisz E, Kercher D, Hauet T, Zeltzer G, Risner-Jamtgaard J D, Yaney D and Ruiz R 2010 *Appl. Phys. Lett.* **96** 052511
[303] Ruiz R, Dobisz E and Albrecht T R 2011 *ACS Nano* **5** 79–84
[304] Sun S, Murray C B, Weller D, Folks L and Moser A 2000 *Science* **287** 1989–92
[305] Redl F X, Black C T, Papaefthymiou G C, Sandstrom R L, Yin M, Zeng H, Murray C B and O'Brien S P 2004 *J. Am. Chem. Soc.* **126** 14583–99
[306] Terris B D and Thomson T 2005 *J. Phys. D: Appl. Phys.* **38** R199
[307] Sun S 2006 *Adv. Mater.* **18** 393–403
[308] Lohau J, Moser A, Rettner C T, Best M E and Terris B D 2001 *Appl. Phys. Lett.* **78** 990–2
[309] Barbic M, Schultz S, Wong J and Scherer A 2001 *IEEE Trans. Magn.* **37** 1657–60
[310] Mamin H J, Terris B D, Fan L S, Hoen S, Barrett R C and Rugar D 1995 *IBM J. Res. Dev.* **39** 681–99
[311] Vettiger P *et al* 2002 *IEEE Trans. Nanotechnol.* **1** 39–55
[312] Gidon S, Lemonnier O, Rolland B, Bichet O, Dressler C and Samson Y 2004 *Appl. Phys. Lett.* **85** 6392–4
[313] Barbé C, Bartlett J, Kong L, Finnie K, Lin H, Larkin M, Calleja S, Bush A and Calleja G 2004 *Adv. Mater.* **16** 1959–66
[314] Irvine D J 2011 *Nat. Mater.* **10** 342–3
[315] Jordan A *et al* 2001 *J. Magn. Magn. Mater.* **225** 118–26
[316] Johannsen M, Gneveckow U, Eckelt L, Feussner A, WaldÖFner N, Scholz R, Deger S, Wust P, Loening S A and Jordan A 2005 *Int. J. Hyperth.* **21** 637–47
[317] Valadares L F, Tao Y G, Zacharia N S, Kitaev V, Galembeck F, Kapral R and Ozin G A 2010 *Small* **6** 565–72
[318] Solovev A A, Xi W, Gracias D H, Harazim S M, Deneke C, Sanchez S and Schmidt O G 2012 *ACS Nano* **6** 1751–6
[319] Paxton W F, Kistler K C, Olmeda C C, Sen A, St Angelo S K, Cao Y, Mallouk T E, Lammert P E and Crespi V H 2004 *J. Am. Chem. Soc.* **126** 13424–31
[320] Dreyfus R, Baudry J, Roper M L, Fermigier M, Stone H A and Bibette J 2005 *Nature* **437** 862–5
[321] Howse J R, Jones R A L, Ryan A J, Gough T, Vafabakhsh R and Golestanian R 2007 *Phys. Rev. Lett.* **99** 048102
[322] Solovev A A, Sanchez S, Pumera M, Mei Y F and Schmidt O G 2010 *Adv. Funct. Mater.* **20** 2430–5
[323] Kline T R, Paxton W F, Mallouk T E and Sen A 2005 *Angew. Chem. Int. Ed.* **44** 744–6

[324] Ryzhkova A V, Podgornov F V and Haase W 2010 *Appl. Phys. Lett.* **96** 151901
[325] Loget G and Kuhn A 2011 *Nat. Commun.* **2** 535
[326] Ebbens S J and Howse J R 2010 *Soft Matter* **6** 726–38
[327] Baraban L, Tasinkevych M, Popescu M N, Sanchez S, Dietrich S and Schmidt O G 2012 *Soft Matter* **8** 48–52
[328] Lim J, Lanni C, Evarts E R, Lanni F, Tilton R D and Majetich S A 2011 *ACS Nano* **5** 217–26
[329] Shchukin V A and Bimberg D 1999 *Rev. Mod. Phys.* **71** 1125–71
[330] Castro M, Cuerno R, Vázquez L and Gago R 2005 *Phys. Rev. Lett.* **94** 016102
[331] Bobek T *et al* 2007 *Adv. Mater.* **19** 4375–80
[332] Zhu J, Yu Z, Burkhard G F, Hsu C M, Connor S T, Xu Y, Wang Q, McGehee M, Fan S and Cui Y 2009 *Nano Lett.* **9** 279–82
[333] Teichert C, de Miguel J J and Bobek T 2009 *J. Phys.: Condens. Matter* **21** 224025
[334] Faustini M, Capobianchi A, Varvaro G and Grosso D 2012 *Chem. Mater.* **24** 1072–9
[335] Teichert C, Barthel J, Oepen H P and Kirschner J 1999 *Appl. Phys. Lett.* **74** 588–90
[336] Mulders A M *et al* 2005 *Phys. Rev.* B **71** 214422
[337] Facsko S, Dekorsy T, Koerdt C, Trappe C, Kurz H, Vogt A and Hartnagel H L 1999 *Science* **285** 1551–3
[338] Fassbender J, Strache T, Liedke M O, Markó D, Wintz S, Lenz K, Keller A, Facsko S, Mönch I and McCord J 2009 *New J. Phys.* **11** 125002
[339] Sigmund P 1969 *Phys. Rev.* **184** 383–416
[340] Bradley R M and Harper J M E 1988 *J. Vac. Sci. Technol.* A **6** 2390–5
[341] Facsko S, Bobek T, Stahl A, Kurz H and Dekorsy T 2004 *Phys. Rev.* B **69** 153412
[342] Keller A, Biermanns A, Carbone G, Grenzer J, Facsko S, Plantevin O, Gago R and Metzger T H 2009 *Appl. Phys. Lett.* **94** 193103
[343] Bradley R M 2011 *Phys. Rev.* B **83** 195410
[344] Ziberi B, Frost F, Höche T and Rauschenbach B 2005 *Phys. Rev.* B **72** 235310
[345] Fritzsche M, Muecklich A and Facsko S 2012 *Appl. Phys. Lett.* **100** 223108
[346] Chan W L and Chason E 2007 *J. Appl. Phys.* **101** 121301
[347] Park S H, Kim S O, Oh H S, Choa S H and Lee T D 2007 *Phys. Status Solidi* c **4** 4516–9
[348] Piramanayagam S N 2007 *J. Appl. Phys.* **102** 011301
[349] Keller A, Roßbach S, Facsko S and Möller W 2008 *Nanotechnology* **19** 135303
[350] Biermanns A, Pietsch U, Grenzer J, Hanisch A, Facsko S, Carbone G and Metzger T H 2008 *J. Appl. Phys.* **104** 044312
[351] Buchter A *et al* 2013 *Phys. Rev. Lett.* **111** 067202
[352] Da Col S *et al* 2014 *Phys. Rev.* B **89** 180405
[353] Lee W, Schwirn K, Steinhart M, Pippel E, Scholz R and Gosele U 2008 *Nat. Nanotechnol.* **3** 234–9
[354] Thiaville A and Nakatani Y 2006 Domain-wall dynamics in nanowires and nanostrips *Spin Dynamics in Confined Magnetic Structures* III (*Topics in Applied Physics* vol 101) ed B Hillebrands and A Thiaville (Berlin: Springer) pp 161–206
[355] Deneke C, Jin-Phillipp N Y, Loa I and Schmidt O G 2004 *Appl. Phys. Lett.* **84** 4475–7
[356] Schumacher O, Mendach S, Welsch H, Schramm A, Heyn C and Hansen W 2005 *Appl. Phys. Lett.* **86** 143109
[357] Deneke C, Sigle W, Eigenthaler U, van Aken P A, Schütz G and Schmidt O G 2007 *Appl. Phys. Lett.* **90** 263107
[358] Deneke C, Songmuang R, Jin-Phillipp N Y and Schmidt O G 2009 *J. Phys. D: Appl. Phys.* **42** 103001
[359] Deneke C, Müller C, Jin-Phillipp N Y and Schmidt O G 2002 *Semicond. Sci. Technol.* **17** 1278
[360] Yablonovitch E, Gmitter T, Harbison J P and Bhat R 1987 *Appl. Phys. Lett.* **51** 2222–4
[361] Rao K S K, Katayama T, Yokoyama S and Hirose M 2000 *Japan. J. Appl. Phys.* **39** L457
[362] Palmstrøm C 2003 *MRS Bull.* **28** 725–8
[363] Herfort J, Jenichen B, Kaganer V, Trampert A, Schönherr H P and Ploog K 2006 *Phys. E: Low-Dimens. Syst. Nanostruct.* **32** 371–4
[364] Wolf S A, Awschalom D D, Buhrman R A, Daughton J M, von Molnar S, Roukes M L, Chtchelkanova A Y and Treger D M 2001 *Science* **294** 1488–95 (preprint www.sciencemag.org/cgi/reprint/294/5546/1488.pdf)
[365] Galanakis I, Dederichs P H and Papanikolaou N 2002 *Phys. Rev.* B **66** 174429
[366] Awschalom D D, Loss D and Samarth N (ed) 2013 *Semiconductor Spintronics and Quantum Computation* (Berlin: Springer)
[367] Herfort J, Schönherr H P and Ploog K H 2003 *Appl. Phys. Lett.* **83** 3912–4
[368] Liou S H, Malhotra S S, Shen J X, Hong M, Kwo J, Chen H S and Mannaerts J P 1993 *J. Appl. Phys.* **73** 6766–8
[369] Ionescu A *et al* 2005 *Phys. Rev.* B **71** 094401
[370] Deneke C, Schumann J, Engelhard R, Thomas J, Sigle W, Zschieschang U, Klauk H, Chuvilin A and Schmidt O G 2008 *Phys. Status Solidi* c **5** 2704–8
[371] Deneke C, Schumann J, Engelhard R, Thomas J, Müller C, Khatri M S, Malachias A, Weisser M, Metzger T H and Schmidt O G 2009 *Nanotechnology* **20** 045703
[372] Deneke C, Zschieschang U, Klauk H and Schmidt O G 2006 *Appl. Phys. Lett.* **89** 263110
[373] Jin-Phillipp N Y, Thomas J, Kelsch M, Deneke C, Songmuang R and Schmidt O G 2006 *Appl. Phys. Lett.* **88** 033113
[374] Paetzelt H, Gottschalch V, Bauer J, Herrnberger H and Wagner G 2006 *Phys. Status Solidi* a **203** 817–24
[375] Songmuang R, Deneke C and Schmidt O G 2006 *Appl. Phys. Lett.* **89** 223109
[376] Bof Bufon C C, Cojal González J D, Thurmer D J, Grimm D, Bauer M and Schmidt O G 2010 *Nano Lett.* **10** 2506–10
[377] Karnaushenko D D, Karnaushenko D, Makarov D and Schmidt O G 2015 *NPG Asia Mater.* **7** e188
[378] Karnaushenko D, Münzenrieder N, Karnaushenko D D, Koch B, Meyer A K, Baunack S, Petti L, Tröster G, Makarov D and Schmidt O G 2015 *Adv. Mater.* **27** 6797–805
[379] Lebedev M A and Nicolelis M A L 2016 *Trends Neurosci.* **29** 536–46
[380] Funke M E, Moore K, Orrison W W Jr and Lewine J D 2011 *Epilepsia* **52** 10–4
[381] Fomin V M, Smith E J, Karnaushenko D D, Makarov D and Schmidt O G 2013 *Phys. Rev.* E **87** 052122
[382] Dick B, Brett M J and Smy T 2003 *J. Vac. Sci. Technol.* B **21** 23–8
[383] Kak A C and Slaney M 1988 *Principles of Computerized Tomographic Imaging* vol 33 (New York: IEEE)
[384] Radon J 1917 *Ber. Verh. Sächs. Akad. Wiss.* **69** 262
[385] Nyquist H 1928 *Trans. AIEE* **47** 617–44
[386] Kaczmarz S 1937 *Bull. Int. Acad. Pol. Sci. Lett.* **35** 355
[387] De Rosier D J and Klug A 1968 *Nature* **217** 130–4
[388] Midgley P A and Dunin-Borkowski R E 2009 *Nat. Mater.* **8** 1476–122
[389] Schärpf O 1978 *J. Appl. Cryst.* **11** 626–30
[390] Lange A, Hentschel M P and Kupsch A 2008 *MP Mater. Test.* **50** 272
[391] Gabor D 1948 *Nature* **161** 777–8
[392] Lichte H 1986 *Ultramicroscopy* **20** 293
[393] Paganin D and Nugent K A 1998 *Phys. Rev. Lett.* **80** 2586–9
[394] De Graef M and Zhu Y 2001 *J. Appl. Phys.* **89** 7177–9

[395] Lade S J, Paganin D and Morgan M J 2005 *Opt. Commun.* **253** 392–400
[396] Phatak C, Beleggia M and De Graef M 2008 *Ultramicroscopy* **108** 503–13
[397] Aharonov Y and Bohm D 1959 *Phys. Rev.* **115** 485–91
[398] Möllenstedt G and Düker H 1956 *Z. Physik* **145** 377–97
[399] Glass R, Arnold M, Blümmel J, Küller A, Möller M and Spatz J 2003 *Adv. Funct. Mater.* **13** 569–75
[400] Phatak C, Petford-Long A K, Heinonen O, Tanase M and De Graef M 2011 *Phys. Rev.* B **83** 174431
[401] Volkov V, Zhu Y and Graef M D 2002 *Micron* **33** 411–6
[402] Lee J, Makarov D, Brombacher C, Dymerska B, Suess D, Albrecht M and Fidler J 2014 *Nanotechnology* **25** 045604
[403] Otálora J, López-López J, Núñez A S and Landeros P 2012 *J. Phys.: Condens. Matter* **24** 436007
[404] Rothemund P W 2006 *Nature* **440** 297–302
[405] Kuzyk A, Schreiber R, Fan Z, Pardatscher G, Roller E M, Hogele A, Simmel F C, Govorov A O and Liedl T 2012 *Nature* **483** 311–4
[406] McNulty I, Kirz J, Jacobsen C, Anderson E H, Howells M R and Kern D P 1992 *Science* **256** 1009–12
[407] Chapman H N *et al* 2007 *Nature* **448** 676–9
[408] Marchesini S *et al* 2008 *Nat. Photon.* **2** 560–3
[409] Ravasio A *et al* 2009 *Phys. Rev. Lett.* **103** 028104
[410] Zhu D *et al* 2010 *Phys. Rev. Lett.* **105** 043901
[411] Gauthier D, Guizar-Sicairos M, Ge X, Boutu W, Carré B, Fienup J R and Merdji H 2010 *Phys. Rev. Lett.* **105** 093901
[412] Gunther C M *et al* 2011 *Nat. Photon.* **5** 99–102
[413] Roy S, Parkinson D, Seu K A, Su R, Turner J J, Chao W, Anderson E H, Cabrini S and Kevan S D 2011 *Nat. Photon.* **5** 243–5
[414] Wang T *et al* 2012 *Phys. Rev. Lett.* **108** 267403
[415] Rodenburg J M and Faulkner H M L 2004 *Appl. Phys. Lett.* **85** 4795
[416] Shapiro D *et al* 2005 *Proc. Natl Acad. Sci.* **102** 15343–6
[417] Pfeifer M A, Williams G J, Vartanyants I A, Harder R and Robinson I K 2006 *Nature* **442** 63–6
[418] Thibault P, Dierolf M, Menzel A, Bunk O, David C and Pfeiffer F 2008 *Science* **321** 379–82
[419] Rodenburg J 2008 *Ptychography and Related Diffractive Imaging Methods* (*Advances in Imaging and Electron Physics* vol 150) (Amsterdam: Elsevier) pp 87
[420] Dierolf M, Menzel A, Thibault P, Schneider P, Kewish C M, Wepf R, Bunk O and Pfeiffer F 2010 *Nature* **467** 436–9
[421] Giewekemeyer K, Thibault P, Kalbfleisch S, Beerlink A, Kewish C M, Dierolf M, Pfeiffer F and Salditt T 2010 *Proc. Natl Acad. Sci.* **107** 529–34
[422] Tripathi A, Mohanty J, Dietze S H, Shpyrko O G, Shipton E, Fullerton E E, Kim S S and McNulty I 2011 *Proc. Natl Acad. Sci.* **108** 13393–8
[423] Donnelly C *et al* 2015 *Phys. Rev. Lett.* **114** 115501
[424] Pendry J B 2000 *Phys. Rev. Lett.* **85** 3966–9
[425] Pendry J B and Anantha Ramakrishna S 2002 *J. Phys.: Condens. Matter* **14** 8463
[426] Pendry J 2003 *Opt. Express* **11** 755–60
[427] Liu Z, Lee H, Xiong Y, Sun C and Zhang X 2007 *Science* **315** 1686
[428] Sebastian T, Schultheiss K, Obry B, Hillebrands B, Schultheiss H and Obry B 2015 *Front. Phys.* **3**
[429] Melzer M *et al* 2015 *Adv. Mater.* **27** 1274–80
[430] Lin G, Makarov D, Melzer M, Si W, Yan C and Schmidt O G 2014 *Lab Chip* **14** 4050–8
[431] Pérez N, Melzer M, Makarov D, Ueberschär O, Ecke R, Schulz S E and Schmidt O G 2015 *Appl. Phys. Lett.* **106** 153501
[432] Karnaushenko D, Makarov D, Yan C, Streubel R and Schmidt O G 2012 *Adv. Mater.* **24** 4518–22
[433] Makarov D, Karnaushenko D and Schmidt O G 2013 *ChemPhysChem* **14** 1771–6
[434] Karnaushenko D, Makarov D, Stöber M, Karnaushenko D D, Baunack S and Schmidt O G 2015 *Adv. Mater.* **27** 880–5